

CORE/SHELL TYPE, Ce<sup>3+</sup> and Tb<sup>3+</sup> DOPED GdBO<sub>3</sub>/SiO<sub>2</sub> SYSTEM:  
SYNTHESIS AND CELECOXIB DRUG DELIVERY APPLICATIONS

A THESIS SUBMITTED TO  
THE GRADUATE SCHOOL OF NATURAL AND APPLIED SCIENCES  
OF  
MIDDLE EAST TECHNICAL UNIVERSITY

BY

PELIN AKMAN

IN PARTIAL FULFILLMENT OF THE REQUIREMENTS  
FOR  
THE DEGREE OF MASTER OF SCIENCE  
IN  
CHEMISTRY

JUNE 2019



Approval of the thesis:

**CORE/SHELL TYPE, Ce<sup>3+</sup> AND Tb<sup>3+</sup> DOPED GdBO<sub>3</sub>/SiO<sub>2</sub> SYSTEM:  
SYNTHESIS AND CELECOXIB DRUG DELIVERY APPLICATIONS**

submitted by **PELIN AKMAN** in partial fulfillment of the requirements for the degree of **Master of Science in Chemistry Department, Middle East Technical University** by,

Prof. Dr. Halil Kalıpçılar  
Dean, Graduate School of **Natural and Applied Sciences**

\_\_\_\_\_

Prof. Dr. Cihangir Tanyeli  
Head of Department, **Chemistry**

\_\_\_\_\_

Prof. Dr. Ayşen Yılmaz  
Supervisor, **Chemistry, METU**

\_\_\_\_\_

**Examining Committee Members:**

Prof. Dr. Birgül Zümreoğlu Karan  
Chemistry, Hacettepe University

\_\_\_\_\_

Prof. Dr. Ayşen Yılmaz  
Chemistry, METU

\_\_\_\_\_

Prof. Dr. Okan Esentürk  
Chemistry, METU

\_\_\_\_\_

Assoc. Prof. Dr. İrem Erel Göktepe  
Chemistry, METU

\_\_\_\_\_

Prof. Dr. Ceyhan Kayran İşçi  
Chemistry, METU

\_\_\_\_\_

Date: 17.06.2019

**I hereby declare that all information in this document has been obtained and presented in accordance with academic rules and ethical conduct. I also declare that, as required by these rules and conduct, I have fully cited and referenced all material and results that are not original to this work.**

Name, Surname: Pelin Akman

Signature:

## ABSTRACT

### **CORE/SHELL TYPE, Ce<sup>3+</sup> AND Tb<sup>3+</sup> DOPED GdBO<sub>3</sub>/SiO<sub>2</sub> SYSTEM: SYNTHESIS AND CELECOXIB DRUG DELIVERY APPLICATIONS**

Akman, Pelin  
Master of Science, Chemistry  
Supervisor: Prof. Dr. Ayşen Yılmaz

June 2019, 84 pages

Multifunctional nanoparticles have been widely used as drug carriers to control drug release. However, besides controlling drug release, it is important to track the behavior of the drug in body. For this purpose, functionalizing the drug carriers with luminescent or magnetic materials and using them as bioimaging agents have attracted attention in recent years. In this study, luminescent and magnetic core/shell Gd<sub>1-x-y</sub>Ce<sub>x</sub>Tb<sub>y</sub>BO<sub>3</sub>@SiO<sub>2</sub> (x=0.05, y=0.05) nanoparticles were synthesized and used in celecoxib drug delivery system. Celecoxib is a nonsteroidal anti-inflammatory and poorly water soluble, hydrophobic drug. In order to visualize the drug in body, both magnetic and luminescent core was synthesized. This core is composed of Ce and Tb doped Gadolinium borate synthesized by Pechini sol-gel method. Different proportions of Ce and Tb doped GdBO<sub>3</sub> were synthesized and their photoluminescence (PL) spectra were compared. After that, Gd<sub>0.90</sub>Ce<sub>0.05</sub>Tb<sub>0.05</sub>BO<sub>3</sub> was determined as the best luminescent core. Also, Gadolinium is strongly paramagnetic and widely used as contrast agent in magnetic resonance imaging (MRI). To increase drug loading capacity, mesoporous silica was chosen because of its high surface area, porosity, high biocompatibility and easy synthesis route. Mesoporous silica coating to Gd<sub>0.90</sub>Ce<sub>0.05</sub>Tb<sub>0.05</sub>BO<sub>3</sub> core was done by modified Stöber method. The obtained Gd<sub>0.90</sub>Ce<sub>0.05</sub>Tb<sub>0.05</sub>BO<sub>3</sub> core particles have a diameter of 60 nm and silica coated Gd<sub>0.90</sub>Ce<sub>0.05</sub>Tb<sub>0.05</sub>BO<sub>3</sub>@SiO<sub>2</sub> core/shell particles have a diameter of 200-400 nm. They

have considerably high luminescence intensity. After silica coating, drug loading was done in ethanol and a substantial decrease in photoluminescence intensity was observed for drug loaded sample. This means that during the drug release, luminescence increases, so by comparing the PL intensity, drug amount released from the carrier can be calculated. Drug release profile was obtained in pH 7.4, phosphate buffer solution (PBS) for 24 hours. Celebrex is the commercially available form of Celecoxib. For the characterization of the materials, X-Ray Diffractometry (XRD), Fourier-Transform Infrared Spectroscopy (FTIR), Transmission Electron Microscopy (TEM), Scanning Electron Microscopy (SEM), Photoluminescence spectroscopy (PL), Thermogravimetric Analysis (TGA), Nitrogen-sorption analysis, and Zeta-potential analysis were used. For drug release calculations Ultraviolet–visible spectroscopy (UV-VIS) was used. The cytotoxicity assay was done by using HCT-116 human colon cancer cells. The release profile of the prepared Celecoxib loaded carrier and commercial drug, Celebrex were compared according to UV-VIS results and it is understood that the solubility of the drug was enhanced with the drug carrier. All of the results here confirm that  $Gd_{0.90}Ce_{0.05}Tb_{0.05}BO_3@SiO_2$  nanoparticles are promising as drug carriers and also as bioimaging agents.

Keywords: Core/shell, Gadolinium Borate, Magnetic, Bioimaging, Drug Delivery

## ÖZ

### ÇEKİRDEK/KABUK YAPILI, Ce<sup>3+</sup> VE Tb<sup>3+</sup> KATKILI GdBO<sub>3</sub>/SiO<sub>2</sub> NANOPARÇACIKLARIN SENTEZİ VE SELEKOKSİB İLAÇ TAŞIYICI SİSTEMDE UYGULANMASI

Akman, Pelin  
Yüksek Lisans, Kimya  
Tez Danışmanı: Prof. Dr. Ayşen Yılmaz

Haziran 2019, 84 sayfa

Çoklu fonksiyonlu nanoparçacıklar kontrollü ilaç salımında çok yaygın kullanılmaktadır. Kontrollü ilaç salımı dışında ilacın vücuttaki davranışını takip edebilmek de önemli olduğundan, ilaç taşıyıcı sistem bu amaca yönelik lüminesan ya da manyetik özelliklere sahip hale getirilmeye çalışılmaktadır. Bu çalışmada lüminesan ve manyetik özellikli, çekirdek/kabuk yapısında Gd<sub>0.90</sub>Ce<sub>0.05</sub>Tb<sub>0.05</sub>BO<sub>3</sub>@SiO<sub>2</sub> nanoparçacıkları sentezlenmiş, bu parçacıklar Selekoksib ilacı için taşıma sistemi olarak kullanılmıştır. Selekoksib sudaki çözünürlüğü düşük olan hidrofobik bir ilaçtır. İlacın vücutta görüntülenebilmesi için hem lüminesan hem manyetik özellikte bir çekirdek sentezlenmiştir. Bu çekirdek Ce<sup>3+</sup> ve Tb<sup>3+</sup> katkılanmış Gadolinyum borat (GdBO<sub>3</sub>) parçacıklarından oluşmaktadır ve Pechini sol-jel metodu ile sentezlenmiştir. Farklı Ce<sup>3+</sup> ve Tb<sup>3+</sup> konsantrasyonlarına sahip GdBO<sub>3</sub> sentezlenmiş ve en yüksek fotoışıma şiddeti % 5 Ce<sup>3+</sup> ve % 5 Tb<sup>3+</sup> katkılanmış örnekte gözlemlenmiştir. Bunun yanısıra, Gd elementi güçlü paramanyetik özelliğe sahip olduğundan Manyetik Rezonans görüntüleme (MRI) manyetik kontrast ajanı olarak kullanılır. Mezogözenekli silikanın kabuk olarak kullanılma amacı ise yüksek yüzey alanına sahip olması, böylece ilaç yükleme kapasitesini artırması, yüksek biyouyumluluğu ve kolay sentezlenebilmesidir.

Çekirdeğin mezogözenekli silika ile kaplanması modifiye edilmiş Stöber metodu ile yapılmıştır. Elde edilen çekirdekler 60 nm çapında, çekirdek/kabuk parçacıkları ise 200-400 nm çapında olup yüksek fotoışıma şiddetine sahiptirler. Silika kaplama ve etanol içerisinde ilaç yükleme işleminden sonra fotoışıma şiddetinde azalma gözlenmiştir. Bu azalma, fotoışıma şiddetinin ilaç salımı sırasında artacağını gösterirken, ilaç miktarının fotoışıma şiddeti sayesinde hesaplanabilmesine olanak tanır. İlaç salınım grafiği 7.4 pH'a sahip fosfatlı tampon çözeltisi (PBS) içerisinde yapılan deneyler ile elde edilmiştir. Parçacıkların özelliklerinin belirlenmesi için X ışınları toz kırınımı (XRD), taramalı elektron mikroskobu (SEM), fourier dönüşümlü kızılötesi spektroskopisi (FT-IR), geçirimli elektron mikroskobu (TEM), termogravimetrik analiz (TGA), flüoresans spektrometresi (PL), zeta potansiyeli, azot emilimi analizleri yapılmıştır. İlaç salınımı için ise ultraviyole ve görünür ışık absorpsiyon spektrometresi (UV-VIS) kullanılmıştır. Sitotoksite deneyleri HCT-116 kolon kanser hücreleri ile yapılmıştır. İlaç taşıyıcının ve piyasada satılan Celebrex ilacının salım eğrileri karşılaştırılmış, ilaç taşıyıcının Selekoksisib çözünürlüğünü artırdığı gözlemlenmiştir. Tüm bu sonuçlar  $Gd_{0.90}Ce_{0.05}Tb_{0.05}BO_3@SiO_2$  nanoparçacıklarının hem ilaç salımında hem de biyogörüntüleme kullanılabileceğini göstermektedir.

Anahtar Kelimeler: Çekirdek/kabuk, Gadolinyum Borat, Manyetik, Biyogörüntüleme, İlaç taşıyıcı

to my family...

## ACKNOWLEDGEMENTS

First, I would like to thank my supervisor, Prof. Dr. Ayşen Yılmaz for the opportunity she gave to me, for her endless support and patience. All the things I have learnt from her were invaluable.

I would like to thank Prof. Dr. Okan Esentürk and Prof. Dr. Ahmet M. Önal for their collaboration in photoluminescence studies and Prof. Dr. Enver Bulur for quantum yield measurements, also sharing their knowledge.

I would like to thank my lab mates Gencay Çelik, Özde Ceren Abacı, Oğuzcan Taneroğlu and Ali Farid for their friendship and endless support.

I would like to thank my beautiful friend Dr. Sera İflazoğlu for her support, she is like a sister for me.

I would like to thank Assoc. Prof. Dr. Özgül Persil Çetinkol, Assoc. Prof. Dr. İrem Erel Göktepe and Prof. Dr. Saim Özkar for their assistance by letting me to utilize their research laboratory during the study and Dr. İbrahim Çam from METU Central laboratory for magnetism analyses.

I would like to express my gratitude for Prof. Dr. Sreeparna Banerjee and Sinem Ulusan for sharing their research lab and knowledge.

I would like to thank Eda Alemdar Yılmaz and Gizem Atakan for their lovely friendship and sharing tons of fun memories. They were always right beside me to climb every obstacle.

I owe my special thanks to Mete Çolak for his true love, patience, support and especially for always holding my hand to overcome the difficulties. I believe I can deal with anything as long as he is right beside me.

I want to give the best love and gratitude to my mother, my father and my sister. Without their love and support I could not succeed anything.

## TABLE OF CONTENTS

ABSTRACT .....	v
ÖZ .....	vii
ACKNOWLEDGEMENTS .....	x
TABLE OF CONTENTS .....	xi
LIST OF TABLES .....	xv
LIST OF FIGURES .....	xvi
LIST OF ABBREVIATIONS .....	xx
CHAPTERS	
1. INTRODUCTION .....	1
1.1. Luminescence and luminescent materials .....	1
1.1.1. Fundamental mechanisms of luminescence.....	1
1.1.2. The quantum yield of luminescence .....	4
1.1.3. Luminescent materials .....	5
1.1.4. Rare earth (RE) ions and their luminescence properties.....	7
1.1.4.1. Photoluminescence properties of Cerium (Ce) .....	11
1.1.4.2. Photoluminescence properties of Terbium (Tb) .....	12
1.2. Rare earth borates .....	13
1.2.1. Gadolinium Borate (GdBO <sub>3</sub> ) .....	15
1.2.2. Rare earth doped borates.....	17
1.3. Synthesis methods of inorganic phosphors .....	18

1.3.1. Sol-gel synthesis.....	19
1.4. Drug delivery systems.....	20
1.4.1. Polymeric matrices .....	22
1.4.2. Core/shell structures .....	22
1.4.2.1. Inorganic/Inorganic Core/Shell Materials .....	23
1.5. Hydrophobic drugs.....	24
1.5.1. Celecoxib.....	24
1.6. Multifunctionality of nano-drug carriers.....	25
1.6.1. Drug loading and release properties .....	26
1.6.2. Visualization.....	27
1.6.2.1. Luminescent drug carriers .....	27
1.6.2.2. Magnetic drug carriers .....	28
1.7. Aim of the work .....	29
2. EXPERIMENTAL .....	31
2.1. Materials.....	31
2.2. Synthesis of $Gd_{1-x-y}Ce_xTb_yBO_3$ core .....	31
2.3. Silica coating to $Gd_{1-x-y}Ce_xTb_yBO_3$ .....	31
2.4. Celecoxib loading .....	32
2.5. Celecoxib release .....	32
2.6. Cell proliferation assay .....	33
3. CHARACTERIZATION.....	35
3.1. Powder X-Ray diffraction (XRD).....	35
3.2. Photoluminescence spectroscopy (PL) .....	35
3.3. CIE chromaticity diagram.....	35

3.4. Integrating sphere for measurements of fluorescence quantum yield .....	37
3.5. Transmission electron microscopy (TEM) .....	37
3.6. Scanning electron microscopy (SEM) .....	38
3.7. Fourier transform infrared spectroscopy (FT-IR) .....	38
3.8. Nitrogen-sorption .....	38
3.9. Thermogravimetric analysis (TGA) .....	38
3.10. Vibrating sample magnetometer (VSM) .....	38
3.11. Zeta-potential .....	39
3.12. Ultraviolet-visible spectroscopy (UV-VIS) .....	39
4. RESULTS & DISCUSSION .....	41
4.1. Powder X-Ray diffraction pattern of core, core/shell and drug loaded core/shell particles .....	42
4.2. Photoluminescence spectra of core, core/shell and drug loaded core/shell particles .....	45
4.3. CIE chromaticity diagram .....	55
4.4. Integrating sphere measurements of fluorescence quantum yield .....	56
4.5. Transmission electron microscopy (TEM) .....	58
4.6. Scanning electron microscopy (SEM) .....	61
4.7. FTIR Spectroscopy .....	63
4.8. Nitrogen adsorption-desorption analysis .....	65
4.8.1. Brauner-Emmett-Teller (BET) method .....	65
4.8.2. Barret-Joyner-Halenda (BJH) method .....	66
4.9. Thermogravimetric analysis (TGA) .....	67
4.10. Vibrating-sample magnetometer (VSM) .....	68

4.11. Zeta-potential .....	71
4.12. UV-VIS analysis .....	71
4.12.1. Celecoxib loading .....	72
4.12.2. Celecoxib release.....	72
4.13. Cell proliferation assay .....	75
5. CONCLUSION .....	77
REFERENCES .....	79

## LIST OF TABLES

### TABLES

Table 1. Electronic states of the rare earth metals. ....	10
Table 2. Global B <sub>2</sub> O <sub>3</sub> stockpile (2017). ....	15
Table 3. Chemicals used to prepare PBS. ....	33
Table 4. Magnetization values of core, core/shell and Celecoxib loaded core/shell materials. ....	69
Table 5. Coercivity values of core, core/shell and Celecoxib loaded core/shell materials. ....	69
Table 7. Zeta potential results for core, core/shell and Celecoxib loaded core/shell samples. ....	71

## LIST OF FIGURES

### FIGURES

Figure 1. Luminescence types depending on the duration. ....	2
Figure 2. Radiative (R) and nonradiative (NR) paths.....	3
Figure 3. Jablonski diagram.....	3
Figure 4. Emission spectra of reference sample A and sample B, .....	5
Figure 5. Direct (a) and indirect (b) excitation and energy transfer mechanism (E.T.: energy transfer). ....	5
Figure 6. Emission spectra of different amounts of Yb <sup>3+</sup> doped materials (with an excitation wavelength of 976 nm). ....	6
Figure 7. Configurational coordinate diagram with (a) absorption, (b) emission and (c) Stokes' shift. ....	7
Figure 8. Dieke Diagram of rare Earth ions. ....	8
Figure 9. Energy level diagram of Ce <sup>3+</sup> .....	11
Figure 10. Energy level diagram of Tb <sup>3+</sup> .....	13
Figure 11. Gadolinium borate lattice structure (black spheres: Gd, red spheres: O, blue spheres: B). ....	16
Figure 12. (a) B <sub>3</sub> O <sub>9</sub> <sup>9-</sup> ring (b and c) coordination spheres of the B cations without one O4 or O5. ....	17
Figure 13. Drug concentration vs. time profile for single dose and multiple dose of conventional, sustained and controlled delivery formulations. (MSC: Minimum safe concentration, MEC: Minimum effective concentration).....	21
Figure 14. Chemical structure of Celecoxib. ....	25

Figure 15. $\beta$ -NaYF <sub>4</sub> :Gd <sup>3+</sup> /Tb <sup>3+</sup> nanorods and (f) $\beta$ -NaYF <sub>4</sub> :Gd <sup>3+</sup> /Tb <sup>3+</sup> - DOX conjugate at various molar concentrations in water. ....	29
Figure 16. CIE chromaticity diagram.....	37
Figure 17. Experimental scheme for core, core/shell synthesis and drug loading (PEG: polyethylene glycol, EDTA: ethylenediaminetetraacetic acid, CTAB: cetyltrimethylammonium bromide, TEOS: tetraethylorthosilicate, CLX: celecoxib). ....	42
Figure 18. (a) XRD patterns of Gd <sub>0.90</sub> Ce <sub>0.05</sub> Tb <sub>0.05</sub> BO <sub>3</sub> synthesized with citric acid and EDTA, GdBO <sub>3</sub> card, 13-0483 (b) XRD pattern of citric acid synthesis, GdBO <sub>3</sub> card and Gd(BO <sub>2</sub> ) <sub>3</sub> card, 70-2239. ....	43
Figure 19. XRD patterns of Gd <sub>0.65</sub> Ce <sub>0.10</sub> Tb <sub>0.25</sub> BO <sub>3</sub> and Gd <sub>0.90</sub> Ce <sub>0.05</sub> Tb <sub>0.05</sub> BO <sub>3</sub> core which were synthesized by using EDTA. ....	44
Figure 20. XRD patterns of core, core/shell and drug loaded samples.....	45
Figure 21. Photoluminescence excitation spectra of Gd <sub>0.90</sub> Ce <sub>0.05</sub> Tb <sub>0.05</sub> BO <sub>3</sub> at 545 nm wavelength. ....	46
Figure 22. Photoluminescence emission spectra of Gd <sub>0.98</sub> Ce <sub>0.01</sub> Tb <sub>0.01</sub> BO <sub>3</sub> and Gd <sub>0.96</sub> Ce <sub>0.01</sub> Tb <sub>0.03</sub> BO <sub>3</sub> at an excitation wavelength of 359 nm.....	47
Figure 23. Photoluminescence emission spectra of Gd <sub>0.90</sub> Ce <sub>0.05</sub> Tb <sub>0.05</sub> BO <sub>3</sub> and Gd <sub>0.87</sub> Ce <sub>0.05</sub> Tb <sub>0.08</sub> BO <sub>3</sub> at an excitation wavelength of 359 nm.....	48
Figure 24. Photoluminescence emission spectra of Gd <sub>0.85</sub> Ce <sub>0.10</sub> Tb <sub>0.05</sub> BO <sub>3</sub> , Gd <sub>0.75</sub> Ce <sub>0.10</sub> Tb <sub>0.15</sub> BO <sub>3</sub> , Gd <sub>0.70</sub> Ce <sub>0.10</sub> Tb <sub>0.20</sub> BO <sub>3</sub> and Gd <sub>0.65</sub> Ce <sub>0.10</sub> Tb <sub>0.25</sub> BO <sub>3</sub> at an excitation wavelength of 359 nm. ....	49
Figure 25. Photoluminescence emission spectra of Gd <sub>0.70</sub> Ce <sub>0.10</sub> Tb <sub>0.20</sub> BO <sub>3</sub> and Gd <sub>0.90</sub> Ce <sub>0.05</sub> Tb <sub>0.05</sub> BO <sub>3</sub> at an excitation wavelength of 359 nm. ....	50
Figure 26. Photoluminescence emission spectra of Gd <sub>1-x-y</sub> Ce <sub>x</sub> Tb <sub>y</sub> BO <sub>3</sub> with different concentrations of Ce and Tb at an excitation wavelength of 359 nm. ....	51
Figure 27. Photoluminescence emission spectra of Gd <sub>0.90</sub> Ce <sub>0.05</sub> Tb <sub>0.05</sub> BO <sub>3</sub> and Gd <sub>0.95</sub> Tb <sub>0.05</sub> BO <sub>3</sub> , at an excitation wavelength of 359 nm.....	52

Figure 28. Photoluminescence emission spectra of $Gd_{0.90}Ce_{0.05}Tb_{0.05}BO_3$ core, $SiO_2$ coated core and drug loaded core/shell samples at an excitation wavelength of 359 nm. ....	53
Figure 29. Photoluminescence emission spectra of Celecoxib loaded samples after 30 minutes, 2 hours, 4 hours and 6 hours of drug release in PBS at an excitation wavelength of 359 nm. ....	54
Figure 30. Photoluminescence intensity as a function of the cumulatively released CLX. ....	54
Figure 31. CIE chromaticity diagram for $Gd_{0.90}Ce_{0.05}Tb_{0.05}BO_3$ . ....	55
Figure 32. Image of $Gd_{0.90}Ce_{0.05}Tb_{0.05}BO_3$ samples both in water-dispersed and solid forms under UV lamp, 366 nm. ....	56
Figure 33. Photoluminescence spectra of $Gd_{0.90}Ce_{0.05}Tb_{0.05}BO_3$ . ....	57
Figure 34. Average quantum yield of $Gd_{0.90}Ce_{0.05}Tb_{0.05}BO_3$ . ....	58
Figure 35. (a) TEM image of $Gd_{0.90}Ce_{0.05}Tb_{0.05}BO_3$ core samples synthesized with EDTA, (b) TEM image of $Gd_{0.90}Ce_{0.05}Tb_{0.05}BO_3$ core samples synthesized with citric acid. ....	59
Figure 36. TEM images of single silica-coated $Gd_{0.90}Ce_{0.05}Tb_{0.05}BO_3$ core samples. ....	60
Figure 37. TEM images of double silica-coated $Gd_{0.90}Ce_{0.05}Tb_{0.05}BO_3$ core samples. ....	60
Figure 38. TEM images of double silica-coated $Gd_{0.90}Ce_{0.05}Tb_{0.05}BO_3$ core samples. ....	61
Figure 39. (a) SEM images of $Gd_{0.90}Ce_{0.05}Tb_{0.05}BO_3$ core samples synthesized with citric acid and (b) core samples synthesized with EDTA. ....	62
Figure 40. (a) SEM images of single silica-coated $Gd_{0.90}Ce_{0.05}Tb_{0.05}BO_3$ samples (b-c-d) double silica-coated $Gd_{0.90}Ce_{0.05}Tb_{0.05}BO_3$ samples. ....	63
Figure 41. FTIR spectra of pure Celecoxib, drug-loaded samples, core/shell and core particles. ....	64
Figure 42. Pore volume vs. relative pressure graph of drug-loaded samples and core/shell samples. ....	66

Figure 43. Pore size distribution of $Gd_{0.90}Ce_{0.05}Tb_{0.05}BO_3@SiO_2$ and drug loaded samples, $Gd_{0.90}Ce_{0.05}Tb_{0.05}BO_3@SiO_2@CLX$ .	67
Figure 44. TGA curves of the core/shell particles and Celecoxib loaded core/shell particles.	68
Figure 45. Magnetization curves of the core, core/shell particles and Celecoxib loaded core/shell particles.	70
Figure 46. Calibration curve prepared by different Celecoxib concentrations in ethanol.	72
Figure 47. Calibration curve prepared by different Celecoxib concentrations in PBS.	73
Figure 48. Celecoxib release profile of $Gd_{0.90}Ce_{0.05}Tb_{0.05}BO_3@SiO_2$ carrier in PBS with a pH of 7.4.	74
Figure 49. MTT result showing the viability of HCT-116 cells after treated with core, empty/drug loaded drug carrier and drug only at different concentrations.	76

## LIST OF ABBREVIATIONS

### ABBREVIATIONS

BET: Brauner-Emmett-Teller

BJH: Barret-Joyner-Halenda

CLX: Celecoxib

COX: Cyclooxygenase

CTAB: Cetyltrimethylammonium Bromide

EDTA: Ethylenediaminetetraacetic Acid

FT-IR: Fourier Transform Infra-Red

MCM: Mobile Composition Matter

PBS: Phosphate Buffer Solution

RE: Rare Earth

SBA: Santa Barbara Amorphous

SEM: Scanning Electron Microscope

TEM: Transmission Electron Microscope

TEOS: Tetraethyl Orthosilicate

UV-VIS: Ultra Violet-Visible

XRD: X-Ray Diffraction





## CHAPTER 1

### INTRODUCTION

#### 1.1. Luminescence and luminescent materials

In recent years, luminescent products and their application attracted attention in many different fields such as bioimaging, plasma TV lasers and lighting devices. Rare earth metals and their compounds are studied broadly for these applications because of their nature, which arise from the unpaired electrons in  $4f$ . In lighting devices, the most commonly used rare earth elements are lanthanum, yttrium, cerium, europium, and terbium; in lasers, ytterbium and neodymium; in medical devices, gadolinium, cerium, lutetium, and terbium (Lucas, 2015). Currently, magnetic nanoparticles and luminescent nanomaterials have incorporated to possess outstanding double functions to drug delivery systems (Li et al., 2019). Nanoparticles as drug delivery agents can be composed of diverse materials such as polymers, lipids and ceramics (Liu et al., 2013).

##### 1.1.1. Fundamental mechanisms of luminescence

Luminescence phenomena involves 2 steps, excitation and emission. Excitation occurs when an energy source hits the electron from ground state to a higher energy state, emission occurs when that electron comes back to the original state by emitting energy. In the luminescence process, the incoming light is absorbed and it loses some of its energy. This energy loss leads to an emission of a light with much greater wavelength than the beginning. This phenomenon is called as Stokes law. The wavelength of emitted light is unique for a luminescent material. After absorption of the radiation, emission occurs with a unique time,  $\tau_c$ , and this parameter determines the class of the luminescence process either as fluorescence or as phosphorescence. The duration of fluorescence is smaller than  $10^{-8}$  seconds and for phosphorescence the

duration is longer than  $10^{-8}$  seconds. A detailed classification of luminescence is shown in Figure 1.

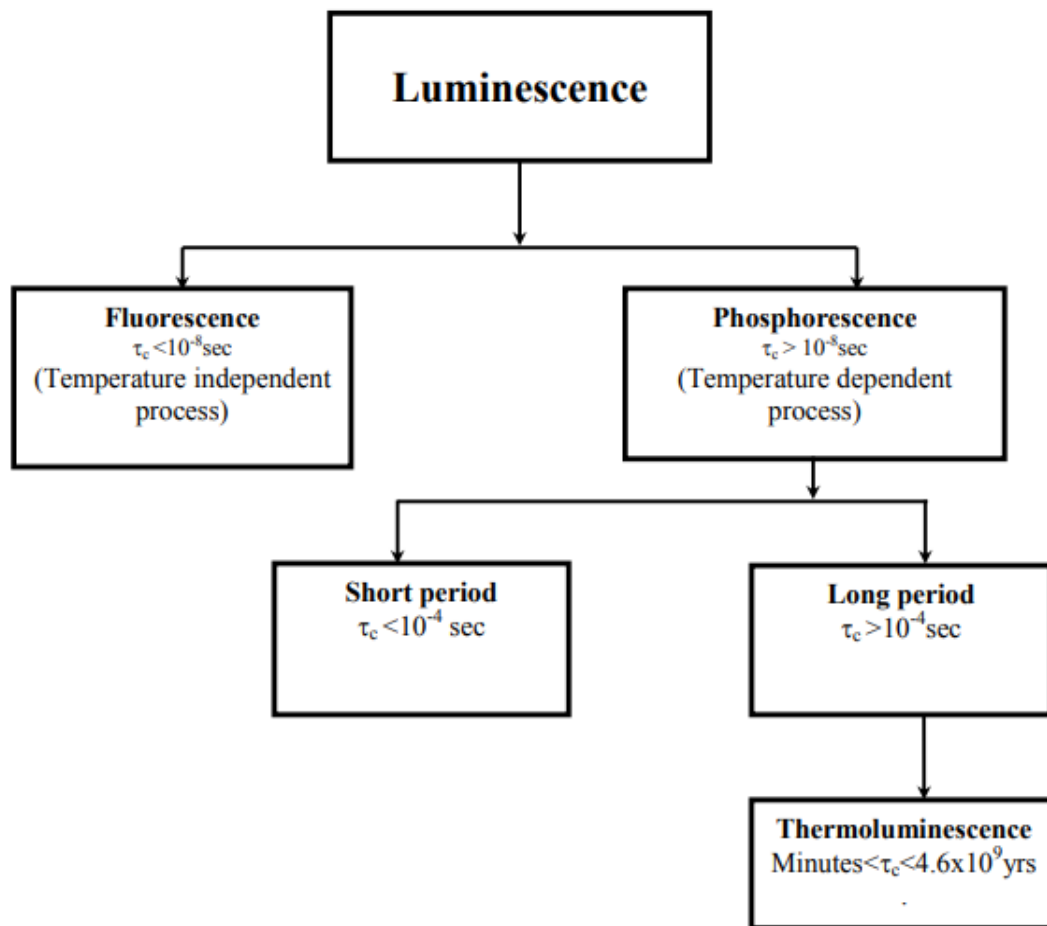


Figure 1. Luminescence types depending on the duration (Murthy & Virk, 2013).

There are two different paths to go back to the ground state, the first one is radiative and the second one is nonradiative Figure 2. Luminescence phenomena occurs in radiative emission path. Non-radiative emission does not participate in luminescence, but it occurs with radiative emission. A powerful luminescent material has radiative path mainly (Murthy & Virk, 2013).

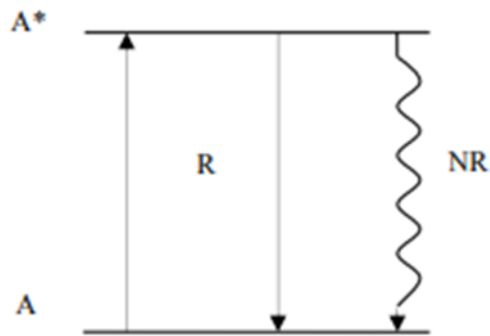


Figure 2. Radiative (R) and nonradiative (NR) paths (Murthy & Virk, 2013).

In general, the energy of luminescent molecules go to higher electronic states by excitation. There are several ways to go back to the ground state which are vibration relaxation, internal conversion and intersystem crossing. This process is represented by a Jablonski energy level diagram (Figure 3).

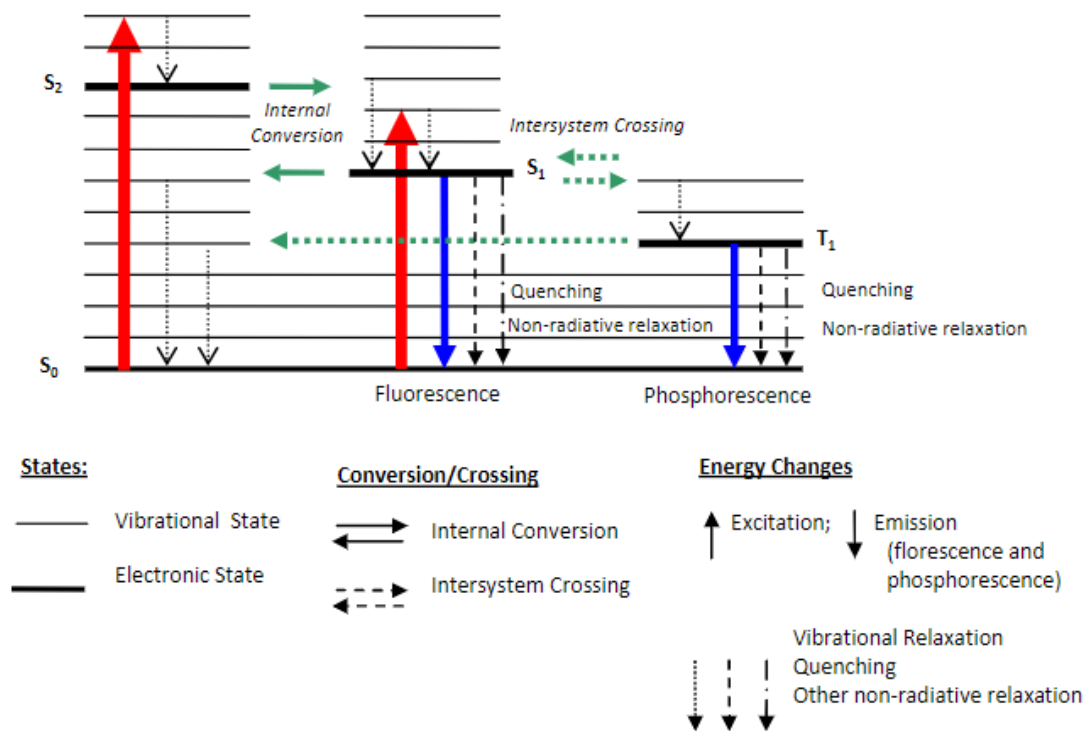


Figure 3. Jablonski diagram (Khalid & Kontis, 2008).

The thick lines in the diagram are the main orbits (singlet and triplet states) and the thin lines are vibrational and rotational energy levels (Khalid & Kontis, 2008). There are many different types of luminescence depending on the generation of the light such as photoluminescence, radioluminescence, cathodoluminescence, electroluminescence, thermoluminescence, chemiluminescence, bioluminescence etc.

### 1.1.2. The quantum yield of luminescence

In photoluminescence, quantum yield,  $\eta$ , is calculated by the following formula where  $N(em)$  is the number of emitted quanta and  $N(abs)$  is the number of absorbed quanta.

$$\eta = \frac{N(em)}{N(abs)}$$

For measurements, fluorescence spectrometer is used with an accessory called integrating sphere. One method to calculate quantum yield is direct excitation. In direct excitation method, the sample is directly excited by a monochromator and then the scatter and the emission of the sample are recorded. The other method is direct-indirect excitation in which the sample is excited by excitation radiation bouncing from the sphere.

In this study, direct excitation method was used to measure the quantum yield of the  $Gd_{0.90}Ce_{0.05}Tb_{0.05}BO_3$  samples. The quantum yield of the samples measured by direct excitation method is calculated by using following equation:

$$\eta = \frac{E_B - E_A}{S_A - S_B}$$

Figure 4 tells us that  $S_A$  and  $S_B$  belong to the excitation scatter region,  $E_A$  and  $E_B$  belong to the emission region. The indices A and B belongs to the experimental setup, A belongs to the reference sample (blank sample) and B belongs to the analyzed sample (Lakowicz, n.d.).

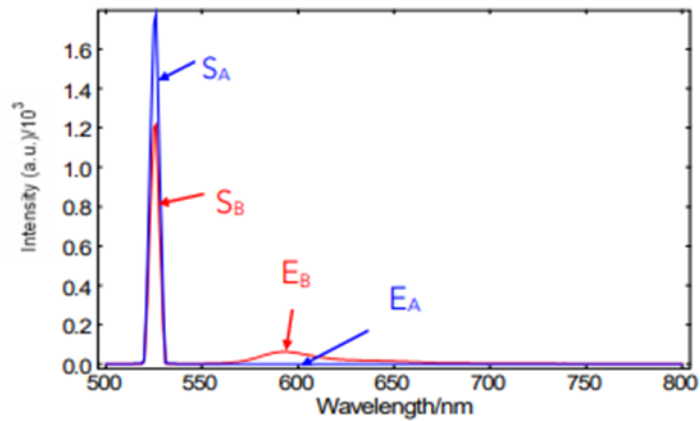


Figure 4. Emission spectra of reference sample A and sample B, where S is scattering, E is emission (Edinst.com, 2019).

### 1.1.3. Luminescent materials

Luminescent materials are mostly inorganic solids composed of a host lattice and generally doped with low concentration of impurities. Energy absorption occurs to activate luminescence and the emission occurs on the doped ions and forms desired emission. Therefore, these impurities are called activator ions. The energy generated by the activator is transferred to a second type of impurity called sensitizer (Figure 5).

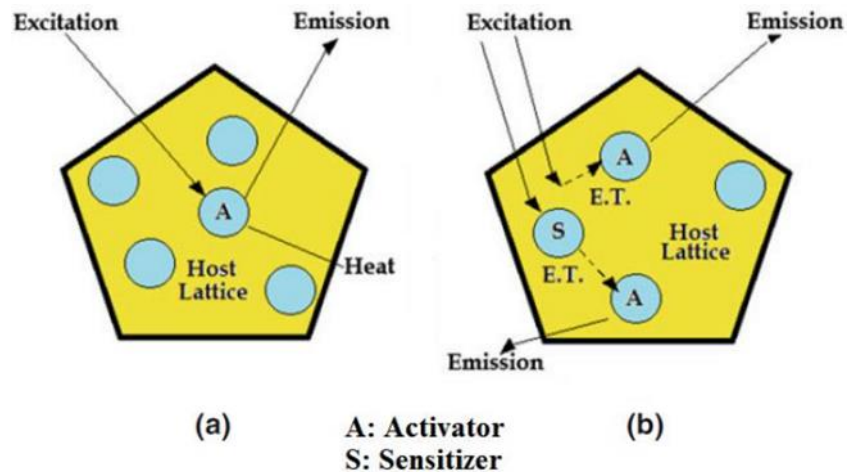


Figure 5. Direct (a) and indirect (b) excitation and energy transfer mechanism (E.T.: energy transfer) (Ronda, 2007).

The concentration of the impurities are usually low since high impurity concentration decreases the luminescence efficiency and this effect is known as concentration quenching. For example, in Figure 6, the luminescence intensities changing with the different mole percentages of  $\text{Yb}^{3+}$  are shown (Bahadur, Yadav, & Rai, 2017). By choosing the proper impurity, the color of the luminescence can be adjusted as desired without changing the host material.

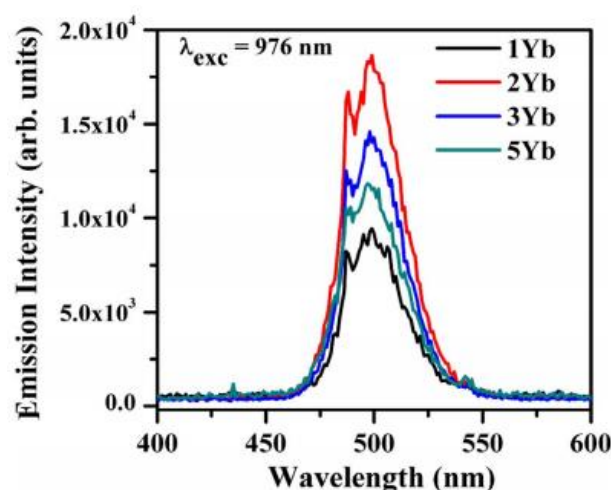


Figure 6. Emission spectra of different amounts of  $\text{Yb}^{3+}$  doped materials (with an excitation wavelength of 976 nm) (Bahadur, Yadav, & Rai, 2017).

Instead of absorption and emission lines, there are bands for electronic transitions in solid materials. In Figure 7, there is the configurational coordinate diagram (CCD) of the bandwidths conforming the separate energy levels. The energy,  $E$ , belongs to the activator-ligand system and configurational coordinate,  $R$ , shows the interatomic space which explains the ligand configuration. To illustrate, the center ion acts as a harmonic oscillator in small displacements. The quantity  $R_0$  represents the equilibrium distance between the ligand and the center ion in ground state,  $g$ . For the first excited state,  $e$ , the distance is shown by  $R_0'$ . The horizontal lines show the vibrational levels ( $0, 1, 2, 3$  and  $0', 1', 2', 3'$  are the levels of ground state and excited state). Figure 7(a) demonstrates the absorption of a photon and non-radiative relaxation. The vertical arrows represent the absorption of a photon. The excitation of a center from ground

state to excited state is called optical absorption transition. In Figure 7(b), there is a return to the lower energy levels (Ruvalcaba, 2016).

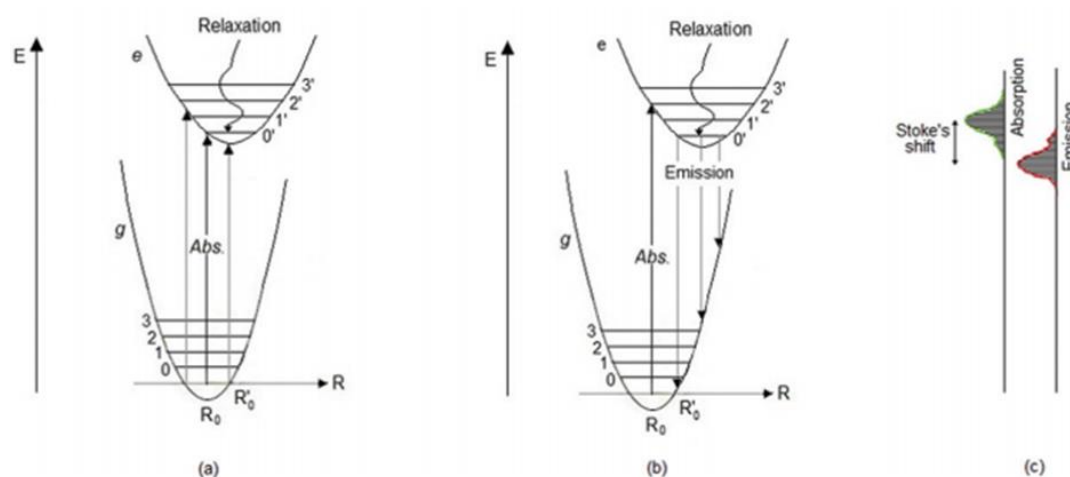


Figure 7. Configurational coordinate diagram with (a) absorption, (b) emission and (c) Stokes' shift (Ruvalcaba, 2016).

#### 1.1.4. Rare earth (RE) ions and their luminescence properties

The rare earths (RE) elements are a group consisting of Scandium, Yttrium and the lanthanides, La, Ce, Pr, Nd, Pm, Sm, Eu, Gd, Tb, Dy, Ho, Er, Tm, Yb, and Lu. These rare earth elements were considered to be present in very little amounts, however they are not actually “rare”. Today, it is known that lanthanides are relatively abundant (Teo, Termini, & Gray, 2016). A valence state of +3 is present for all rare earth elements, but the most stable ones are +4 and +2 since they have either totally empty, half-filled or full *f* shells. Rare earth elements exhibiting +3 valence state show magnetic behavior since they have the highest number of unpaired electrons in *f* shells (Ruvalcaba 2016). The energy level diagram for trivalent  $RE^{3+}$  ions are shown in the Figure 8 known as Dieke diagram (Dieke & Satten, 2005). The diagram provides a fast identification of the energy levels in different host materials and it is understood that the crystal lattice of host material affects the energy levels (Peijzel et al., 2005).



Figure 8. Dieke Diagram of rare Earth ions (Dieke & Satten, 2005).

There are two types of transitions for rare earth ions which are the forbidden  $4f \rightarrow 4f$  transition and  $4f \rightarrow 5d$  transition. The lifetime of the excited state is from micro to milliseconds and the transition takes place between 4f shell and outer 5d shell. These transitions provide a broad emission and sufficient luminescence. Outside matrix affects the emission peak of the rare earth ions and 5d electrons are not shielded by the outer shell (Ma et al., 2018).

The electronic states of the rare earth metals are represented by term symbols. Term symbols have the general formula of  $^{2S+1}L_J$ . The term  $2S+1$  is the multiplicity where  $S$  is total spin angular momentum quantum number,  $L$  is the total orbital angular momentum quantum number and (Toennies, 1970). The electronic states of the rare earth metals are shown in the Table 1.

Table 1. *Electronic states of the rare earth metals.*

Atomic number	Elements	Ground state configuration	RE <sup>3+</sup> ions	S	L	J	Term symbol
			4f electrons	$\Sigma s$	$\Sigma l$	$\Sigma(l+s)$	
21	Sc			0	0	0	
39	Y			0	0	0	
57	La	4f <sup>0</sup> 6s <sup>2</sup> 5d <sup>1</sup>		0	0	0	<sup>2</sup> F <sub>5/2</sub>
58	Ce	4f <sup>1</sup> 6s <sup>2</sup> 5d <sup>1</sup>	↑	1/2	3	5/2	<sup>2</sup> F <sub>5/2</sub>
59	Pr	4f <sup>3</sup> 6s <sup>2</sup>	↑ ↑	1	5	4	<sup>3</sup> H <sub>4</sub>
60	Nd	4f <sup>4</sup> 6s <sup>2</sup>	↑ ↑ ↑	3/2	6	9/2	<sup>4</sup> I <sub>9/2</sub>
61	Pm	4f <sup>5</sup> 6s <sup>2</sup>	↑ ↑ ↑ ↑	2	6	4	<sup>5</sup> I <sub>4</sub>
62	Sm	4f <sup>6</sup> 6s <sup>2</sup>	↑ ↑ ↑ ↑ ↑	5/2	5	5/2	<sup>6</sup> H <sub>5/2</sub>
63	Eu	4f <sup>7</sup> 6s <sup>2</sup>	↑ ↑ ↑ ↑ ↑ ↑	3	3	0	<sup>7</sup> F <sub>0</sub>
64	Gd	4f <sup>8</sup> 6s <sup>2</sup> 5d <sup>1</sup>	↑ ↑ ↑ ↑ ↑ ↑ ↑	7/2	0	7/2	<sup>8</sup> S <sub>7/2</sub>
65	Tb	4f <sup>9</sup> 6s <sup>2</sup>	↑ ↓ ↑ ↑ ↑ ↑ ↑ ↑	3	3	6	<sup>7</sup> F <sub>6</sub>
66	Dy	4f <sup>10</sup> 6s <sup>2</sup>	↑ ↓ ↑ ↓ ↑ ↑ ↑ ↑ ↑	5/2	5	15/2	<sup>6</sup> H <sub>15/2</sub>
67	Ho	4f <sup>11</sup> 6s <sup>2</sup>	↑ ↓ ↑ ↓ ↑ ↓ ↑ ↑ ↑ ↑	2	6	8	<sup>5</sup> I <sub>8</sub>
68	Er	4f <sup>12</sup> 6s <sup>1</sup>	↑ ↓ ↑ ↓ ↑ ↓ ↑ ↓ ↑ ↑ ↑	3/2	6	15/2	<sup>4</sup> I <sub>15/2</sub>
69	Tm	4f <sup>14</sup> 6s <sup>1</sup>	↑ ↓ ↑ ↓ ↑ ↓ ↑ ↓ ↑ ↓ ↑ ↑	1	5	6	<sup>3</sup> H <sub>6</sub>
70	Yb	4f <sup>14</sup> 6s <sup>2</sup>	↑ ↓ ↑ ↓ ↑ ↓ ↑ ↓ ↑ ↓ ↑ ↓ ↑	1/2	3	7/2	
71	Lu	4f <sup>14</sup> 6s <sup>2</sup> 5d <sup>1</sup>	↑ ↓ ↑ ↓ ↑ ↓ ↑ ↓ ↑ ↓ ↑ ↓ ↑ ↓	0	0	0	<sup>2</sup> F <sub>7/2</sub>

#### 1.1.4.1. Photoluminescence properties of Cerium (Ce)

Cerium,  $\text{Ce}^{3+}$ , ion has the lowest  $4f \rightarrow 5d$  transition energy among the lanthanide ions, but there is a large energy gap between  $5d^1$  and the closest level ( $^2F_{7/2}$ ) below causing the  $5d$  level to serve as a light-emitting state. Therefore, the crystal field splitting energy of  $5d$  state and structure of the host crystal determines the luminescence photon energy. Figure 9 shows the energy level diagram of  $\text{Ce}^{3+}$ . There are two emission peaks belonging to the  $\text{Ce}^{3+}$   $4f$  configuration coming from  $^2F_{5/2}$  and  $^2F_{7/2}$  levels.  $\text{Ce}^{3+}$  has the shortest decay time among the lanthanide ions due to the  $d \rightarrow f$  transition being both spin-allowed and parity-allowed (Yen, Shionoya, & Yamamoto, 2007). In addition,  $4f \rightarrow 5d$  transitions lead to a relatively broad absorption and emission bands and high emission intensities. Yang et al. and his/her friends studied the emission spectra of  $\text{Ce}^{3+}$  doped  $\text{GdAl}_3(\text{BO}_3)_4$  phosphors and observed a broad band about 400 nm because of the transition of  $5d \rightarrow ^2F_J$  ( $J=5/2, 7/2$ ) upon 328 nm excitation (Yang & Zhang, 2007). These characteristics facilitate the applications of Cerium in light-emitting diodes (LEDs), inorganic scintillators, and photocatalysis (Qiao et al., 2018).

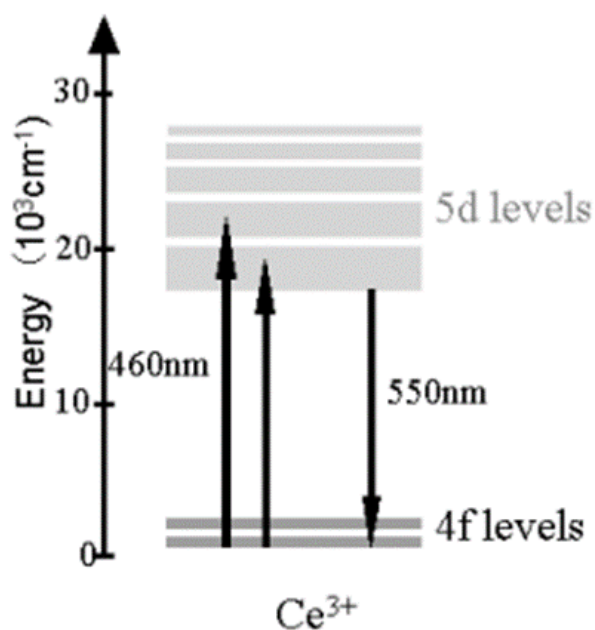


Figure 9. Energy level diagram of  $\text{Ce}^{3+}$  (Yang & Zhang, 2007).

#### 1.1.4.2. Photoluminescence properties of Terbium (Tb)

Among the lanthanide ions,  $Tb^{3+}$  has an intense emission in the visible region with a long lifetime that makes it a promising material in applications from display devices to biological assays (Feng et al., 2008). Emission bands of  $Tb^{3+}$  ion in the visible region arising from the  $^5D_4 \rightarrow ^7F_J$  ( $J=0-6$ ) transitions belong to the green, and  $^5D_3 \rightarrow ^7F_J$  transitions belong to the blue region.

In Figure 10, there is an energy level diagram showing the emissions of  $Tb^{3+}$ . The emission line intensity depends on the  $Tb^{3+}$  concentration and decreases with increasing concentration because of the cross relaxation. Besides, blue to green ratio is also dependent on the  $Tb^{3+}$  concentration and the structure of the host material (Yen, Shionoya, & Yamamoto, 2007). Singh et al. have studied the photoluminescence enhancement in  $Tb^{3+}$  ternary complexes and found a significantly intense emission band at 543 nm corresponding to  $^5D_4 \rightarrow ^7F_5$  transition (Singh et al., 2016). The main transitions of  $Tb^{3+}$  are  $^5D_4 \rightarrow ^7F_6$ ,  $^5D_4 \rightarrow ^7F_5$ ,  $^5D_4 \rightarrow ^7F_4$ , and  $^5D_4 \rightarrow ^7F_3$  which correspond to 489, 544, 586 and 622 nm, respectively (Zhang et al., 2014).

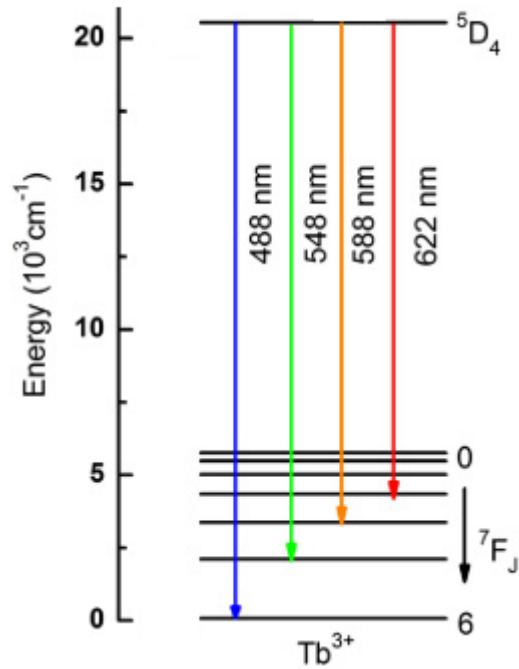


Figure 10. Energy level diagram of Tb<sup>3+</sup> (Duan et al., 2013).

## 1.2. Rare earth borates

Borates are the salts or esters of boric acid (Bates and Jackson, 1987). Borate compounds have been employed in a numerous applications for many decades. Some of the application areas of borates are detergents, polymer additives, glass production, ceramics, agriculture, oil and gas chemicals (Kistler and Helvacı, 1990). Borates can be found as different minerals in nature such as boroxide (B<sub>2</sub>O<sub>3</sub>), Ulexite (NaCaB<sub>5</sub>O<sub>9</sub>.8H<sub>2</sub>O), Kernite (Na<sub>2</sub>B<sub>4</sub>O<sub>7</sub>.4H<sub>2</sub>O), Colemanite (Ca<sub>2</sub>B<sub>6</sub>O<sub>11</sub>.5H<sub>2</sub>O) and Tincal (Na<sub>2</sub>B<sub>4</sub>O<sub>7</sub>.10H<sub>2</sub>O) (Carr, Alsobrook and Austin, 1994). The total reserve of Boron minerals in world is almost 1.3 billion tons and 73 % of the reserves are in Turkey. In Turkey, the total B<sub>2</sub>O<sub>3</sub> production is 1.96 million tons and this makes Turkey the greatest provider in the world. In Eskişehir, Kütahya, Balıkesir and Bursa, there are tincal and colemanite boron minerals found and extracted from mines. There are some other reserves in South America (Peru, Chile, Argentina, Bolivia), Asia

(China, Russia, India) and North America (USA). Table 2 shows the borate reserves by each country (Eti Maden, 2017).

The first study for rare-earth borates was done by Levin et al. in 1961 and they observed that the rare-earth borates have a polymorphous character with three different Calcium Carbonate ( $\text{CaCO}_3$ ) crystal structures which are vaterite, calcite and aragonite (Levin, Roth & Martin, 1961). The important factor determining the crystal structure of the borate is the size of the rare-earth ion ( $\text{RE}^{3+}$ ) (Li et al., 2009). For example, aragonite type is observed when radius ratio of lanthanum and oxygen ions ( $\text{Ln}^{3+}/\text{O}^{2-}$ ) is equal to or greater than 0.71 (Villiers 1971). If the ratio is a value between 0.61 and 0.71, vaterite structure is observed for a lanthanum borate (Chadeyron et al., 1997). Finally, if the radius ratio is smaller than 0.607, the structure changes with the changing reaction temperature and vaterite or calcite is observed (Cox & Keszler, 2002). There are five crystal structures known for the rare-earth borates today, which are monoclinic pseudowollastonite type (C2/c, No.15), hexagonal vaterite type (space group P63/m, No.176), rhombohedral calcite type (R3c, No.161), orthorhombic aragonite type (Pnam, No.62) and the rhombohedral vaterite type (R32, No.155) (Giesber et al., 2003).

Table 2. Global B<sub>2</sub>O<sub>3</sub> stockpile (2017) (Eti Maden, 2017).

Country	Total B <sub>2</sub> O <sub>3</sub> reserve (thousand tons)	Distribution (%)
<b>Turkey</b>	948.712	73.4
<b>Russia</b>	100.000	7.7
<b>USA</b>	80.000	6.2
<b>Chile</b>	41.000	3.2
<b>China</b>	36.000	2.8
<b>Peru</b>	22.000	1.7
<b>Bolivia</b>	19.000	1.5
<b>Kazakhstan</b>	15.000	1.2
<b>Argentina</b>	9.000	0.7
<b>Serbia</b>	21.000	1.6
<b>Total</b>	1.291.712	100

Since boric acid has a low toxicity, rare earth borates are widely used in Hg-free lamps, bioimaging and drug delivery systems (Kubasiewicz et al., 2015).

### 1.2.1. Gadolinium Borate (GdBO<sub>3</sub>)

Gadolinium borate is a hexagonal crystal in rhombohedral space group R32 and adopts vaterite structure. The lattice constants of GdBO<sub>3</sub> crystal are a=6.6357 Å and c=26.706 Å and the volume of the unit cell is 1018.44 Å<sup>3</sup>. In the structure, there are tetrahedral polyborate groups (BO<sub>4</sub>) and they form B<sub>3</sub>O<sub>9</sub><sup>9-</sup> rings. These rings form a layered structure around Gd ions and Gd ions are surrounded by eight oxygen atoms (Ren et al., 1999).

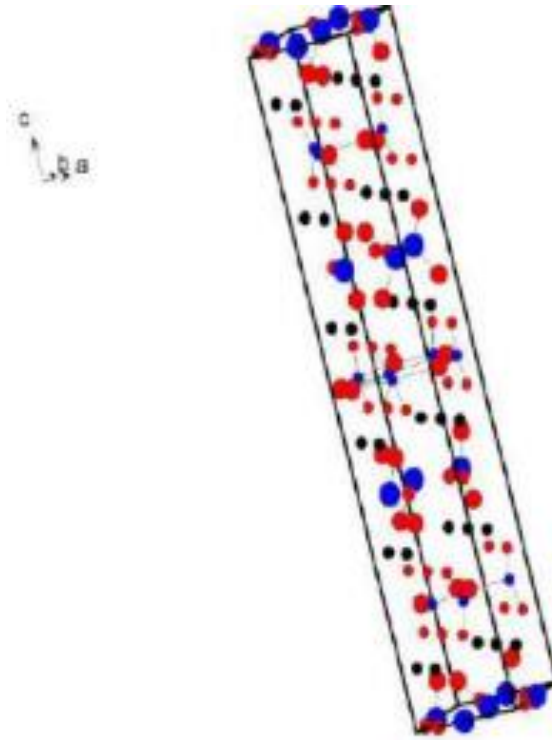


*Figure 11.* Gadolinium borate lattice structure (black spheres: Gd, red spheres: O, blue spheres: B) (Severoğlu 2016).

Figure 11 shows the gadolinium borate structure and Figure 12(a) shows  $B_3O_9^{9-}$  structure. Absorption bands of the stretching and bending modes of  $B_3O_9^{9-}$  rings can be seen in infrared spectra. Stretching mode shows bands around 1105, 970, 900, 810  $cm^{-1}$  and bending mode shows bands around 690 and 565  $cm^{-1}$  (Weir & Lippincott, 1961). The peaks between 900 and 1050  $cm^{-1}$  belong to the characteristic tetrahedral  $BO_4$  borate group (Ren et al., 1999). On the other hand, in a different study Zhang et al. and his/her friends have studied the the neutron diffraction pattern of  $\pi$ -LBO with Rietveld refinement and observed a coexistence of the  $BO_3$  and  $BO_4$  units. Also, this coexistence was verified by FTIR spectroscopy. According to the results, the vibration peaks of the  $BO_3$  units (1408 and 719  $cm^{-1}$ ) and  $BO_4$  units (573, 870, 930, 1014, and 1068  $cm^{-1}$ ) could be explained by the formation of B-O-B bending resulting from the deformation of borate ring (Figure 12b-12c) (Zhang et al., 2015).

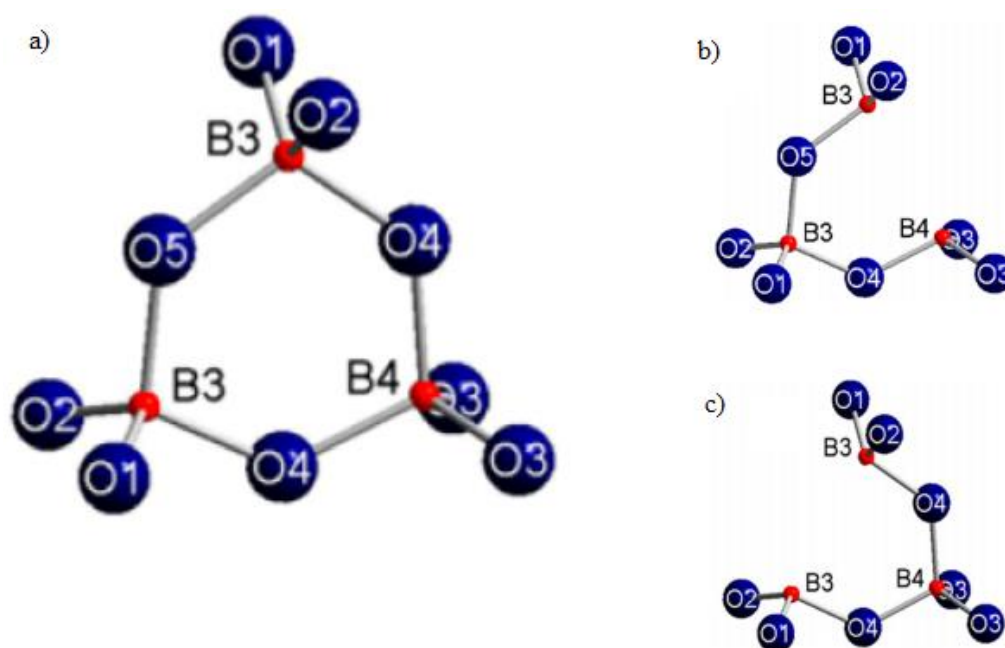


Figure 12. (a) B<sub>3</sub>O<sub>9</sub><sup>9-</sup> ring (b and c) coordination spheres of the B cations without one O4 or O5 (Zhang et al., 2015).

### 1.2.2. Rare earth doped borates

Organic chromophores were used to obtain fluorescent materials, but there were some drawbacks such as short excited state lifetimes and small Stokes' shifts which result in difficult probe signal separation and autofluorescence background. Starting from the mid-80s, lanthanide complexes have successfully replaced organic chromophores since they are easily recognized by their sharp emission lines and they are not sensitive to photobleaching (Bettencourt-Dias, 2014). Rare earth ions with 2+ or 3+ valence states are effective activators for luminescence. Rare earth doped materials with visible emission have a variety of potential applications such as fluorescence imaging, solid state lighting, display monitors, lasers and optical data storage (Dorosz et al., 2015). There are two classes of the luminescence in the visible region which are up-conversion and down-conversion. In up-conversion process, a low-energy light source (NIR light) is used and high-energy visible light emission is observed. For downconversion, there are two or more photons emitted with low energy by absorbing

a high energy photon (Yu Qiao et al., 2018). There are many examples in literature for both downconversion and up-conversion systems. For example, Zhang et al. synthesized a red phosphor on GdBO<sub>3</sub> host doped with Eu<sup>3+</sup>, Ce<sup>3+</sup> and Tb<sup>3+</sup> and studied its photoluminescence excitation and emission properties (Zhang et al., 2014). Kubasiewicz et al. have studied an up-conversion material consisting of GdBO<sub>3</sub> host doped with Yb<sup>3+</sup> and Tb<sup>3+</sup> (Kubasiewicz et al., 2015). Giesber et al. have investigated both LaBO<sub>3</sub> and GdBO<sub>3</sub> hosts synthesized by codoping Eu<sup>3+</sup> and Er<sup>3+</sup> and observed a remarkable up-conversion luminescence intensity for both materials (Giesber et al., 2003). Qin et al. have observed a promising luminescence intensity for aragonite type LaBO<sub>3</sub> doped with Eu<sup>3+</sup> and Tb<sup>3+</sup> nanofibers (Qin et al., 2013).

### **1.3. Synthesis methods of inorganic phosphors**

The most commonly used methods to synthesize inorganic phosphors are solid-state synthesis, hydrothermal synthesis, sol-gel synthesis, microwave assisted synthesis, high temperature synthesis and combustion synthesis (Wiwattanapongpan et al., 2007). Each method has its own advantages and disadvantages. In solid-state synthesis route, preparation of precursor materials in a desired composition homogeneously is the main issue. All components in the homogeneous mixture are completely diffused to obtain the proper composition. In a typical synthesis, inorganic solids are finely divided to be obtained as powders, then mixed well and heated. This method cannot provide high-quality materials due to the encountered diffusion barriers causing a nonhomogeneity (Seneci, 2000).

Hydrothermal synthesis is a homogeneous or heterogeneous reaction occurring in a closed system with a pressure larger than 1 atm, at high temperatures and this reaction includes a proper solvent (Byrappa & Yoshimura, 2013). The reaction media is kept at high temperatures under a high pressure for certain time intervals and crystal growth occurs in a steel cylindrical container called autoclave. In hydrothermal synthesis, it is possible to obtain the desired morphology and size of the particles by changing the reaction conditions, temperature, pressure and time (Shyichuk, 2015). Additionally, it

is possible to collect high-quality, homogeneous and pure products without calcination step (Wang et al., 2010).

In combustion synthesis, the reactants can be in solid, liquid or gaseous phases. There is a mixture of an aqueous solution of oxides or metal salts and a fuel. This mixture is heated up to a high temperature that starts the ignition, then combustion happens and forms ultrafine solid particles (Liu, Chen, & Li, 2018). Combustion synthesis provide a fast removal of the organic species and solvent, enables the formation of small-sized phosphors (Alves, Bergmann & Berutti, 2013). However, there is a drawback of this synthesis which is the presence of carbon in large amounts in the final product (Kumar D., Kumar B. & Mahesh, 2018).

### 1.3.1. Sol-gel synthesis

Sol-gel techniques have been used since the 80s. It has a simple synthesis route and also it is a cost-effective and convenient method. Sol-gel synthesis starts from the precursor materials which are mixed to obtain the sol. The second step is the pyrolysis in which the organic materials are converted to gases. High temperatures are applied to decompose the organic matrix completely and then crystallization is obtained. In sol-gel synthesis, there is a formation of metal-oxygen bonds (M-O-M bonds) causing a crosslinking. The major steps of the process are condensation and hydrolysis, as follows:



During hydrolysis step, the alkoxy group (OR) is converted to a hydroxyl group (OH). Condensation reactions start the M-O-M bond formation. In condensation, one OH-group may bind to another to form an oxygen bridge. When it binds to an alkoxy group, an alcohol (ROH) will be obtained (Livage & Pierre, 2016). When hydrolysis and condensation occur at the same time, gelation of the sol is observed. The first

applied sol-gel synthesis is the formation of spherical monodisperse silica particles, known as Stöber-process. In Stöber process, an alcoholic solution of tetraethyl orthosilicate (TEOS) is used as the silica source. As a catalyst for gelation, a base is used, e.g. sodium hydroxide, ammonia, and the base also starts the formation of silica spheres. The particle size can be adjusted by using different type of alcohol and water content (Antoni, Tag & Ensinger, 2015).

#### **1.4. Drug delivery systems**

The pharmacological properties of the drugs are improved by proper drug delivery systems and these systems are allowed by Food and Drug Administration (US FDA) (Hwang, Jeon, & Kim, 2010). There are two classes of drug release according to US FDA, immediate release and modified release. The drug is released soon after the drug is taken for the immediate release type and drug release occurs after some time for modified release. The aim in modified one is to reduce dosing frequency, side effects and to enhance bioavailability of the drug (Allen & Cullis, 2004). In recent years, many drugs need an appropriate delivery system even though they are powerful for treatment of a disease. The problems such as poor solubility, limited effectiveness, side effects and high dosing frequency can be overcome by a proper drug delivery system (Nevozhay et al., 2007). Moreover, there are many advantages of an improved drug delivery system such as decreasing the side effects, keeping the drug levels in a therapeutically pleasing range, preventing overdose, decreased number of dosing frequency and dosage, improving the effectiveness and stability of the drug (Langer, 1998). As can be seen from the Figure 13, the concentration of the therapeutic agent in a conventional tablet or capsule reaches a toxic level with every dose. Additionally, the effective concentration of the drug in therapeutic level cannot be maintained for a long time. However, optimal concentration of the drug in therapeutic level can be prolonged with a proper drug carrier (Vallet-Regi, Balas & Arcos, 2007).

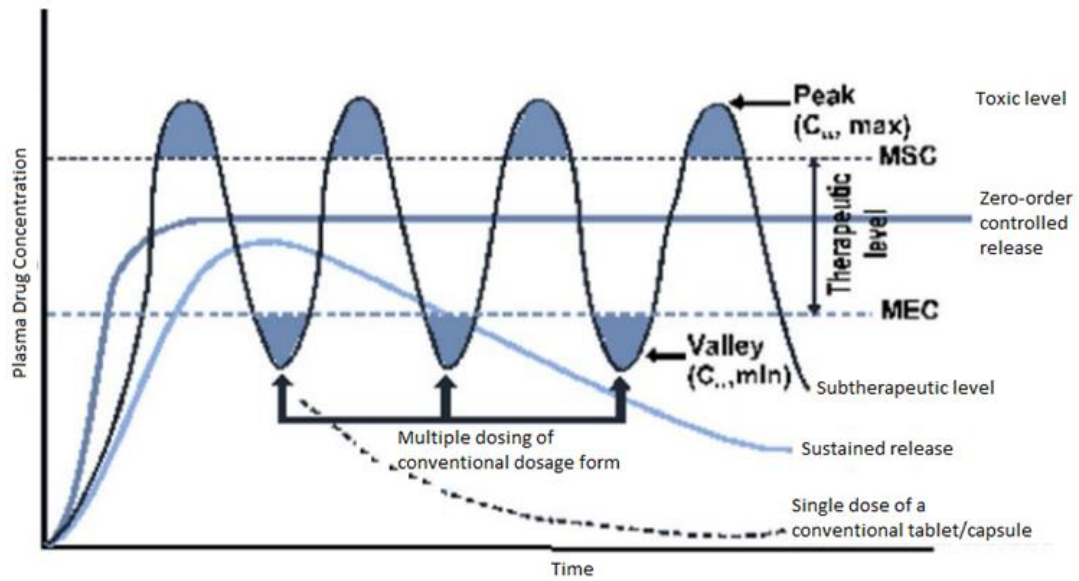


Figure 13. Drug concentration vs. time profile for single dose and multiple dose of conventional, sustained and controlled delivery formulations. (MSC: Minimum safe concentration, MEC: Minimum effective concentration) (Vallet-Regi, Balas & Arcos, 2007).

In order to find an ideal drug carrier, various materials and methods were used. Mostly, nanoparticles and nanoformulations were used as drug carriers with a great success and still nano-sized drug carriers have great potential for many application areas such as gene therapy, radiotherapy and delivery of proteins, vaccines, antibiotics, anti-tumors and AIDS therapy. There are many advantages of using nanoparticles as drug carriers including drug targeting, delivery, release and additionally they have a great potential to integrate diagnosis and therapy (Tiwari et al., 2012). The examples for nano-sized drug carriers are polymeric nanoparticles (PNPs) such as polyacrylamide, polyacrylate, natural polymers like albumin, DNA, chitosan, gelatin; mesoporous silica products such as MCM-41 (Mobil Composition of Matter) and SBA-15 (Santa Barbara University mesoporous silica material) (Sevimli & Yılmaz, 2012), (Eren et al., 2016), (Günaydın & Yılmaz, 2015); carbon-based nanomaterials such as single-walled carbon nanotube (SWCNT), multi-walled carbon nanotube (MWCNT). Even though there are many proper nano drug carriers found, scientists have studied to track the drug carrier in the body by bringing luminescent or magnetic properties to drug

carriers and they have used nanoparticles for these purposes since surface modification is easy for nanoparticles (Wilczewska et al., 2012).

It is important to enhance drug loading and release properties by increasing surface interactions between drug and the carrier to reach an effective controlled drug release. For example, SBA-15 drug carrier has only silanol groups on the surface and inside the channels, forming weak interactions with the drug, so the interactions are not efficient that the sustained release cannot be maintained. Therefore, Song et al. have attached amine groups on the surface of SBA-15 particles for Ibuprofen release. The surface of functionalized SBA-15 is positively charged by amine group and becomes hydrophilic, leading to a strong interaction between drug and the carrier and also a sustained release (Andersson et al., 2004), (Song, Hidajat, & Kawi, 2005).

#### **1.4.1. Polymeric matrices**

Polymers have an important role in the improvement of drug delivery systems by providing controlled release of therapeutic agents in constant doses over long periods, tunable dosage and release of both hydrophilic and hydrophobic drugs. In the last 50 years, many different techniques were developed to combine polymers with bioactive agents such as spray coating, compression and encapsulation. For this combination various cellulose derivatives were used such as poly(ethylene glycol) PEG, and poly(N-vinyl pyrrolidone). Polymers used for drug delivery purposes can be classified as diffusion-controlled, solvent-activated, chemically controlled and externally-triggered systems (Liechty et al., 2010). The choice of polymer, in addition to its physicochemical properties, is dependent on the need for extensive bio-chemical characterization and specific preclinical tests to prove its safety. Surface properties such as hydrophilicity, lubricity, smoothness and surface energy govern the biocompatibility with tissues and blood (Pillai & Ramesh, 2001).

#### **1.4.2. Core/shell structures**

Core/shell particles are widely used in drug delivery systems. They can be used to encapsulate drugs since they are biocompatible. The core is not affected by the

conjugated molecules. The selection of core and shell types depends on the multifunctionality of the materials. Then, the surface can be modified depending on the purpose of the drug carrier such as targeting the tumor cells (Sounderya & Zhang, 2010).

In literature, there are many examples to core/shell nanostructures used as drug carriers. The synthesis of a core/shell particle includes a surfactant and micelle formation. Micelles are simple supramolecules formed by amphiphiles and amphiphiles are molecules composed of a hydrophobic and a hydrophilic tail. Hydrophobic parts gather together and form the micelle core where hydrophilic heads stay outside and form a phase barrier to water. In recent decades, large scale of new amphiphiles (surfactants) have been synthesized and used to form different types of core/shell materials (Dwars, Paetzold, & Oehme, 2005). In drug delivery systems a biologically inert drug carrier must be produced. In order to procure a biocompatible, non-toxic drug carrier, silica is used widely as shell in the core/shell type carriers. Furthermore, it is easy to introduce organic functional groups to silica, either through covalent bonding or electrostatic interactions and this provides a high level of versatility (Caruso et al., 2012).

#### **1.4.2.1. Inorganic/Inorganic Core/Shell Materials**

Core and shell can be composed of organic or inorganic materials with different combinations and the most important one is inorganic core/inorganic shell materials since they have a huge application area. The most widely used shell material is silica for inorganic/inorganic core/shell systems because it stabilizes the suspension of the core material. Also, silica is the most chemically inert material available; it can block the core surface without interfering in the redox reaction at the core surface. In the experimental part there are many parameters to control the shell thickness such as coating time, concentration of reactants, catalyst, and other precursors. When there is a microemulsion system in the synthesis of the particles, it was found that with the increasing molar ratio of water to surfactant has a crucial role in particles size and

particle size distribution. All these parameters should be optimized for the desired core/shell system. Core/shell structure provides a multifunctionality to the particles such as magnetism and fluorescence. For example, magnetic iron oxide, Fe, Ni, Co, and super paramagnetic iron oxide (SPION) core particles with suitable shell coatings are used in in-vivo drug release. Since lanthanide earth metals have good fluorescence and photoluminescence properties, lanthanide metal salts with suitable biocompatible inorganic shell coatings are also used for bioimaging and biodetection purposes in living systems (Chaudhuri & Paria, 2012). For example, in 2017, Xia et al. synthesized a luminescent Yb<sup>3+</sup> and Er<sup>3+</sup> doped Gd<sub>2</sub>O<sub>3</sub> core and coated this core with SiO<sub>2</sub> by a cationic surfactant cetyltrimethylammonium bromide (CTAB) (Xia et al., 2017). Similarly, Szczeszak et al. prepared a Eu<sup>3+</sup> doped GdVO<sub>3</sub> core and coated this core with SiO<sub>2</sub> to use this product in drug delivery applications (Szczeszak et al., 2016)

### **1.5. Hydrophobic drugs**

Among all the drug delivery routes, oral ingestion is the most common and expedient way since it is cost-effective, highly patient-compliant, flexible in dosage form and it has almost no sterility constraints. Therefore, a majority of the generic drug companies tend to produce bioequivalent oral drugs (Kannao et al., 2014). However, there is a big problem with the design of these drugs that they have poor bioavailability. Bioavailability relies on some factors such as dissolution rate, drug permeability, solubility, susceptibility and the most common reasons for low bioavailability are poor solubility and low permeability. In order to obtain desired pharmacological response, it is important to reach a proper drug concentration and solubility of the drug must be enhanced to reach the right drug concentration. High doses are needed to attain therapeutic plasma concentrations after oral administration for a poorly soluble drug (Savjani, Gajjar, & Savjani, 2012).

#### **1.5.1. Celecoxib**

Celecoxib is a nonsteroidal anti-inflammatory drug (NSAID) and also an analgesic (painkiller). It inhibits cyclooxygenase (COX) enzyme since it has antipyretic

activities. There are two main COX enzymes, COX-1 works for GI cytoprotection and homeostasis, COX-2 provokes inflammation. Nonsteroidal drugs are not particular for prostaglandin enzyme synthesis but Celecoxib inhibits COX-2 enzyme selectively. Nonsteroidal drugs like Celecoxib can be used as an anticancer drug because they have a beneficial influence on reducing the risk of colon cancer. Celecoxib is 4-[5-(4-Methylphenyl)-3-(trifluoromethyl)-1H-pyrazol-1-yl] benzenesulfonamide. The empirical formula of Celecoxib is  $C_{17}H_{14}F_3N_7O_2S$ , and its molecular weight is 381.37 g/mole. The solubility of Celecoxib in water changes between 3-5 mg/L. (Ehlich, Franciscano, & Andradas, 2005), (Tunc, Severcan, & Banerjee, 2012).

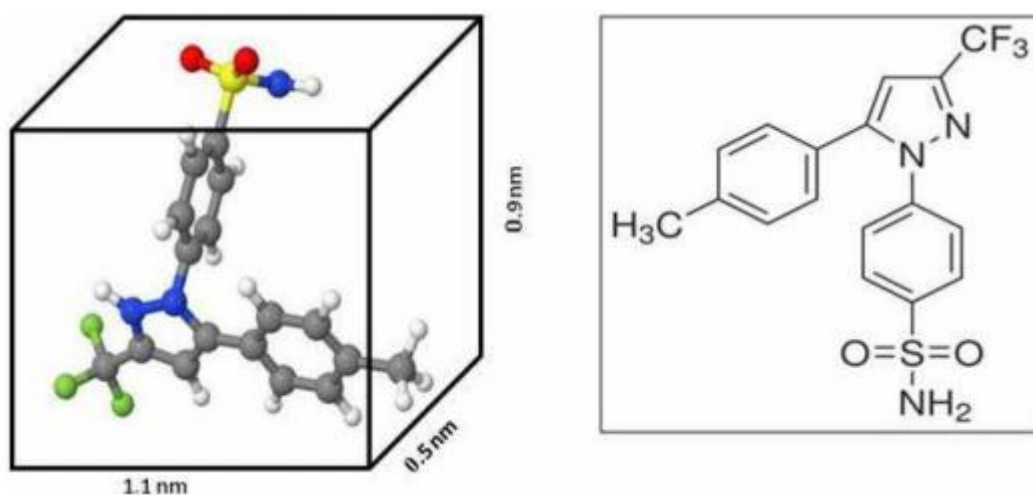


Figure 14. Chemical structure of Celecoxib (Günaydın & Yılmaz, 2015).

### 1.6. Multifunctionality of nano-drug carriers

Nanoparticles are formed in two stages; nucleation and crystal growth. Crystal growth occurs by the deposition of the atoms on a crystal surface. There are some methods to synthesize different types of nanoparticles such as thermal decomposition, coprecipitation, hydrothermal synthesis, sol-gel synthesis etc. and in these methods, similar capping agents and solvents are used. Recently, several simple coating methods have been applied to inorganic nanocrystals such as polymer grafting on the surface via metal chelation, nanoparticle-nanoparticle assembly and nanoparticle-

small molecule assembly. Also, mesoporous silica coating methods have been examined for many hydrophobic and hydrophilic inorganic nanoparticles. These ordinary synthesis methods provide different combinations of nanoparticles with small molecules having multifunctional properties such as magnetic resonance imaging, in vivo optical imaging, magnetic drug targeting, drug delivery combination with thermal therapy (Bao, Mitragotri, & Tong, 2013).

Surface functionalization of drug carriers enables an interaction between drug carriers and the biological system, so a well-designed drug delivery system is exposed to surface modifications to induce some certain properties such as high biocompatibility, strong attraction between the drug carrier and biomolecules, specific targeting sites and high charge density. Such functionalization leads the material to be used for various biomedical applications. Surface modification depends on the surface properties of the material and it is specified according to the kind of the product. For example, quantum dots are functionalized by coordinating ligands and amphiphilic polymers, carbon nanotubes and graphene are functionalized with the suitable chemical groups since without functionalization, they are cytotoxic (Sao, Vaish, & Sinha, 2015).

### **1.6.1. Drug loading and release properties**

Nanoparticles have been used in advanced drug delivery systems involving liposomes, polymeric micelle structures, mesoporous silica and carbon nanotubes. Drug loading to these particles occur by many different mechanisms such as hydrogen bonding, surface adsorption, embedding and other types of interactions. However, drug loading efficiency is still low for currently used drug carriers. Therefore, it is important to improve a drug carrier with a high drug loading efficiency (Yang et al., 2008). There are many examples to methods used to increase drug loading capacity, for example; Yang et al. and his/her friends have studied a core/shell type drug carrier and used mesoporous silica as shell, by this way, surface area is increased and a large surface area allows the carrier to adsorb much more amount of drug on the silica surface and

inside the pores (Yang et al., 2009). Similarly, Xia et al. have studied  $\alpha\text{-Fe}_2\text{O}_3@Y_2\text{O}_3:\text{Eu}^{3+}$  functionalized particles and obtained a highly improved drug loading efficiency (Xia et al., 2017). Slow drug release is also important for drug delivery systems. In order to control drug release, hydrogen bonding and hydrophobic interaction, encapsulation of the carrier with a polymeric material, mild acidic pH triggers and photothermal release have been used. Using Doxorubicin (DOX) as a pH controlled release example, Wang et al. have studied the DOX loading on graphene-based nanocarriers via hydrogen bonding and hydrophobic interaction. According to the study, if there is a decrease in pH value, the amine groups present in DOX molecule will be rapidly protonated and the hydrogen bonding between the drug and carrier will be weakened, resulting in the release of the DOX drug (Wang et al., 2014).

### **1.6.2. Visualization**

The structure and functional properties of cells, organs and living organisms are hard to understand, so there is a need for development of imaging techniques with high sensitivity and resolution. Luminescence imaging owns these features in addition to high penetration depth (Bettencourt-Dias 2014). Also, the magnetic targeting ability is important because it helps to track the location of chemotherapeutic agents for anticancer treatment inside the body (Wang et al., 2014). In order to improve a multimodal imaging functionality, researchers have used magnetic nanoparticles in combination with luminescent materials (Narayanan et al., 2012).

#### **1.6.2.1. Luminescent drug carriers**

Functionalized drug carriers with luminescence properties have attracted attention in recent years, since these materials have a high potential to be used as bioimaging agents. There are many different materials used for bioimaging purposes such as quantum dots, organic dyes with a core-shell structure. However, quantum dots are chemically less stable, toxic and organic dyes have a rapid photobleaching. Therefore, most recently rare earth based materials are used as the luminescent bioimaging agents in biological applications. In previous studies, many different rare earth compounds

were used either as single doped and co-doped forms to achieve a high luminescence intensity. However, the nature of the rare earth compounds is not always suitable for the drug loading and release processes, so they are functionalized by different drug loading matrices such as silica and hydroxyapatite (Gai et al., 2010).

#### **1.6.2.2. Magnetic drug carriers**

Magnetic nanoparticles are important for clinical applications and therapeutic methods. They have incomparable characteristics and capability to function in the biological environment with enhanced interactions. Magnetic nanoparticles have different applications for multifunctional purposes as contrast agents in magnetic resonance imaging drug carriers. Many different types of magnetic nanoparticles were improved for biomedical applications such as iron oxide nanoparticles, metallic nanoparticles, nonmetallic nanoparticles and these nanoparticles were functionalized by different core/shell combinations and surface modifications. In recent years, magnetic nanoparticles have been used to monitor high resolution anatomical images such as cancer imaging, cardiovascular disease imaging and molecular imaging (Sun, Lee, & Zhang, 2008).

Paramagnetic metal ions with one or more unpaired electrons can be used as MRI contrast agents. The most commonly used contrast agents are Gadolinium ( $Gd^{3+}$ ) and manganese ( $Mn^{2+}$ ). In addition, superparamagnetic materials are also used as contrast agents which are classified as ultra-small superparamagnetic  $Fe_3O_4$  particles (smaller than 50 nm), micron-sized iron oxide particles and superparamagnetic iron oxide particles. (Geraldès & Laurent, 2009).

In literature, there are many examples to magnetic drug carriers. For example, Wang et al. have developed a new method to produce magnetic manganese oxide nanoparticles and proved their superior characteristics for targeted MRI contrast agents in tumors and for drug loading capacity (Shin et al., 2009). In another study, scientists have developed an iron oxide based magnetic drug carrier with dual functional properties by using a water-insoluble drug, Doxorubicin. They have

obtained both a useful drug carrier for cancer therapy and a magnetic resonance imaging contrast agent (Jain et al., 2008). Padhye et al. have developed Gd based nanoparticles with excellent paramagnetic properties which makes them suitable for magnetic resonance imaging applications (Figure 15) (Padhye et al., 2015).

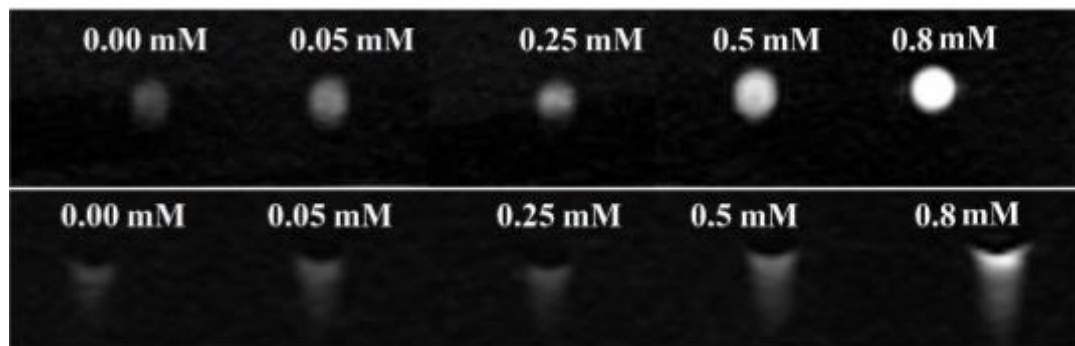


Figure 15.  $\beta$ -NaYF<sub>4</sub>:Gd<sup>3+</sup>/Tb<sup>3+</sup> nanorods and (f)  $\beta$ -NaYF<sub>4</sub>:Gd<sup>3+</sup>/Tb<sup>3+</sup>- DOX conjugate at various molar concentrations in water (Padhye et al., 2015).

### 1.7. Aim of the work

In this research, the aim is to synthesize multifunctional core/shell type nanostructures and to study their drug loading and release properties by using Celecoxib drug. Celecoxib drug was chosen since it is hydrophobic and poorly soluble, so the dissolution rate and solubility of this drug must be enhanced. Firstly, a magnetic and luminescent Ce<sup>3+</sup> and Tb<sup>3+</sup> co-doped GdBO<sub>3</sub> core was synthesized by using sol-gel method. Then, the core was coated with mesoporous transparent silica layer by modified Stöber method in order to obtain high biocompatibility and surface area which enhances the drug loading capacity. In literature, Kubasiewicz and his/her colleagues have synthesized a similar material, silica coated Yb<sup>3+</sup> and Tb<sup>3+</sup> doped GdBO<sub>3</sub> nanostructures by using Triton X-100 (TX-100) and EDTA as chelating agent. They have discussed the up-conversion photoluminescence properties of these particles, however they did not mention magnetization analyses, drug loading-release studies and toxicity experiments (Kubasiewicz et al., 2015). In our study, instead of Yb<sup>3+</sup>, Ce<sup>3+</sup> was chosen as sensitizer and down-conversion photoluminescence was

observed. In sol-gel synthesis method, citric acid and EDTA were used as chelating agent and their differences were discussed in results part. Also, drug loading procedure was applied in ethanol by inserting the drug inside the silica pores by post-grafting method and drug release experiments were done in pH 7.4 phosphate buffer solution (PBS). Finally, toxicity of the drug carrier was tested.

## CHAPTER 2

### EXPERIMENTAL

#### 2.1. Materials

Gadolinium (III) oxide ( $Gd_2O_3$ , Mw=362.50 g/mole, 99.9%), cerium (III) carbonate ( $Ce_2(CO_3)_3 \cdot xH_2O$ , Mw=460.27 g/mole, 99.9%) and terbium (III,IV) oxide ( $Tb_4O_7$ , Mw=747.69 g/mole, 99.9%) were purchased from Aldrich. Poly (ethylene glycol)-block-poly (propylene glycol)-block-poly (ethylene glycol) ( $C_3H_6O \cdot C_2H_4O$ )<sub>x</sub>, Mw=5800 g/mole), Citric acid ( $C_6H_8O_7$ , Mw=192.124 g/mole) and tetraethyl orthosilicate (TEOS) ( $(C_2H_5O)_4Si$  Mw=208.33 g/mole) were obtained from Sigma-Aldrich and EDTA (ethylenediaminetetraacetic acid,  $C_{10}H_{14}N_2O_8K_2$ , Mw= 368.4 g/mole, 98%), boric acid ( $H_3BO_3$ , Mw=61.833 g/mole) from Sigma. Nitric acid (65%,  $HNO_3$ , d=1.39 kg/L) and ethanol (d=0.79 kg/L) were purchased from Merck.

#### 2.2. Synthesis of $Gd_{1-x-y}Ce_xTb_yBO_3$ core

$Gd_{1-x-y}Ce_xTb_yBO_3$  particles are synthesized by using Pechini sol-gel method. Stoichiometric amount of  $Gd_2O_3$ ,  $Tb_4O_7$  and  $Ce_2(CO_3)_3 \cdot xH_2O$  are dissolved in nitric acid ( $HNO_3$ , 65%) and heated to evaporate all the extra acid. Obtained rare earth nitrate salts are dissolved in sufficient amount of deionized water. In a different beaker, boric acid, EDTA and PEG solution is prepared. Rare earth nitrate solutions are added to this solution dropwise with vigorous stirring. This mixture is heated to 80°C until a homogeneous gel forms. The formed gel is calcined at 900°C for 2 hours. Finally, a white powder of  $Gd_{1-x-y}Ce_xTb_yBO_3$  is obtained.

#### 2.3. Silica coating to $Gd_{1-x-y}Ce_xTb_yBO_3$

As-prepared  $Gd_{1-x-y}Ce_xTb_yBO_3$  particles are dispersed in ethanol and ultrasonication is applied for 30 minutes. The mixture is centrifuged and re-dispersed in 160 mL

ethanol, 40 mL deionized water and 2 mL NH<sub>3</sub>. Subsequently, sufficient amount of CTAB is added to this solution and stirred for half an hour. After that, TEOS is introduced to the solution dropwise, mixed for 4 hours and 12 hours of aging is applied. The mixture is centrifuged and solid material is air-dried for 1 day. At the end, calcination is done at 550°C for 6 hours to obtain mesoporous structure.

For double silica coating, single coated particles are dispersed in water/ethanol mixture in the same ratio used for single coating. The surfactant is added to the mixture and mixed for 30 minutes. After that, TEOS is added to the mixture very slowly. The mixture is stirred for 4 hours and 12 hours of aging time is applied. The obtained particles are separated by centrifugation, dried and calcined at 550°C for 6 hours.

#### **2.4. Celecoxib loading**

For Celecoxib loading, ethanol was used as the solvent in liquid-phase grafting method. Gd<sub>1-x-y</sub>Ce<sub>x</sub>Tb<sub>y</sub>BO<sub>3</sub>@SiO<sub>2</sub> nanoparticles (100 mg) were taken in a beaker and mixed with 100 mg of Celecoxib in 50 ml of ethanol. Ultrasonication was done for 30 minutes and the mixture was vigorously stirred at room temperature for 24 and 48 hours (separate replicates). Celecoxib loaded Gd<sub>1-x-y</sub>Ce<sub>x</sub>Tb<sub>y</sub>BO<sub>3</sub>@SiO<sub>2</sub> nanoparticles were separated with centrifuge with 4100 rpm, washed with deionized water and ethanol, dried at room temperature for 1 day. In order to calculate the amount of the drug, UV-VIS analysis was done at 254 nm wavelength. Also, TGA was done to verify UV-VIS results. Beer-Lambert law was used to calculate the concentration of the drug. Drug loading efficiency was calculated from the following equation:

$$\text{Drug loading efficiency} = \frac{\text{Weight of Celecoxib in the sample}}{\text{Weight of carrier in the sample}}$$

#### **2.5. Celecoxib release**

Celecoxib release studies were done by using a pH 7.4 phosphate buffer solution (PBS). Celecoxib loaded Gd<sub>1-x-y</sub>Ce<sub>x</sub>Tb<sub>y</sub>BO<sub>3</sub>@SiO<sub>2</sub> samples (50 mg) were mixed in 50 ml of PBS at 37°C. Drug release was determined at 30 minutes, 1 hour, 2, 4, 6, 12 and 24 hours. For each time, 5 mL of the sample was taken from the mixture and 5 mL of

fresh PBS was added to the mixture. Supernatant solution was obtained with centrifuge and kept for UV-VIS analyses. Absorbance data coming from UV-VIS spectrometer were used to calculate the amount of drug released from  $Gd_{1-x-y}Ce_xTb_yBO_3@SiO_2$  samples by Beer Lambert law.

Table 3. *Chemicals used to prepare PBS.*

Chemicals	m(g) or V(L)	Brand	MW(g/mole)
$KH_2PO_4$	0.24 g	Merck	136.02
$Na_2HPO_4$	1.44 g	Merck	142.00
$H_2O$	1.0 L	-	18.00
NaCl	8.00 g	Sigma	58.44

## 2.6. Cell proliferation assay

For the cytotoxicity experiments, HCT-116 human colon cancer cell line was used. The cells were obtained from Deutsche Sammlung von Mikroorganismen und Zellkulturen (Braunschweig, Germany). A phenol red-free RPMI-1640 medium was used for cell growth which was supplemented with 1.5 mM L-Glutamine, 10 % FBS, 1 % penicillin-streptomycin and 2.5  $\mu$ g/mL plasmocin (Invivogen, San Diego, California, United States) was added to reach a final concentration for mycoplasma contamination. Cell growth was done in a humidified atmosphere with 5 %  $CO_2$  at 37°C. The cell culture media and supplements were purchased from Biological Industries (Beit Haemek, Israel). In order to determine the effect of  $Gd_{90}Ce_5Tb_5BO_3$  core, empty  $Gd_{90}Ce_5Tb_5BO_3@SiO_2$  particles and  $Gd_{90}Ce_5Tb_5BO_3@SiO_2@CLX$  complexes, as well as pure Celebrex on proliferation of HCT-116 cell line, a colorimetric 3-(4,5-dimethylthiazol-2-yl)-2,5 diphenyl tetrazolium bromide (MTT) assay was used. The samples were autoclaved at 120°C for 15 minutes, then re-suspended in a sterile cell culture medium for the preparation of the stock solution at

a concentration of 1 mg/ml. HCT-116 cells were seeded in a 96-well plate at  $1 \times 10^4$  cells per well and allowed to attach for 24 h. The cells were then treated with 500, 100, 50, 10 and 1  $\mu\text{g/mL}$  concentrations of  $\text{Gd}_{90}\text{Ce}_5\text{Tb}_5\text{BO}_3$  core,  $\text{Gd}_{90}\text{Ce}_5\text{Tb}_5\text{BO}_3@ \text{SiO}_2$  particles and  $\text{Gd}_{90}\text{Ce}_5\text{Tb}_5\text{BO}_3@ \text{SiO}_2@ \text{CLX}$  as well as pure CLX alone for 24 h. An MTT assay (Vybrant® MTT Cell Proliferation Assay Kit, Invitrogen, Carlsbad, CA, USA) was performed according to the manufacturer's instructions. Absorbances were collected at 570 nm by a microplate reader (MultiSkan GO Microplate Spectrophotometer, Thermo Scientific, Waltham, MA, USA). The experiments were conducted as three biological and four technical replicates.

## CHAPTER 3

### CHARACTERIZATION

#### 3.1. Powder X-Ray diffraction (XRD)

Powder X-ray diffraction patterns were collected by using a Rigaku X-ray Diffractometer with a miniflex goniometer operated at 30 kV. As the X-ray source, 15 mA Cu-K $\alpha$  line ( $\alpha=1.54 \text{ \AA}$ ) was used. Continuous scanning mode was chosen and step size was adjusted to 0.01 degree, step rate was adjusted to 2.00 degree/min. The XRD patterns were collected starting from 5 degree to 90 degree. The samples are grinded in an Agate mortar until a homogeneous powder is formed. The powder is placed in the sample holder equally and analysis is done.

#### 3.2. Photoluminescence spectroscopy (PL)

Photoluminescence spectra of synthesized materials have been obtained by using a Varian Cary Eclipse Fluorescence Spectrometer. A solid sample holder was used to analyze powder samples. Excitation and emission slits had been adjusted to 2.5 mm. Scanning speed of PL record was set to 100 nm/min. For excitation, a filter with 240-395 nm band pass range was used and for emission, a filter with 430-1100 nm band pass range was used to prevent the detection of the scattered lights from the sample surface. The voltage of detector was set to default.

#### 3.3. CIE chromaticity diagram

Commission International de l'Eclairage (CIE) system was introduced in 1931 to determine the color of any light. The obtained wavelengths in a visible spectrum are converted to the real colors which are detectable by the human eye. CIE XYZ color space studies were done by William David Wriah and John Guild in late 1920s

(Wright, 1929 & Guild, 1932). XYZ values can be calculated by using the following formulas:

$$X = \int_{380}^{780} P(\lambda) \bar{x}(\lambda) d\lambda$$

$$Y = \int_{380}^{780} P(\lambda) \bar{y}(\lambda) d\lambda$$

$$Z = \int_{380}^{780} P(\lambda) \bar{z}(\lambda) d\lambda$$

Where  $\bar{x}(\lambda)$ ,  $\bar{y}(\lambda)$ , and  $\bar{z}(\lambda)$  are the spectral stimulus values which can be determined empirically. The values of the X, Y and Z are used to calculate  $x$  and  $y$  which are called chromaticity coordinates. Chromaticity coordinates can be calculated from the following equations:

$$x = \frac{X}{X+Y+Z}$$

$$y = \frac{Y}{X+Y+Z}$$

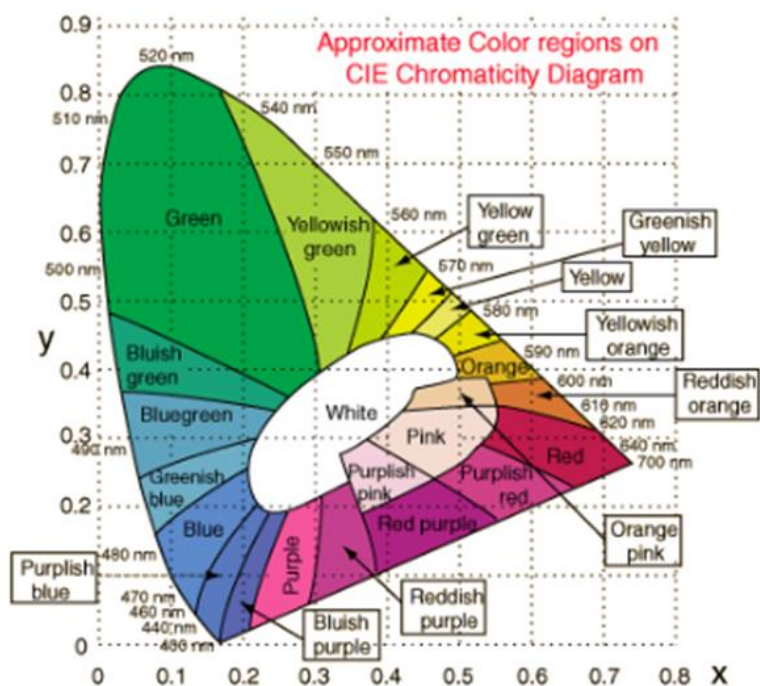


Figure 16. CIE chromaticity diagram (The C.I.E. Color Space, 2003).

### 3.4. Integrating sphere for measurements of fluorescence quantum yield

The integrating sphere is composed of PTFE like material with a reflectance value >99% with 120 mm inside diameter spherical cavity. The reflecting material is covered by an aluminum shell for protection. The integrating sphere has two perpendicularly placed ports, one with a lens to focus excitation beam into sample, the other is an open aperture which the emission or scatter can be monitored.

### 3.5. Transmission electron microscopy (TEM)

The mesoporous core/shell structure of the particles were monitored by a JEOL JEM 2100F STEM Transmission electron microscope at METU central laboratory. JEOL JEM 2100F Field emission gun was used. Before the analysis, samples were dispersed in ethanol and ultrasonicated for 30 minutes and operated at 120 kV. Samples were prepared by using 300-mesh carbon film coated copper grids.

### **3.6. Scanning electron microscopy (SEM)**

The particle morphology and shape were determined by Scanning electron microscope (SEM) at METU central laboratory. The instrument used for the analysis was QUANTA 400F Field Emission SEM. The analysis was done under high vacuum with (Everhart Thornley Detector) ETD secondary electron detector and a beam gun with 20 kV voltage. For analysis, samples were prepared onto double-sided tape which is composed of a mixture of copper and carbon.

### **3.7. Fourier transform infrared spectroscopy (FT-IR)**

In order to characterize the synthesized particles, Bruker IFS 66/S ATR spectrometer was used. The analysis was done in a range of 500 and 4000  $\text{cm}^{-1}$ . For the analysis, thin pellets were prepared by using 1 mg of sample and 100 mg of KBr.

### **3.8. Nitrogen-sorption**

Nitrogen adsorption-desorption measurements were done by Quantachrome Autosorb-6 at METU central laboratory. Drug loaded samples were outgassed at 50°C for 16 hours and core/shell particles were outgassed at 110°C for 16 hours. The pore size distribution was calculated according to the Barrett – Joyner – Halenda (BJH) isotherm and the specific surface area was calculated by using Brauner – Emmett – Teller (BET) method.

### **3.9. Thermogravimetric analysis (TGA)**

Thermogravimetric analysis was done by using a Pyris 1 Perkin Elmer Thermogravimetric Analyzer in air condition starting from 30°C to 600°C with a heating rate of 10°C/min.

### **3.10. Vibrating sample magnetometer (VSM)**

Magnetic properties of the samples were determined by a Vibrating-sample magnetometer, Cryogenic Limited PPMS at METU central laboratory. NbTi magnet

was used and the magnetic field range was from -5 Tesla to +5 Tesla. Analyses were done in 2 K, 20 K and 273 K.

### **3.11. Zeta-potential**

Zetasizer Nano-ZS (Malvern Instruments Ltd., U.K.) was used to determine zeta-potential of core/shell particles. Zeta-potential values were acquired via the Smoluchowski approximation from electrophoretic mobility data. For the analysis, 0.001 g of the samples are suspended in 50 mL deionized water and S 30 H ultrasonic bath was used for 30 minutes at 35°C.

### **3.12. Ultraviolet-visible spectroscopy (UV-VIS)**

Ultraviolet-visible analyses were done to determine the drug loading efficiency and release profile. CARY 5000 UV – VIS – NIR Spectrophotometer was used with a wavelength of 254 nm. Beer-Lambert law ( $A=\epsilon bc$ ) was used to calculate the amount of Celecoxib after loading and during the release. For the analysis, quartz tubes are used with a cell length of 10 mm.



## CHAPTER 4

### RESULTS & DISCUSSION

Luminescent and magnetic, silica coated  $\text{Ce}^{3+}$  and  $\text{Tb}^{3+}$  doped  $\text{GdBO}_3$  core/shell particles,  $\text{Gd}_{1-x-y}\text{Ce}_x\text{Tb}_y\text{BO}_3@\text{SiO}_2$ , were synthesized via following experimental procedure, Figure 17, and Celecoxib loading and release properties were investigated. For luminescence properties, Ce and Tb was chosen as the dopants and for magnetic properties  $\text{GdBO}_3$  was chosen as the host material. Mesoporous silica was chosen as the shell material because of its easy synthesis route, inertness, transparency, surface chemistry and biocompatibility. For the characterization of these materials, X-Ray diffraction (XRD), photoluminescence spectroscopy (PL),  $\text{N}_2$  adsorption-desorption, transmission electron microscopy (TEM), scanning electron microscopy (SEM), Fourier-transform infra-red spectroscopy (FT-IR), thermogravimetric analysis (TGA), vibrating-sample magnetometer (VSM) analysis and zeta-potential analysis. For quantum yield calculations fluorescence spectroscopy with integrating sphere was used. For drug loading efficiency and drug release properties ultraviolet-visible spectrometry (UV-VIS) was used.

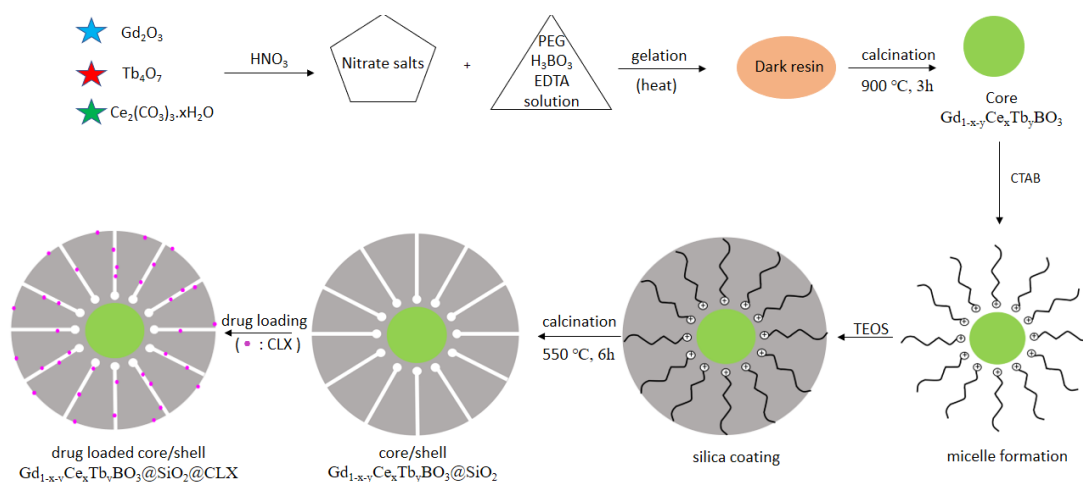


Figure 17. Experimental scheme for core, core/shell synthesis and drug loading (PEG: polyethylene glycol, EDTA: ethylenediaminetetraacetic acid, CTAB: cetyltrimethylammonium bromide, TEOS: tetraethylorthosilicate, CLX: celecoxib).

#### 4.1. Powder X-Ray diffraction pattern of core, core/shell and drug loaded core/shell particles

In order to characterize and compare the crystal structure of the synthesized materials, XRD analysis was used. Gadolinium borate has a hexagonal structure with dimensions of  $a=3.8290 \text{ \AA}$ ,  $b=3.8290 \text{ \AA}$ ,  $c=8.8900 \text{ \AA}$  and  $\alpha=90.000^\circ$ ,  $\beta=90.000^\circ$ ,  $\gamma=95.95^\circ$  crystal lattice parameters (JCPDS card No: 13-0483). Figure 18 shows the XRD pattern of  $\text{Ce}^{3+}$  and  $\text{Tb}^{3+}$  doped  $\text{GdBO}_3$  particles which were synthesized by using EDTA and citric acid separately. As obviously can be seen from the XRD pattern, diffraction peaks of particles synthesized by using EDTA harmonise with the pattern of hexagonal  $\text{GdBO}_3$  (JCPDS card No: 13-0483). However, particles synthesized with citric acid have some extra diffraction peaks in  $\text{GdBO}_3$  pattern. The identification of those extra peaks was done with the XRD instrument's peak search library and it is found that those extra peaks belong to  $\text{Gd}(\text{BO}_2)_3$ , Gadolinium triborate (JCPDS card No: 70-2239), Figure 18. Since citric acid lowers the pH of the sol-gel media, there is a high possibility of formation of triborates instead of borates. In order to be sure about the reason for the formation of triborates, higher doping concentrations of Ce and Tb samples were analyzed.

Figure 19 shows the  $\text{GdBO}_3$  patterns with different concentrations of Ce and Tb. Again, higher doping concentrations have a pure XRD pattern when synthesized with EDTA, but there are still triborate peaks for citric acid synthesis. Therefore, it can be said that the formation of pure  $\text{GdBO}_3$  is not affected by the concentration of  $\text{Ce}^{3+}$  and  $\text{Tb}^{3+}$ . In conclusion,  $\text{Ce}^{3+}$  and  $\text{Tb}^{3+}$  can form substitutional or/ and interstitial alloy with  $\text{GdBO}_3$  host matrix when synthesized by using EDTA as the chelating agent.

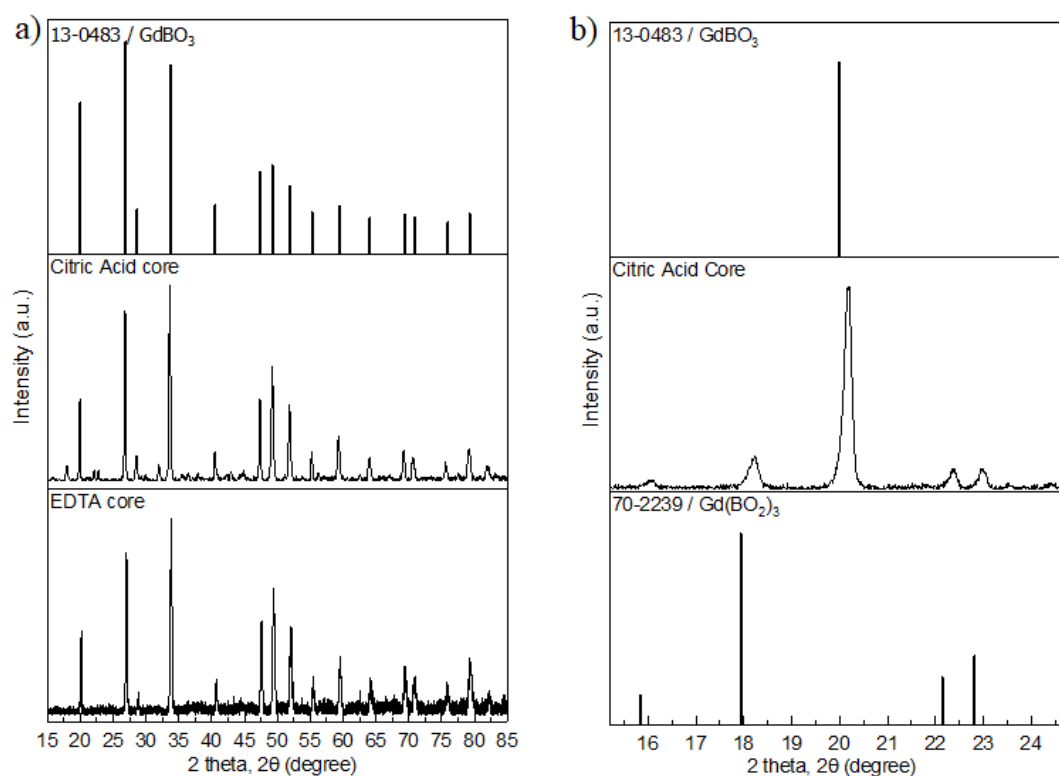


Figure 18. (a) XRD patterns of  $\text{Gd}_{0.90}\text{Ce}_{0.05}\text{Tb}_{0.05}\text{BO}_3$  synthesized with citric acid and EDTA,  $\text{GdBO}_3$  card, 13-0483 (b) XRD pattern of citric acid synthesis,  $\text{GdBO}_3$  card and  $\text{Gd}(\text{BO}_2)_3$  card, 70-2239.

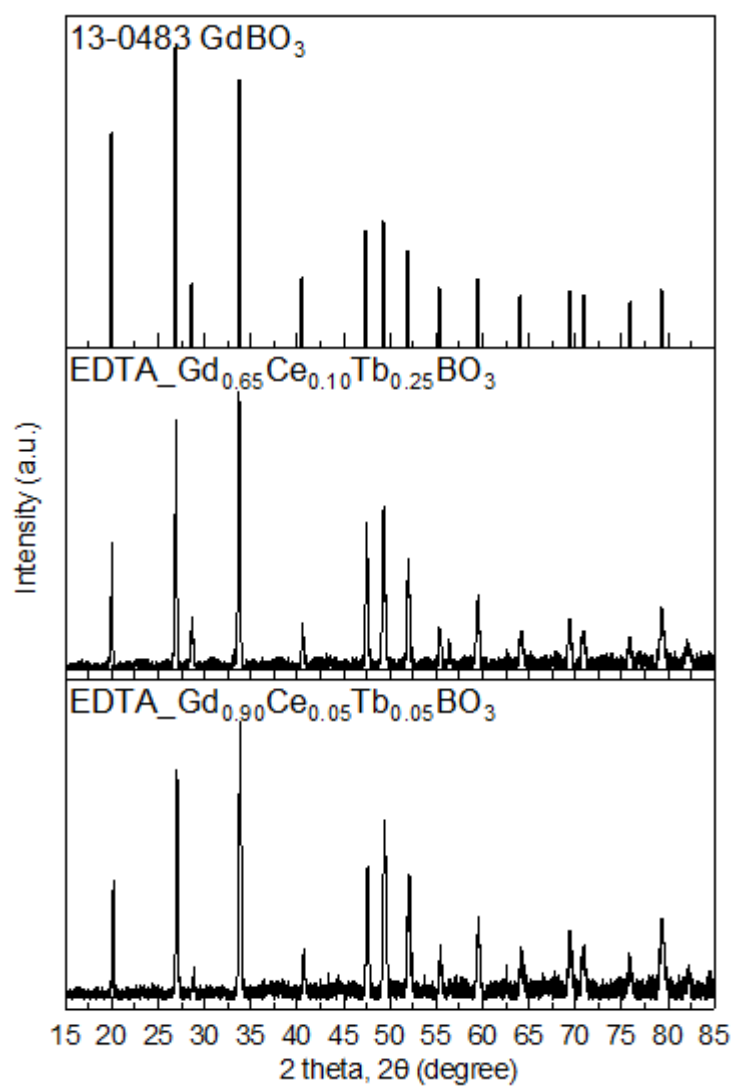


Figure 19. XRD patterns of Gd<sub>0.65</sub>Ce<sub>0.10</sub>Tb<sub>0.25</sub>BO<sub>3</sub> and Gd<sub>0.90</sub>Ce<sub>0.05</sub>Tb<sub>0.05</sub>BO<sub>3</sub> core which were synthesized by using EDTA.

XRD patterns after silica coating and drug loading can be seen in Figure 20. After silica coating and Celecoxib loading processes, it is observed that the crystal structure of GdBO<sub>3</sub> is conserved.

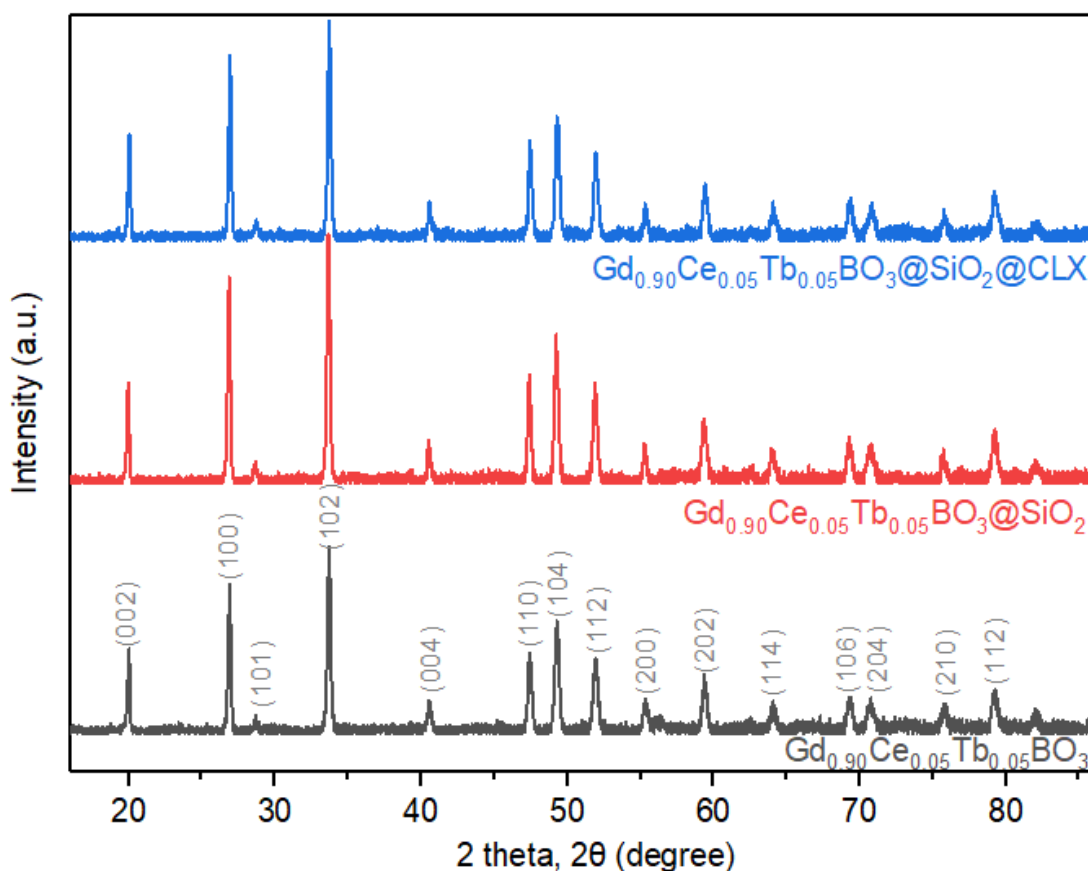


Figure 20. XRD patterns of core, core/shell and drug loaded samples.

#### 4.2. Photoluminescence spectra of core, core/shell and drug loaded core/shell particles

Photoluminescence emission measurements were done for  $\text{Ce}^{3+}$  and  $\text{Tb}^{3+}$  doped  $\text{GdBO}_3$  core particles, core/shell particles before and after drug loading. Photoluminescence spectra were collected in 400-650 nm range at room temperature and excitation wavelength is 359 nm. All core, core/shell and Celecoxib loaded core/shell materials show a strong green luminescence. Figure 21 shows the PL excitation spectrum of  $\text{Ce}^{3+}$  and  $\text{Tb}^{3+}$  doped  $\text{GdBO}_3$  obtained with an emission wavelength of 545 nm. A broad and intense excitation peak was observed at 359 nm and for further analyses, the excitation wavelength of 359 nm was adjusted to collect

the emission spectra. From the literature, it is known that  $Tb^{3+}$  ion has 4 peaks located at 490, 545, 585 and 622 nm arising from the  $^5D_4 \rightarrow ^7F_5$ ,  $^5D_4 \rightarrow ^7F_8$ ,  $^5D_4 \rightarrow ^7F_4$  and  $^5D_4 \rightarrow ^7F_3$  transitions respectively (Selvin & Hearst, 2006).

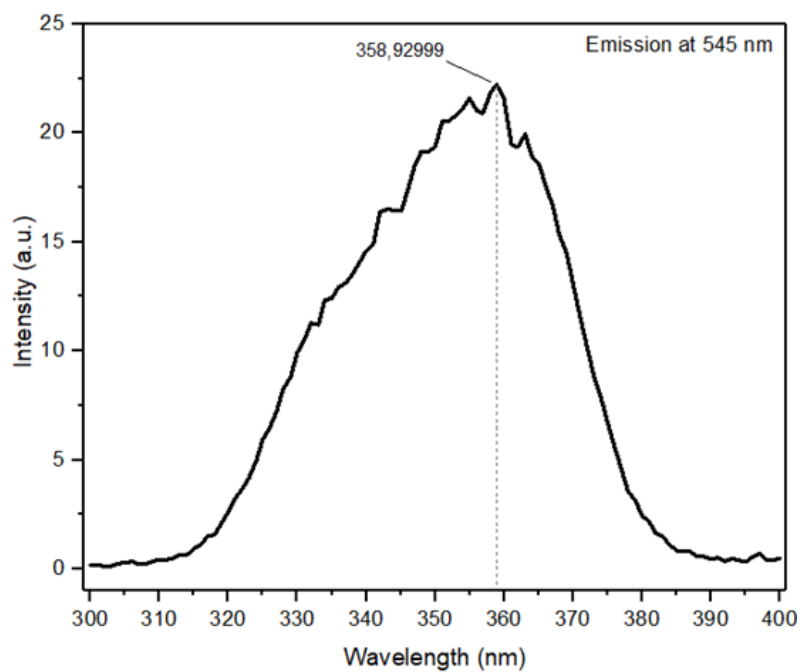


Figure 21. Photoluminescence excitation spectra of  $Gd_{0.90}Ce_{0.05}Tb_{0.05}BO_3$  at 545 nm wavelength.

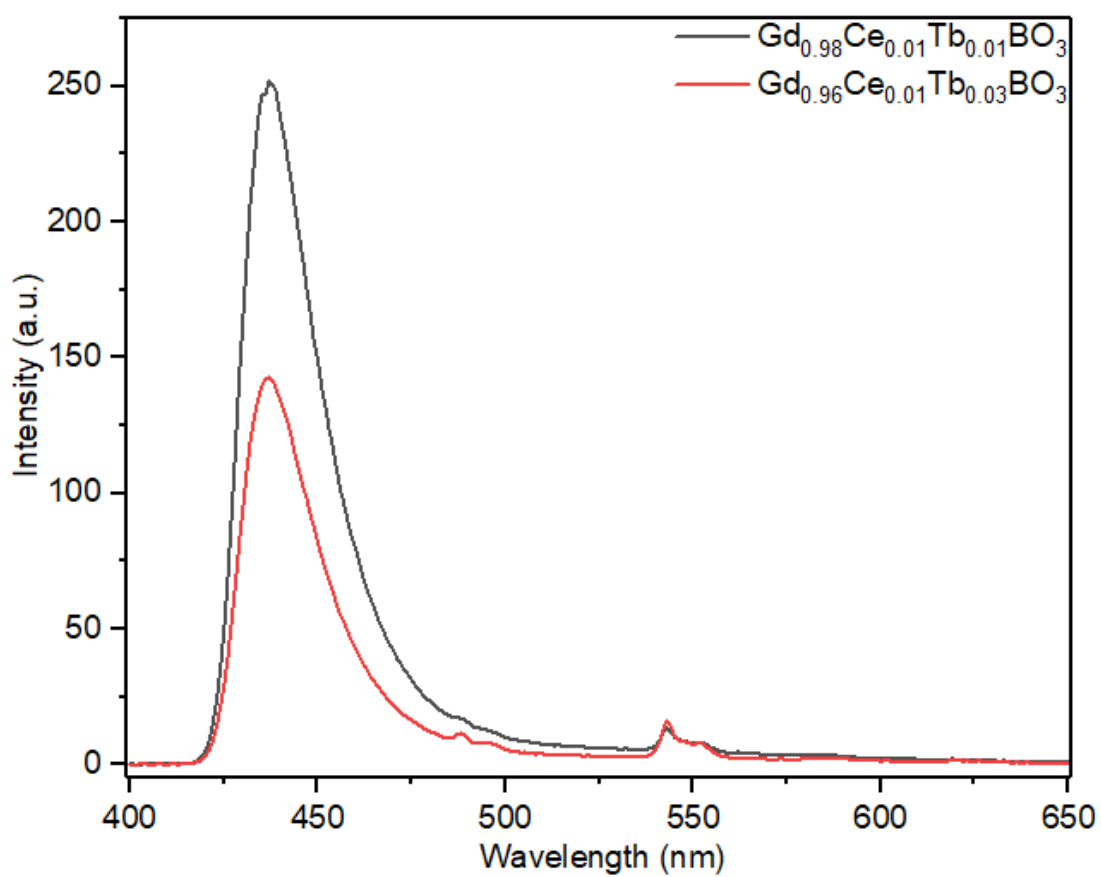


Figure 22. Photoluminescence emission spectra of  $\text{Gd}_{0.98}\text{Ce}_{0.01}\text{Tb}_{0.01}\text{BO}_3$  and  $\text{Gd}_{0.96}\text{Ce}_{0.01}\text{Tb}_{0.03}\text{BO}_3$  at an excitation wavelength of 359 nm.

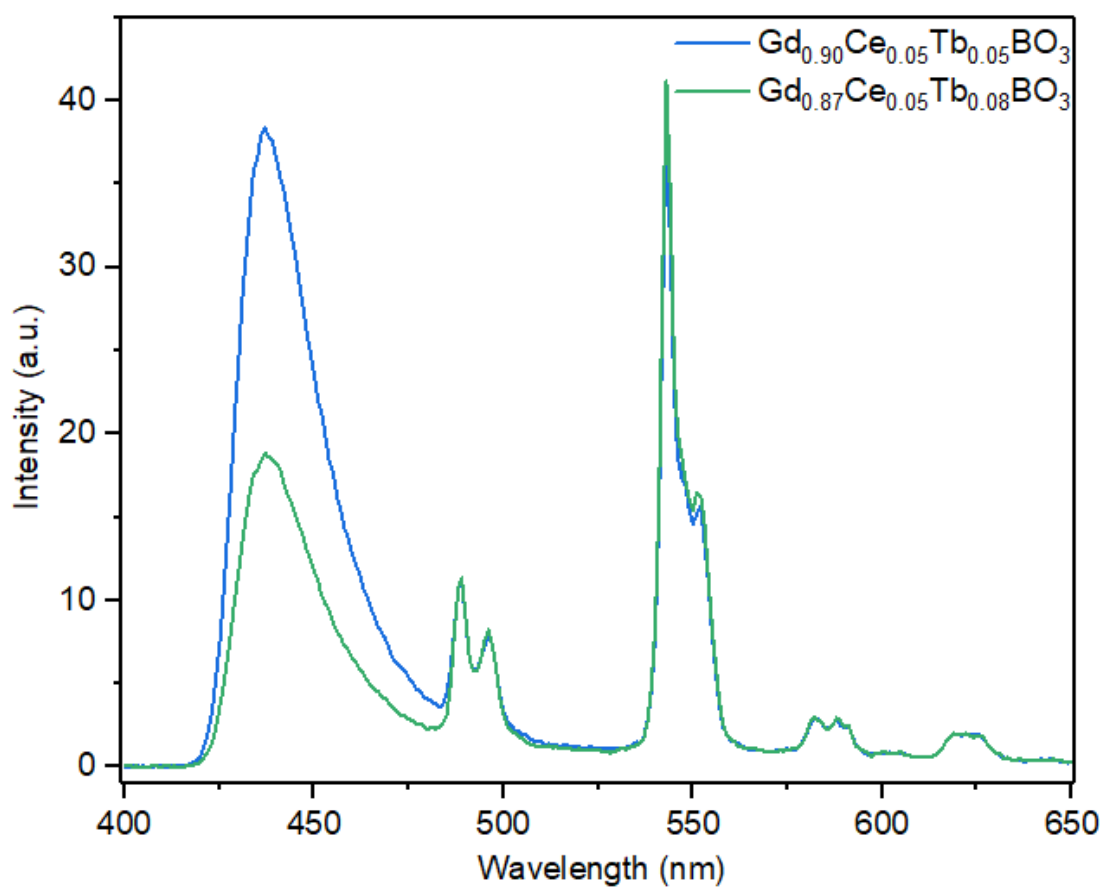


Figure 23. Photoluminescence emission spectra of  $\text{Gd}_{0.90}\text{Ce}_{0.05}\text{Tb}_{0.05}\text{BO}_3$  and  $\text{Gd}_{0.87}\text{Ce}_{0.05}\text{Tb}_{0.08}\text{BO}_3$  at an excitation wavelength of 359 nm.

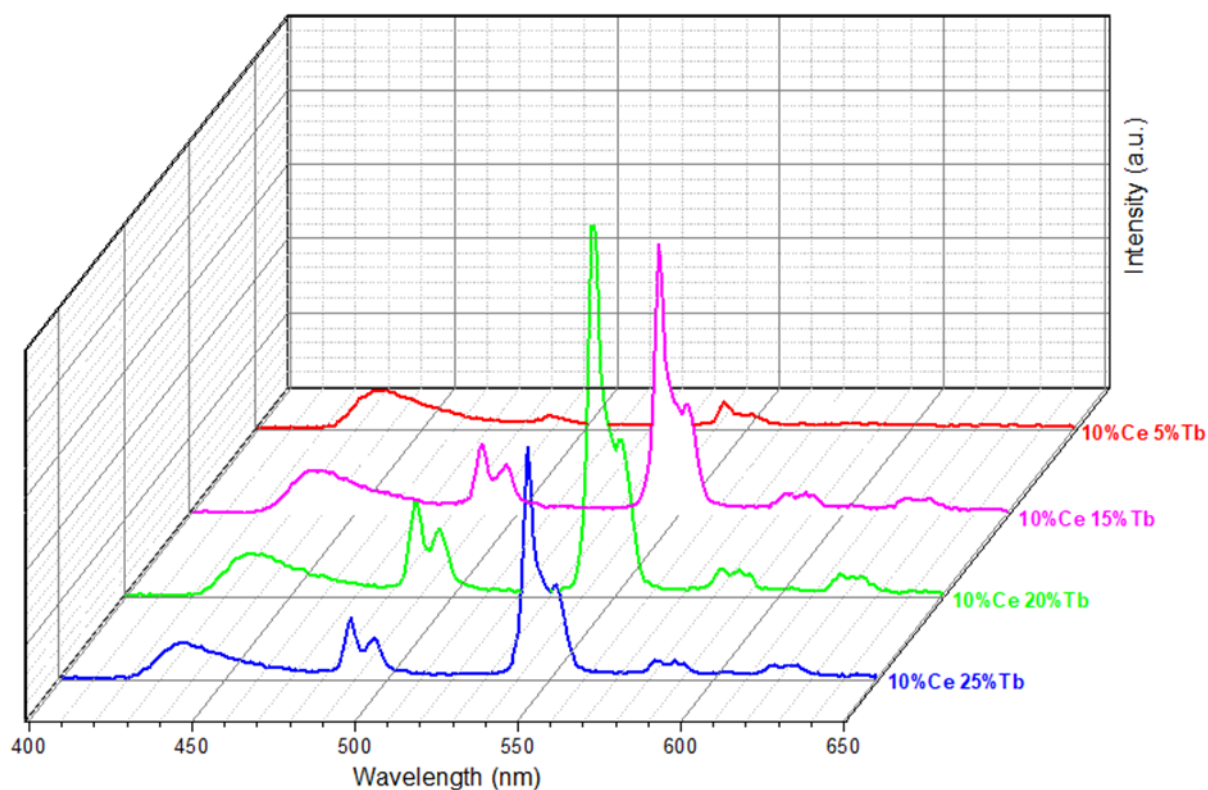


Figure 24. Photoluminescence emission spectra of  $\text{Gd}_{0.85}\text{Ce}_{0.10}\text{Tb}_{0.05}\text{BO}_3$ ,  $\text{Gd}_{0.75}\text{Ce}_{0.10}\text{Tb}_{0.15}\text{BO}_3$ ,  $\text{Gd}_{0.70}\text{Ce}_{0.10}\text{Tb}_{0.20}\text{BO}_3$  and  $\text{Gd}_{0.65}\text{Ce}_{0.10}\text{Tb}_{0.25}\text{BO}_3$  at an excitation wavelength of 359 nm.

In Figure 22, PL spectra of 1% Ce doped samples were compared. There is a certain  $\text{Ce}^{3+}$  peak centered at 437 nm associated with  $5d \rightarrow 4f$  transition of  $\text{Ce}^{3+}$  ions for both samples, however  $\text{Tb}^{3+}$  peaks are not observed intensely, in fact, there is only one peak belonging to  $\text{Tb}^{3+}$  ion which is located at 545 nm. In order to observe all the  $\text{Tb}^{3+}$  peaks intensely and sharply, different concentrations of  $\text{Ce}^{3+}$  and  $\text{Tb}^{3+}$  samples were prepared and analyzed. In Figure 23 and 24, PL spectra of 5% Ce and 10% Ce doped samples were illustrated, respectively.

In both 5% Ce and 10% Ce samples, both  $\text{Tb}^{3+}$  peaks and  $\text{Ce}^{3+}$  peak can be observed (Figure 24). However, when the most intense peaks were compared, it can be seen that 5% Ce, 5% Tb doped samples has the highest photoluminescence intensity among all the samples (Figure 25).

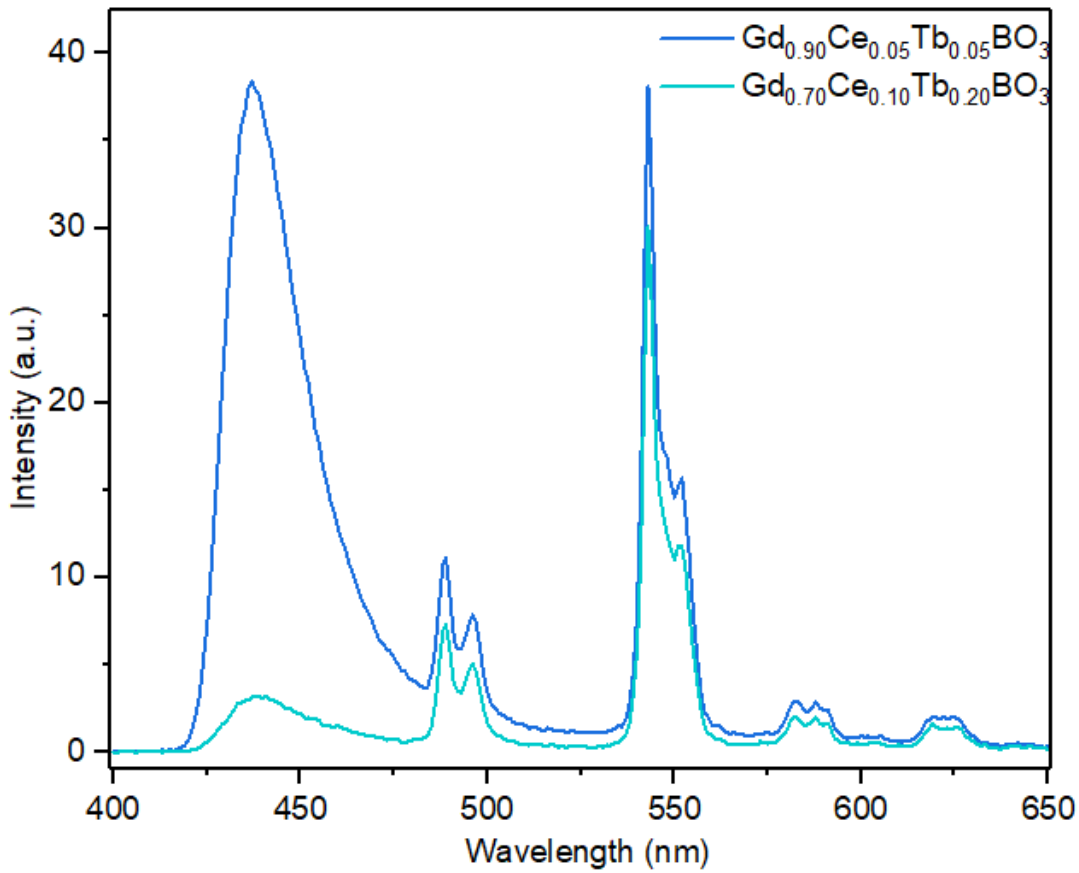


Figure 25. Photoluminescence emission spectra of  $\text{Gd}_{0.70}\text{Ce}_{0.10}\text{Tb}_{0.20}\text{BO}_3$  and  $\text{Gd}_{0.90}\text{Ce}_{0.05}\text{Tb}_{0.05}\text{BO}_3$  at an excitation wavelength of 359 nm.

The emission spectrum collected between 450-650 nm for 5% Ce samples has four bands centered at 490, 545, 585 and 622 nm (Figure 26). The most intense peak at 545 nm belongs to the  $^5\text{D}_4 \rightarrow ^7\text{F}_5$  transition. The following peaks located at 490 nm, 585 nm and 622 nm belong to  $^5\text{D}_4 \rightarrow ^7\text{F}_8$ ,  $^5\text{D}_4 \rightarrow ^7\text{F}_4$  and  $^5\text{D}_4 \rightarrow ^7\text{F}_3$  transitions respectively. In conclusion, all the  $5d-4f$  transitions of  $\text{Tb}^{3+}$  can be seen in the emission spectra of  $\text{Gd}_{0.90}\text{Ce}_{0.05}\text{Tb}_{0.05}\text{BO}_3$ .

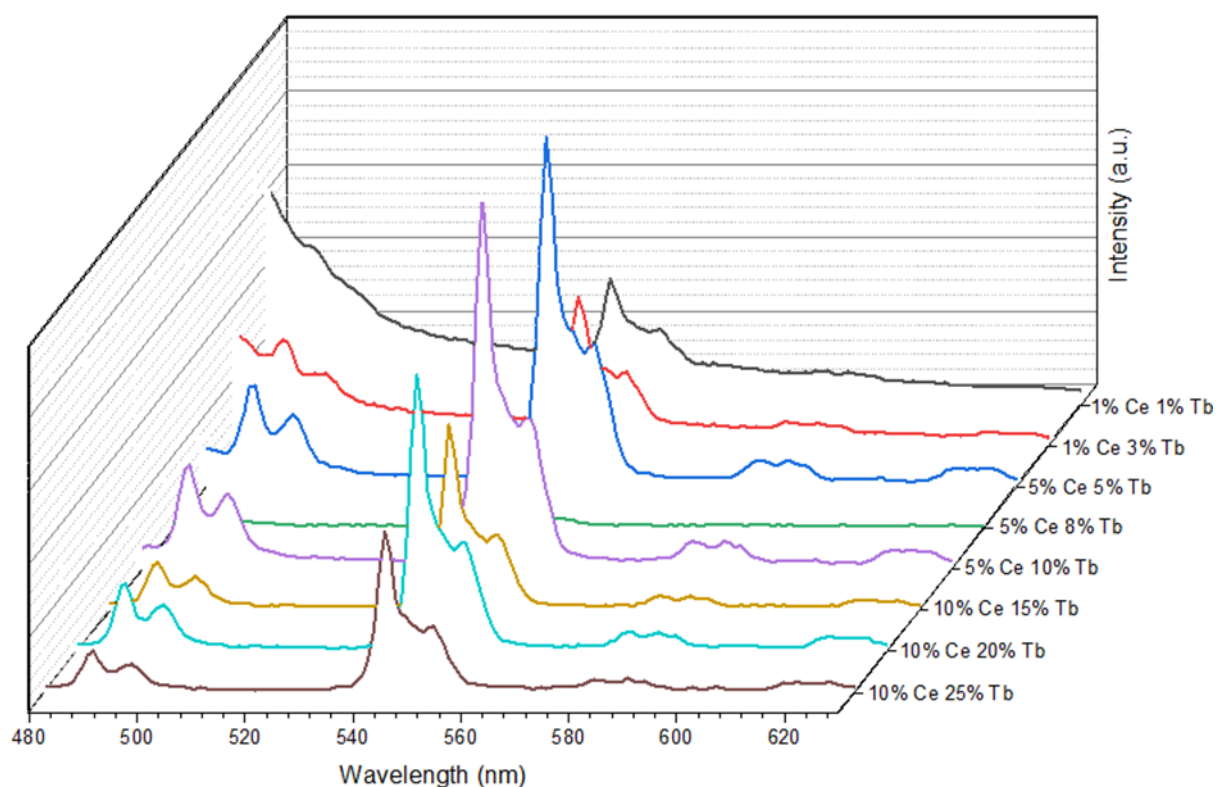


Figure 26. Photoluminescence emission spectra of  $Gd_{1-x-y}Ce_xTb_yBO_3$  with different concentrations of Ce and Tb at an excitation wavelength of 359 nm.

To conclude, the emission intensities of  $Gd_{1-x-y}Ce_xTb_yBO_3$  materials with different  $Ce^{3+}$  and  $Tb^{3+}$  concentrations show varying peak intensities. From the Figure 26, it can be understood that the amount of dopants play a very important role to reach the highest luminescence intensity. As can be seen from the figure, 5% Ce and 5% Tb doped  $GdBO_3$  has the highest luminescence intensity among all.

In Figure 27, there is a comparison between PL spectra of single  $Tb^{3+}$  doped  $GdBO_3$  and  $Ce^{3+}$  and  $Tb^{3+}$  co-doped  $GdBO_3$ . There is a huge difference between these two materials, that is, co-doped material has very intense  $Ce^{3+}$  and  $Tb^{3+}$  peaks where single  $Tb^{3+}$  doped material does not have any. From this figure it can be inferred that  $Ce^{3+}$  ion is an excellent sensitizer for  $Tb^{3+}$  ion in  $GdBO_3$  host structure.

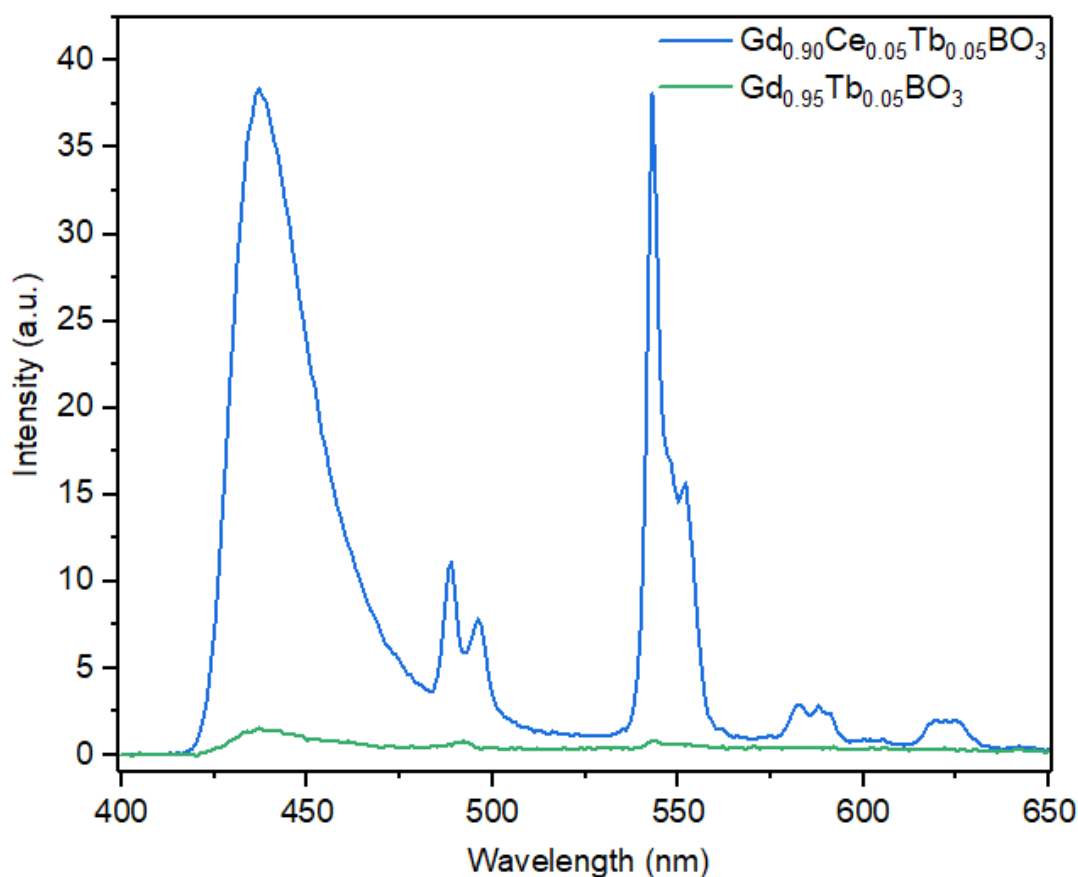


Figure 27. Photoluminescence emission spectra of  $Gd_{0.90}Ce_{0.05}Tb_{0.05}BO_3$  and  $Gd_{0.95}Tb_{0.05}BO_3$ , at an excitation wavelength of 359 nm.

In Figure 28, the PL emission spectra of core, core/shell and Celecoxib loaded drug carrier can be seen. In every step, there is a decrease in peak intensity for both silica coating and drug loading procedures. Actually, this figure has given us the idea about the quantification of the drug from the PL intensity. In literature, there are some examples to this situation. For example, Yang and his/her friends have successfully synthesized a double silica coated,  $Eu^{3+}$  doped  $YVO_4$  luminescent drug carrier with increasing luminescence intensity during Ibuprofen drug release (Yang et al., 2009).

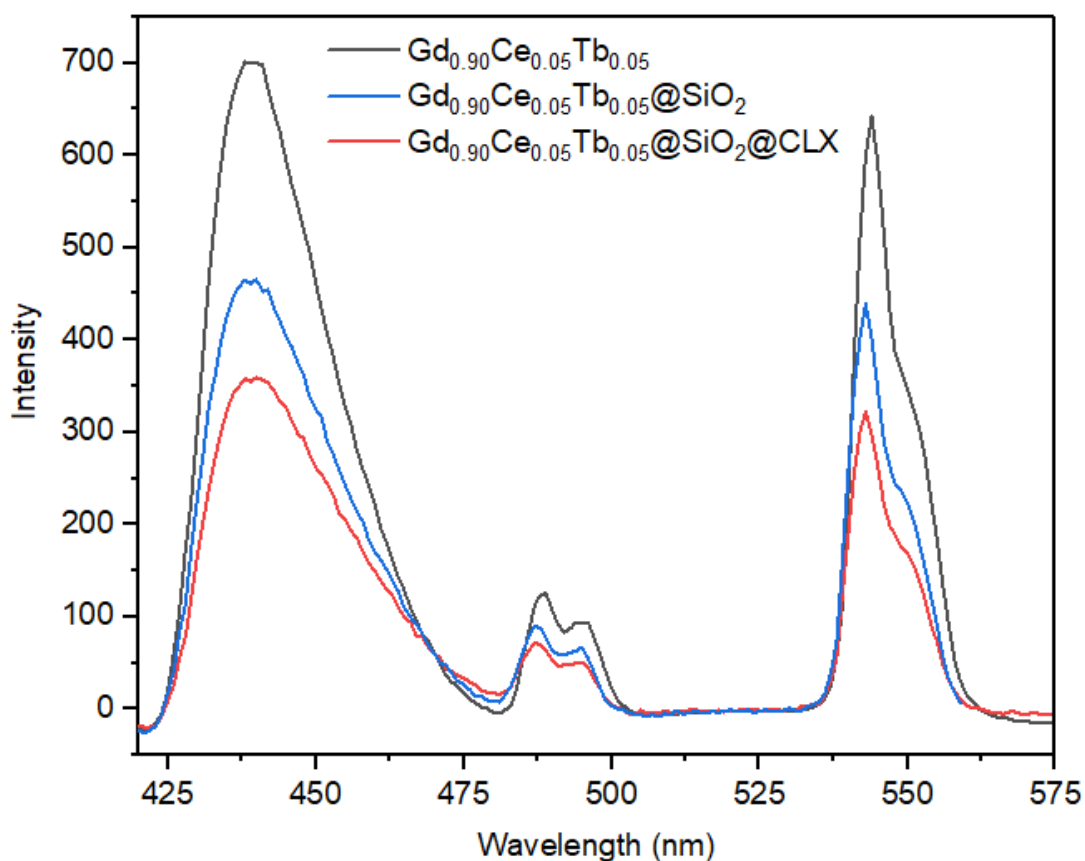


Figure 28. Photoluminescence emission spectra of  $Gd_{0.90}Ce_{0.05}Tb_{0.05}BO_3$  core,  $SiO_2$  coated core and drug loaded core/shell samples at an excitation wavelength of 359 nm.

In order to observe the PL spectra after drug release, drug carrier was separated from the release media by centrifugation. The remaining solid was dried and PL analysis was done. In Figure 29, there are the PL emission intensities of the drug carrier after 30 minutes, 2 hours, 4 hours and 6 hours. There is a certain proportional increase in PL intensities. This means that the quantification of Celecoxib in the body may be done by peak intensity in the future. Figure 30 shows the PL intensity change depending on the Celecoxib release time.

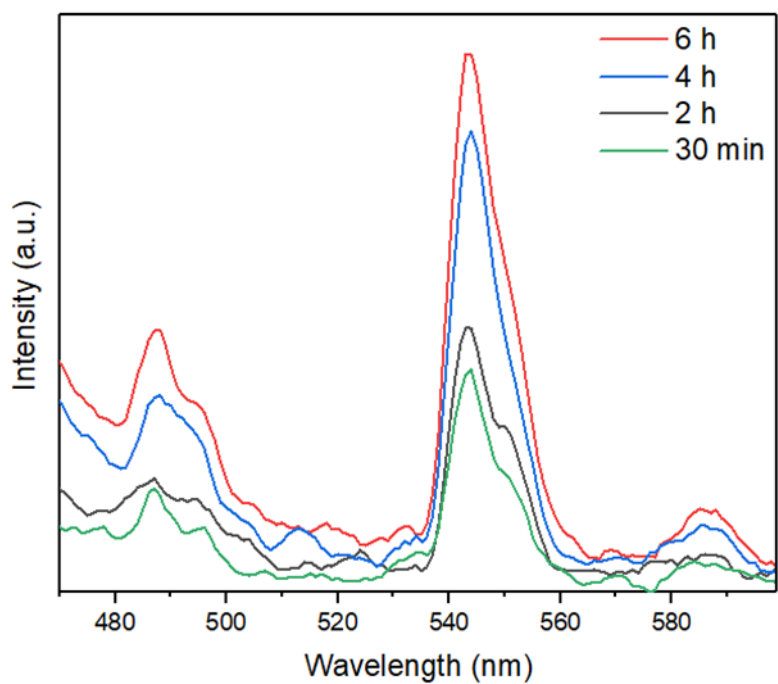


Figure 29. Photoluminescence emission spectra of Celecoxib loaded samples after 30 minutes, 2 hours, 4 hours and 6 hours of drug release in PBS at an excitation wavelength of 359 nm.

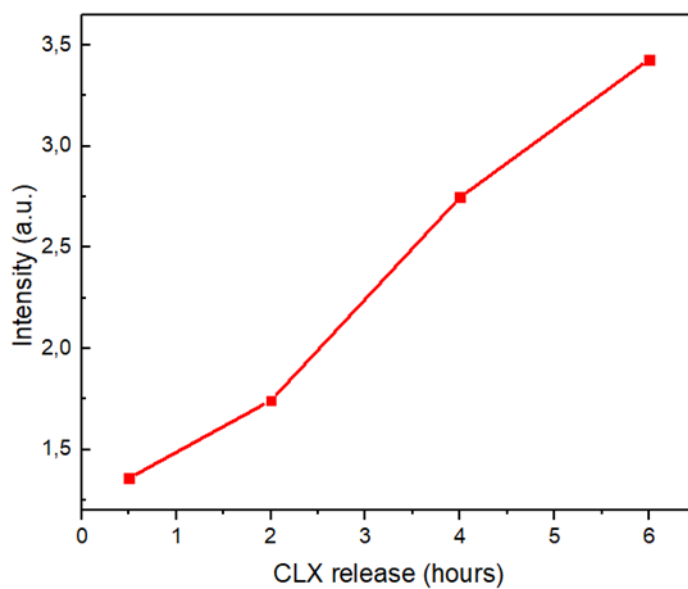


Figure 30. Photoluminescence intensity as a function of the cumulatively released CLX.

### 4.3. CIE chromaticity diagram

CIE chromaticity coordinates of  $\text{Gd}_{0.90}\text{Ce}_{0.05}\text{Tb}_{0.05}\text{BO}_3$  was calculated by using Matlab (Matric Laboratory). The color of the sample was determined by a specific calculation using integrated peak's area obtained from PL emission spectrum of the material. The color of the samples is bright green with x and y values of 0.31 and 0.57, respectively (Figure 31).

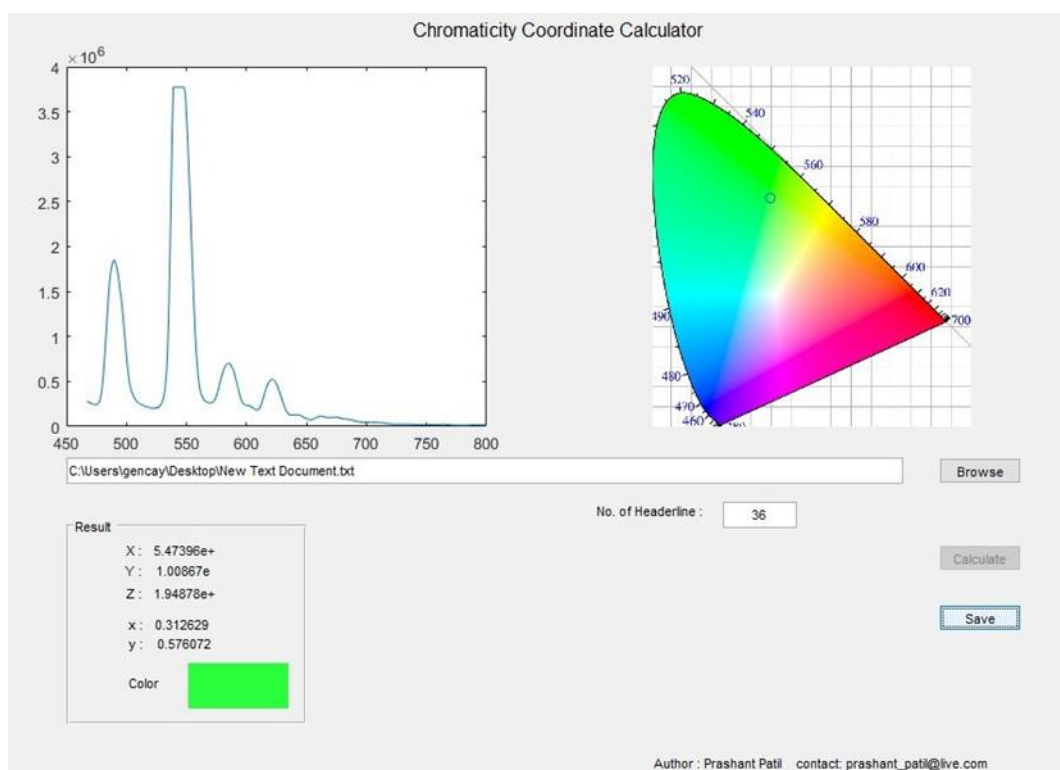


Figure 31. CIE chromaticity diagram for  $\text{Gd}_{0.90}\text{Ce}_{0.05}\text{Tb}_{0.05}\text{BO}_3$ .



*Figure 32.* Image of  $\text{Gd}_{0.90}\text{Ce}_{0.05}\text{Tb}_{0.05}\text{BO}_3$  samples both in water-dispersed and solid forms under UV lamp, 366 nm.

The image displayed in Figure 32 belongs to  $\text{Gd}_{0.90}\text{Ce}_{0.05}\text{Tb}_{0.05}\text{BO}_3$  sample and this image was collected under UV lamp with a wavelength of 366 nm. To summarize, the image under the UV-lamp and the CIE chromaticity results are consistent.

#### **4.4. Integrating sphere measurements of fluorescence quantum yield**

Quantum yield of the  $\text{Gd}_{0.90}\text{Ce}_{0.05}\text{Tb}_{0.05}\text{BO}_3$  samples was calculated according to the following PL spectrum (Figure 33). The average quantum yield of the sample was calculated as  $42 \pm 5$  % which means that  $\text{Gd}_{0.90}\text{Ce}_{0.05}\text{Tb}_{0.05}\text{BO}_3$  may be used as a fluorescent labeling agent or bio-sensor (Matea et al., 2017).

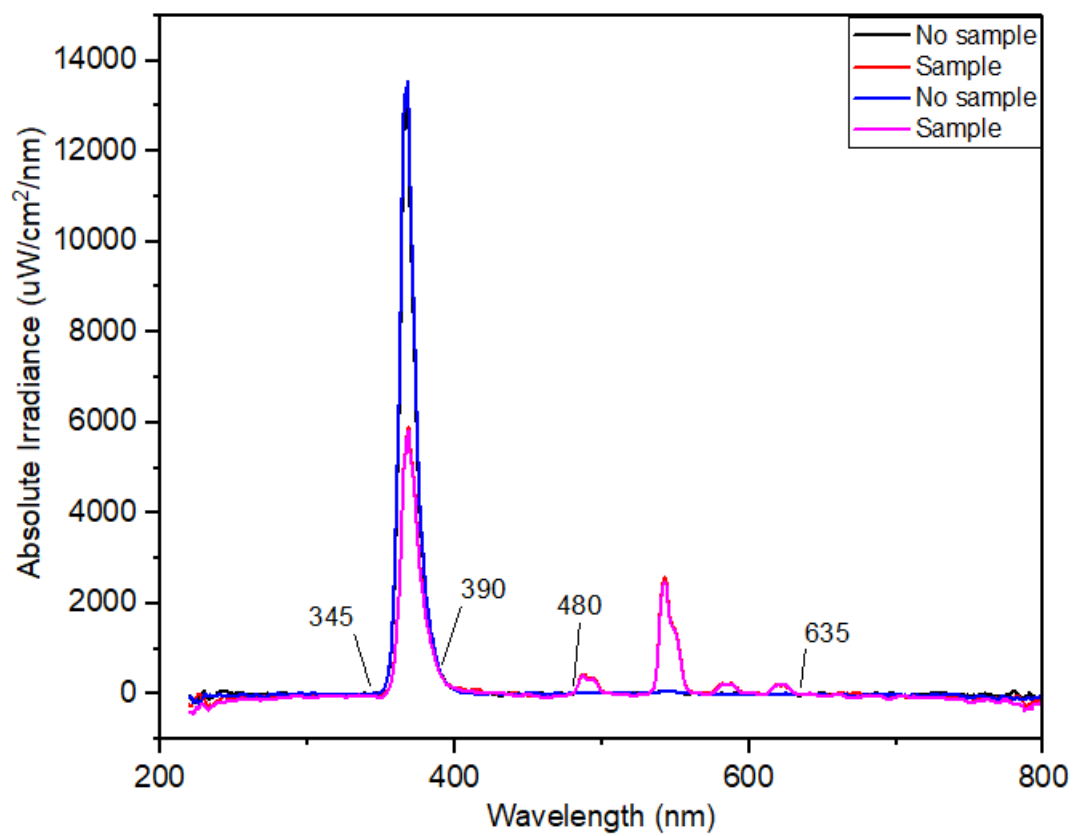


Figure 33. Photoluminescence spectra of  $Gd_{0.90}Ce_{0.05}Tb_{0.05}BO_3$ .

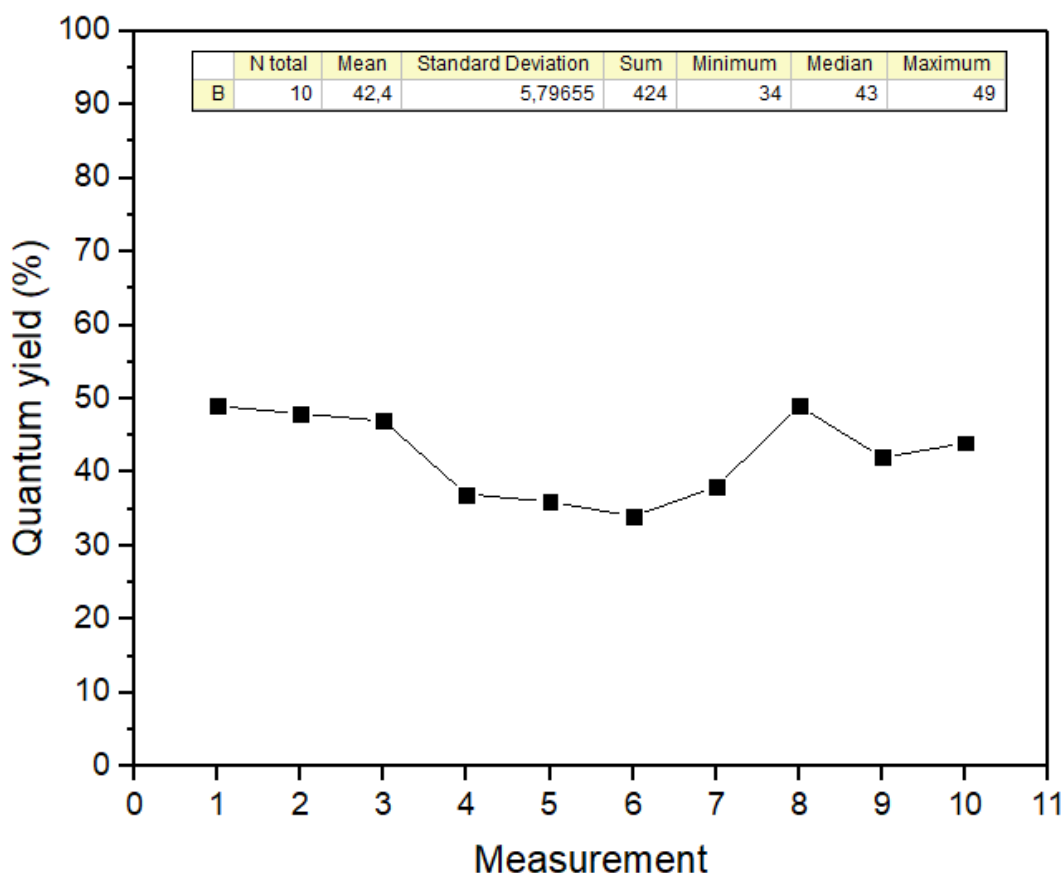


Figure 34. Average quantum yield of  $Gd_{0.90}Ce_{0.05}Tb_{0.05}BO_3$ .

#### 4.5. Transmission electron microscopy (TEM)

Transmission electron microscopy images of core and core/shell products can be seen in the following figures. For a better understanding of mesoporous structure of silica shell, TEM analysis was done before and after silica coating. TEM images of  $Gd_{0.90}Ce_{0.05}Tb_{0.05}BO_3$  core can be seen in Figure 35, from Figure 35a, it can be seen that the core has a size about 60 nm but in Figure 35b agglomeration of the particles can be seen. In Figure 36, single-silica coated particles can be seen. There is no uniformity for these particles and also there are self-assembles silica particles. Therefore, double silica coating was applied to obtain core/shell type materials.

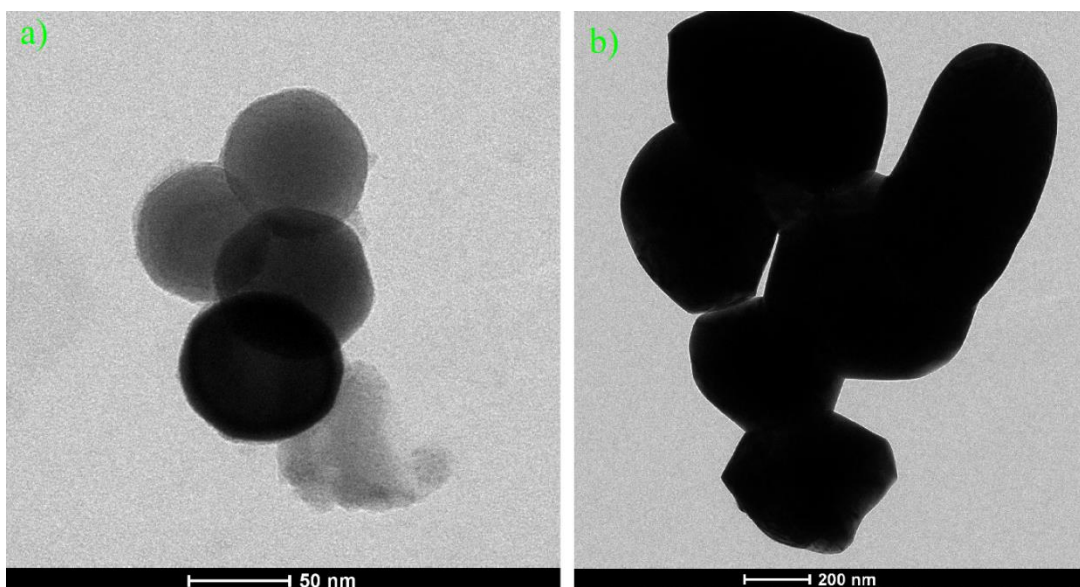


Figure 35. (a) TEM image of  $\text{Gd}_{0.90}\text{Ce}_{0.05}\text{Tb}_{0.05}\text{BO}_3$  core samples synthesized with EDTA, (b) TEM image of  $\text{Gd}_{0.90}\text{Ce}_{0.05}\text{Tb}_{0.05}\text{BO}_3$  core samples synthesized with citric acid.

In Figure 37, spherical core/shell type particles can be seen with a size of 200 nm and there is a narrow size distribution. By double-silica coating, it can be concluded that more ordered particles were obtained. Also, silica channels and porosity of the material can be seen in Figure 38.

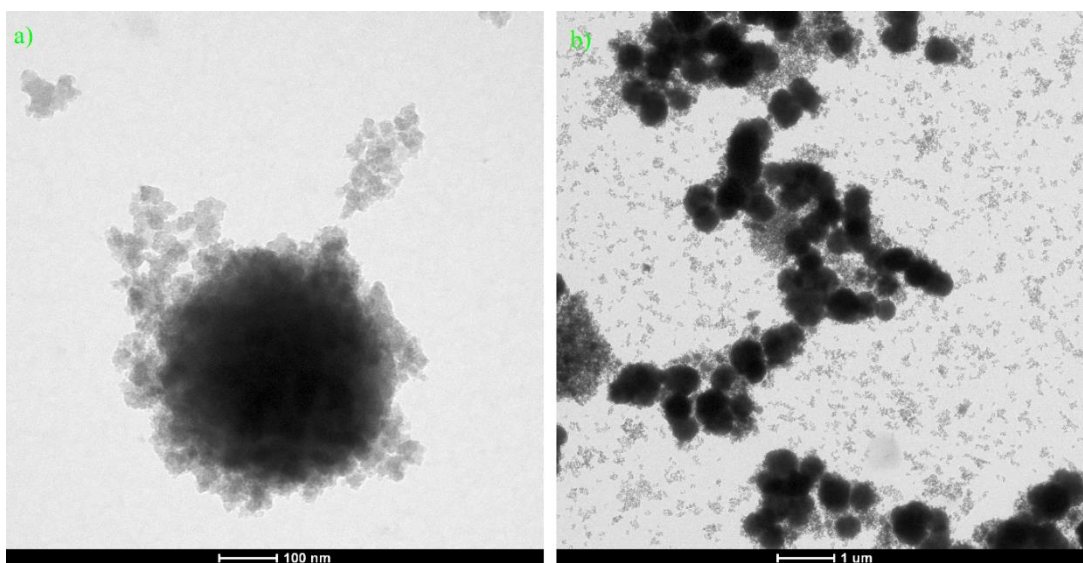


Figure 36. TEM images of single silica-coated  $\text{Gd}_{0.90}\text{Ce}_{0.05}\text{Tb}_{0.05}\text{BO}_3$  core samples.

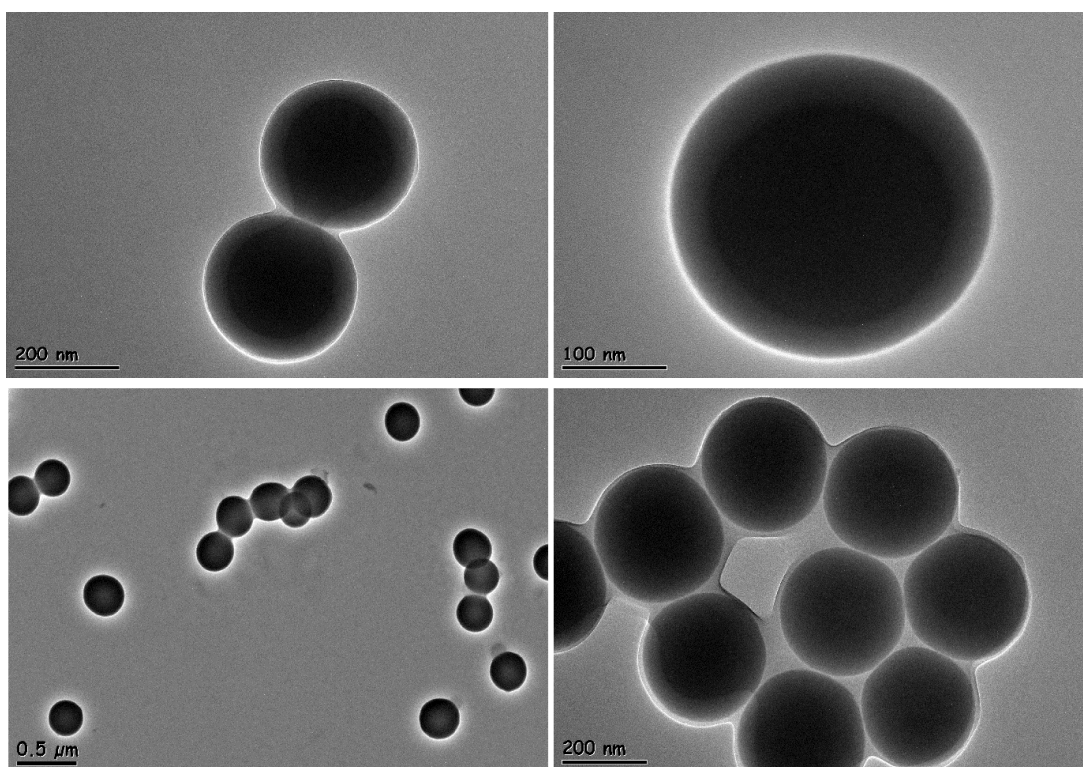
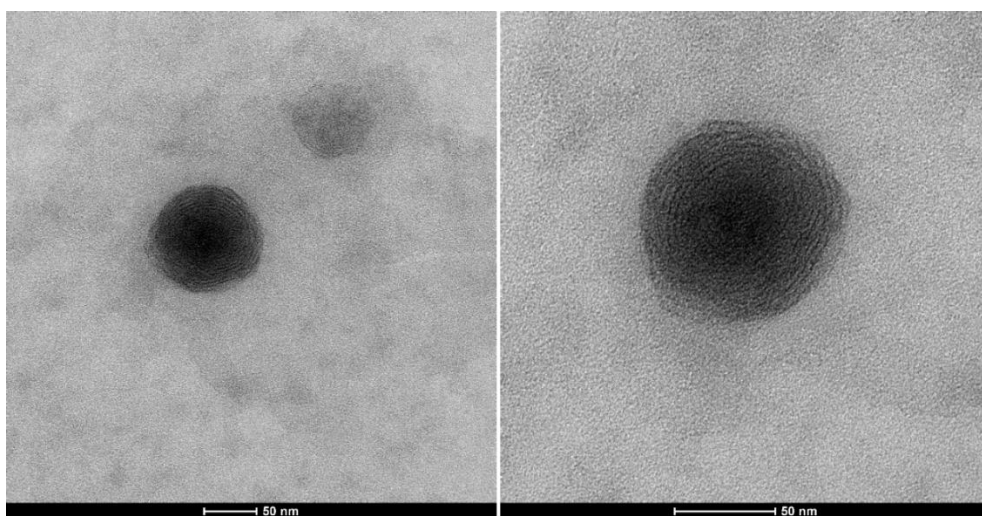


Figure 37. TEM images of double silica-coated  $\text{Gd}_{0.90}\text{Ce}_{0.05}\text{Tb}_{0.05}\text{BO}_3$  core samples.



*Figure 38.* TEM images of double silica-coated  $\text{Gd}_{0.90}\text{Ce}_{0.05}\text{Tb}_{0.05}\text{BO}_3$  core samples.

#### **4.6. Scanning electron microscopy (SEM)**

Morphology of the core and core/shell particles were monitored by Scanning Electron Microscope. In Figure 39, there are core particles synthesized by using citric acid and EDTA separately. In both synthesis, there are no uniformity and agglomeration of the particles can be seen. However in EDTA synthesis, the agglomeration is less than citric acid synthesis and particles are smaller.

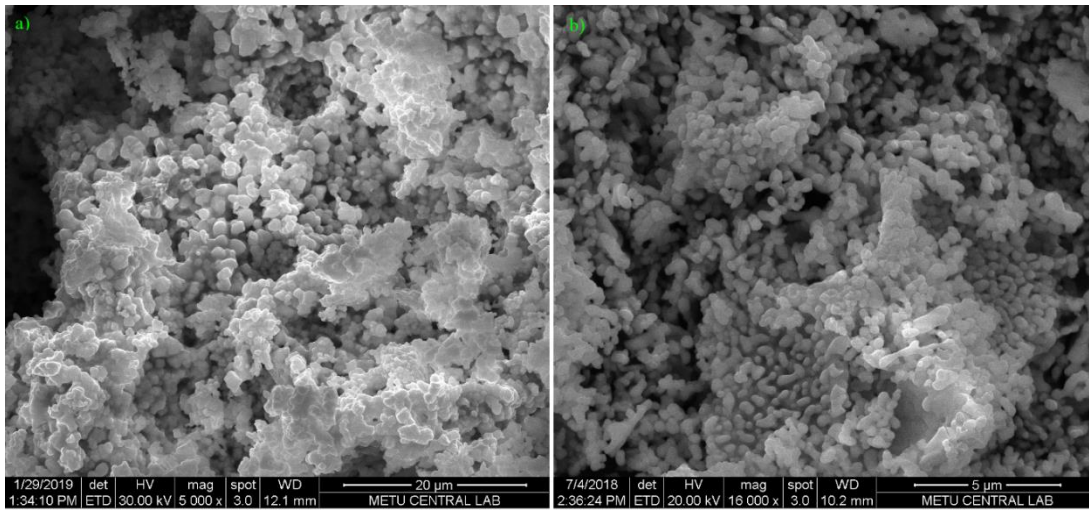


Figure 39. (a) SEM images of  $Gd_{0.90}Ce_{0.05}Tb_{0.05}BO_3$  core samples synthesized with citric acid and (b) core samples synthesized with EDTA.

After silica coating the particle size and distribution seems better since silica coating includes long ultrasonication steps, these steps may have separated the agglomerated particles and following images were collected for single and double silica coated samples. In Figure 40, it can be seen that single silica coating makes the particles much smaller than double coating. However, particle size distribution of double coated samples is narrower than single coated samples and also particle morphology is spherical for double coated samples where single coated samples have a mixed morphology.

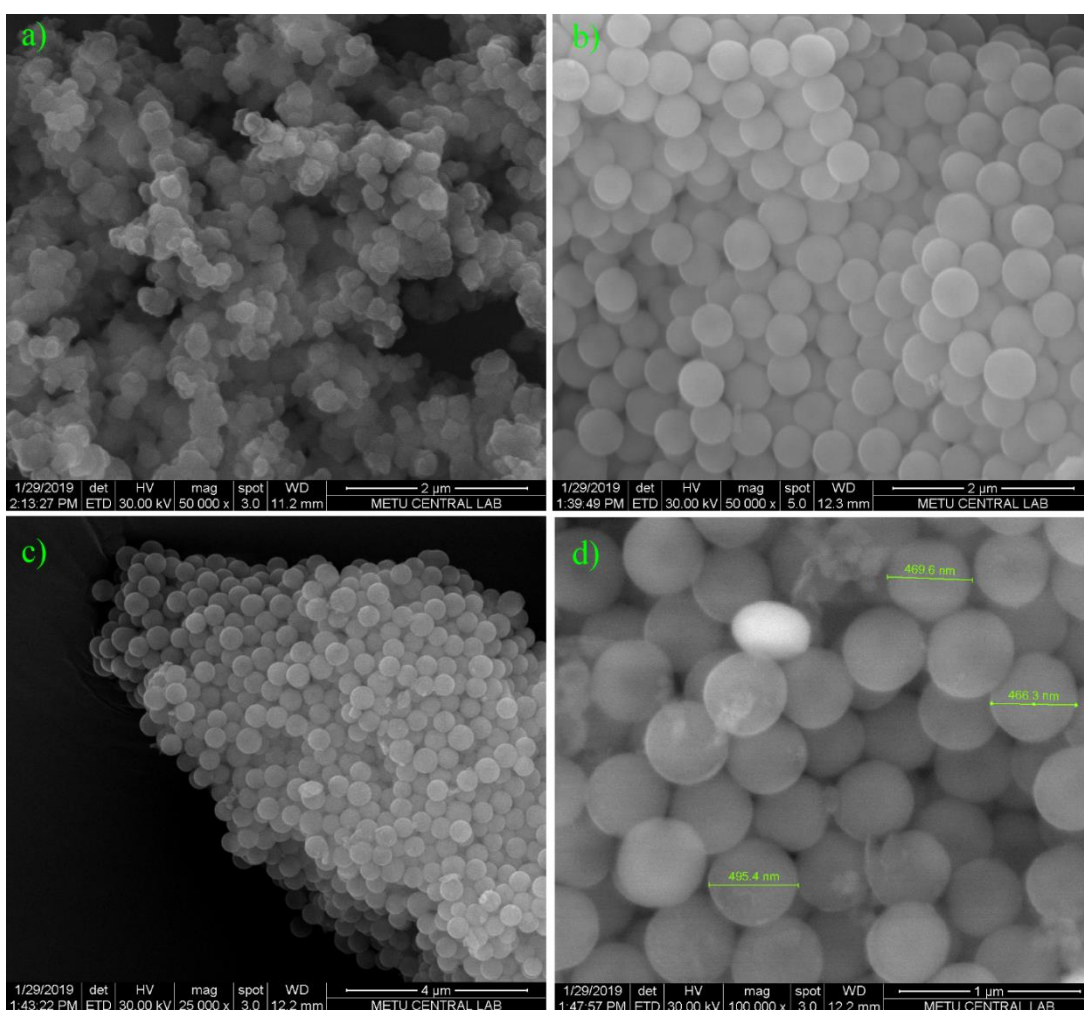


Figure 40. (a) SEM images of single silica-coated  $Gd_{0.90}Ce_{0.05}Tb_{0.05}BO_3$  samples (b-c-d) double silica-coated  $Gd_{0.90}Ce_{0.05}Tb_{0.05}BO_3$  samples.

#### 4.7. FTIR Spectroscopy

$Gd_{0.90}Ce_{0.05}Tb_{0.05}BO_3$ ,  $Gd_{0.90}Ce_{0.05}Tb_{0.05}BO_3@SiO_2$  and CLX loaded  $Gd_{0.90}Ce_{0.05}Tb_{0.05}BO_3@SiO_2$  samples were analyzed to determine the chemical groups. In figure 41, tetrahedral  $BO_4$  group stretching frequencies are observed at 824, 908, 979 and 1059  $cm^{-1}$  and  $BO_3$  peaks are observed around 1408  $cm^{-1}$ . In a similar study, Severoğlu et al. have synthesized vaterite type  $GdBO_3$  and have not observed any isolated  $BO_3$  peaks, this result indicates that there is only tetrahedral  $B_3O_9^{9-}$

formation in their GdBO<sub>3</sub> structure. However in our study, there is a coexistence of BO<sub>3</sub> and BO<sub>4</sub> which means that there are open B<sub>3</sub>O<sub>9</sub><sup>9-</sup> rings in our GdBO<sub>3</sub> structure as mentioned before (Zhang et al., 2015). Also, although there are Ce and Tb as dopants in GdBO<sub>3</sub> structure, there are no extra peaks and no significant changes in FTIR spectrum, meaning that GdBO<sub>3</sub> structure is not disturbed.

For silica coated and drug loaded samples, Si-OH stretching peaks were observed around 3450 cm<sup>-1</sup> as expected. Also, around 1650 cm<sup>-1</sup>, Si-O stretching can be seen. These results tell us that the GdBO<sub>3</sub> core samples were coated with silica successfully.

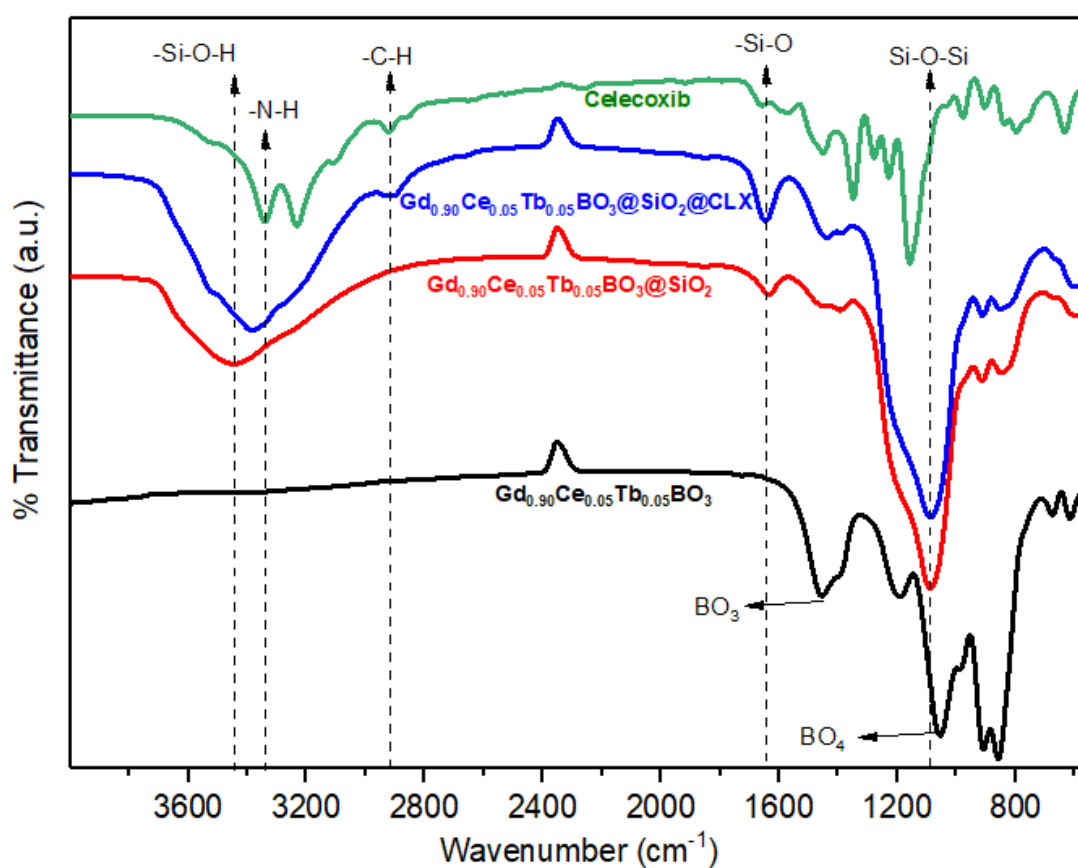


Figure 41. FTIR spectra of pure Celecoxib, drug-loaded samples, core/shell and core particles.

Celecoxib drug has certain N-H and C-H stretching peaks in FTIR spectroscopy at around  $3400\text{ cm}^{-1}$  and  $2900\text{ cm}^{-1}$  respectively. For drug loaded samples, C-H stretching peaks coming from Celecoxib was observed at  $2900\text{ cm}^{-1}$ . Also, N-H stretching peak has led to a shift for drug loaded sample from  $3450\text{ cm}^{-1}$  to  $2900\text{ cm}^{-1}$ . We can understand from these Celecoxib peaks that our drug carrier has certain amount of Celecoxib adsorbed.

#### **4.8. Nitrogen adsorption-desorption analysis**

##### **4.8.1. Brauner-Emmett-Teller (BET) method**

Surface characteristics of porous materials can be investigated by Brauner-Emmett-Teller (BET) theory. Nitrogen adsorption and desorption analysis is done at constant temperature and different pressures and the adsorbed volume is measured. Surface area of the material, pore volume and pore diameter can be found by this way. This analysis was done to core/shell particles and drug loaded core/shell particles to find out the effect of Celecoxib loading on the pore volume, pore diameter and surface area. Surface characteristics of mesoporous materials are examined by the type IV BET isotherms. For this type of isotherm, nitrogen gas is sent to the system until it shows a sharp increase around  $P/P_0 = 0.9$ . After that point, nitrogen gas starts to be condensed in the pores of the mesoporous material and reaches saturation point. This sharp increase around 0.9 shows the narrow pore volume distribution and an ordered mesostructure. Also, pore volume vs. relative pressure curves show that the adsorption-desorption process is reversible. This reversible character of the material tells that pore volume distribution is narrow, otherwise, there would be a large hysteresis curve with an irreversible process (Kruk, Jaroniec, & Sayari, 2002).

In order to analyze the surface properties before and after Celecoxib loading, BET method was used and Figure 42 shows the hysteresis loops. As can be seen in the figure, there is a decrease in pore volume after drug loading. This means that Celecoxib drug was adsorbed not only on the surface, but also inside the pores and channels of mesoporous silica shell.

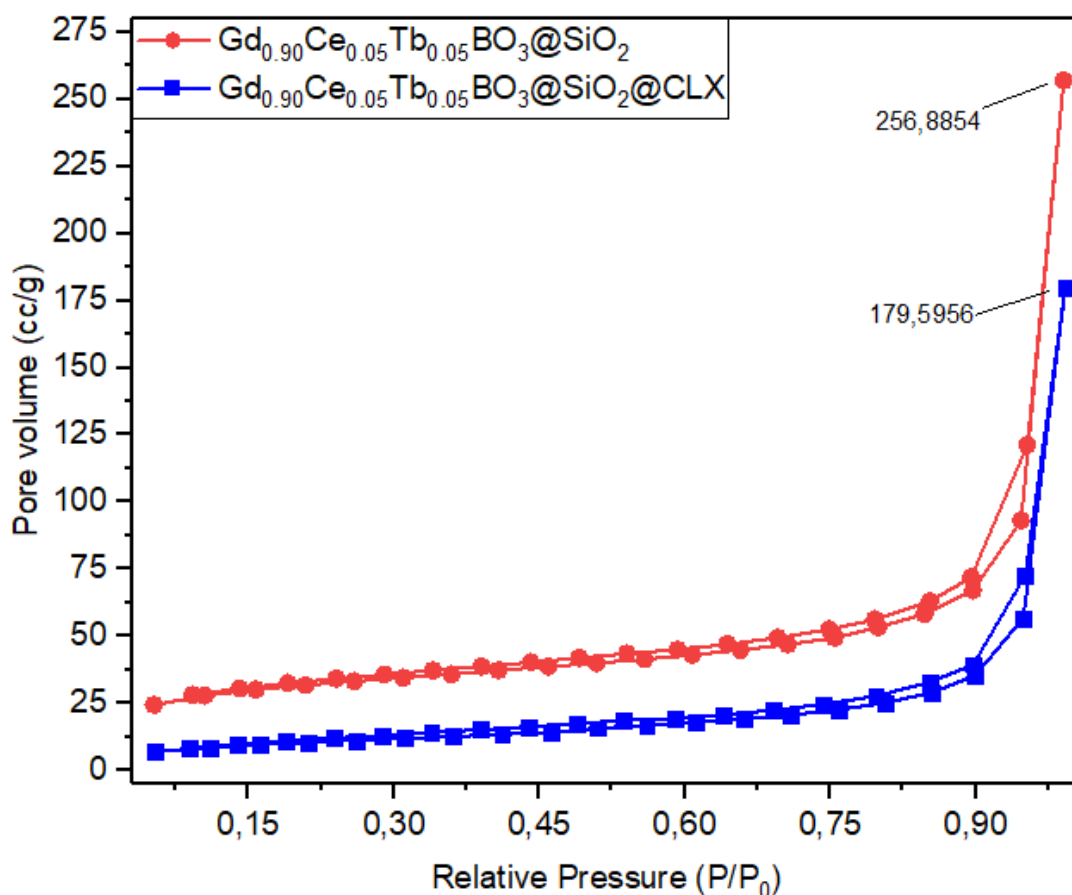


Figure 42. Pore volume vs. relative pressure graph of drug-loaded samples and core/shell samples.

#### 4.8.2. Barret-Joyner-Halenda (BJH) method

Pore size distribution of the porous materials can be examined by Barret-Joyner-Halenda (BJH) method. Pore size calculations were done according to the Kelvin equation,  $\ln(P/P_0) = 2\gamma V_m / rRT$  where  $P$  is the actual pressure,  $P_0$  is the saturated pressure,  $\gamma$  is surface tension,  $V_m$  is the molar volume of the liquid,  $r$  is the radius of the droplet,  $R$  is the universal gas constant and  $T$  is temperature. This equation was used by assuming that the pores are in cylindrical and homogeneous. Figure 43 shows the pore diameter of core/shell particles before and after Celecoxib loading. According to the figure, pore diameter of silica shell is between 6.5 nm and 9.5 nm before drug

loading and after drug loading, pore diameter is about 2 nm. Therefore, it can be said that the Celecoxib drug fills the pores of mesoporous silica shell.

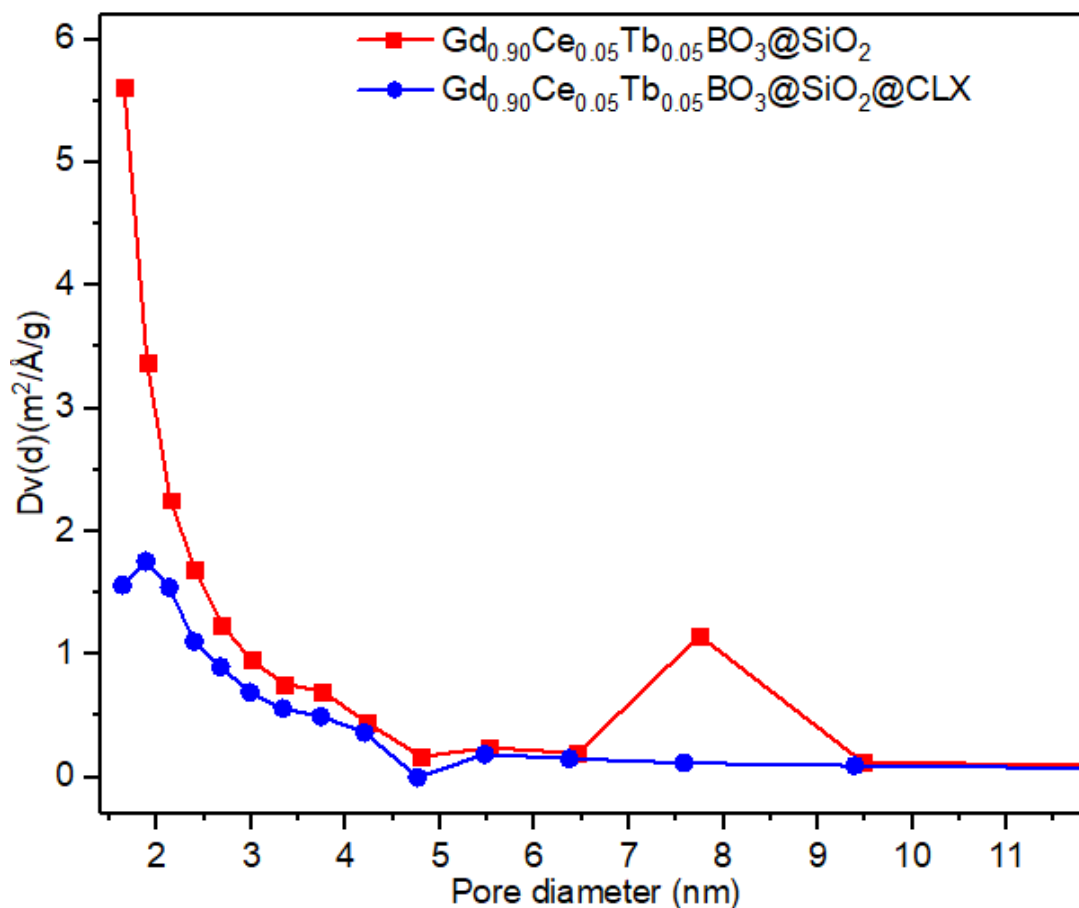


Figure 43. Pore size distribution of  $Gd_{0.90}Ce_{0.05}Tb_{0.05}BO_3@SiO_2$  and drug loaded samples,  $Gd_{0.90}Ce_{0.05}Tb_{0.05}BO_3@SiO_2@CLX$ .

#### 4.9. Thermogravimetric analysis (TGA)

Thermogravimetric analysis (TGA) shows the weight loss of the material as the temperature increases. There is a comparison of TGA curves of core/shell particles and Celecoxib loaded core/shell particles in Figure 44. There is a certain amount weight loss for Celecoxib loaded samples between 200-600°C which indicates the

thermal degradation of Celecoxib drug. There is a small weight loss until 200°C which means the loss of adsorbed water and gases such as CO<sub>2</sub>, NO<sub>x</sub>, SO<sub>x</sub>, NH<sub>3</sub>. The drug loading efficiency was calculated from the TGA curves as 21.8% which supports the UV-VIS drug loading results.

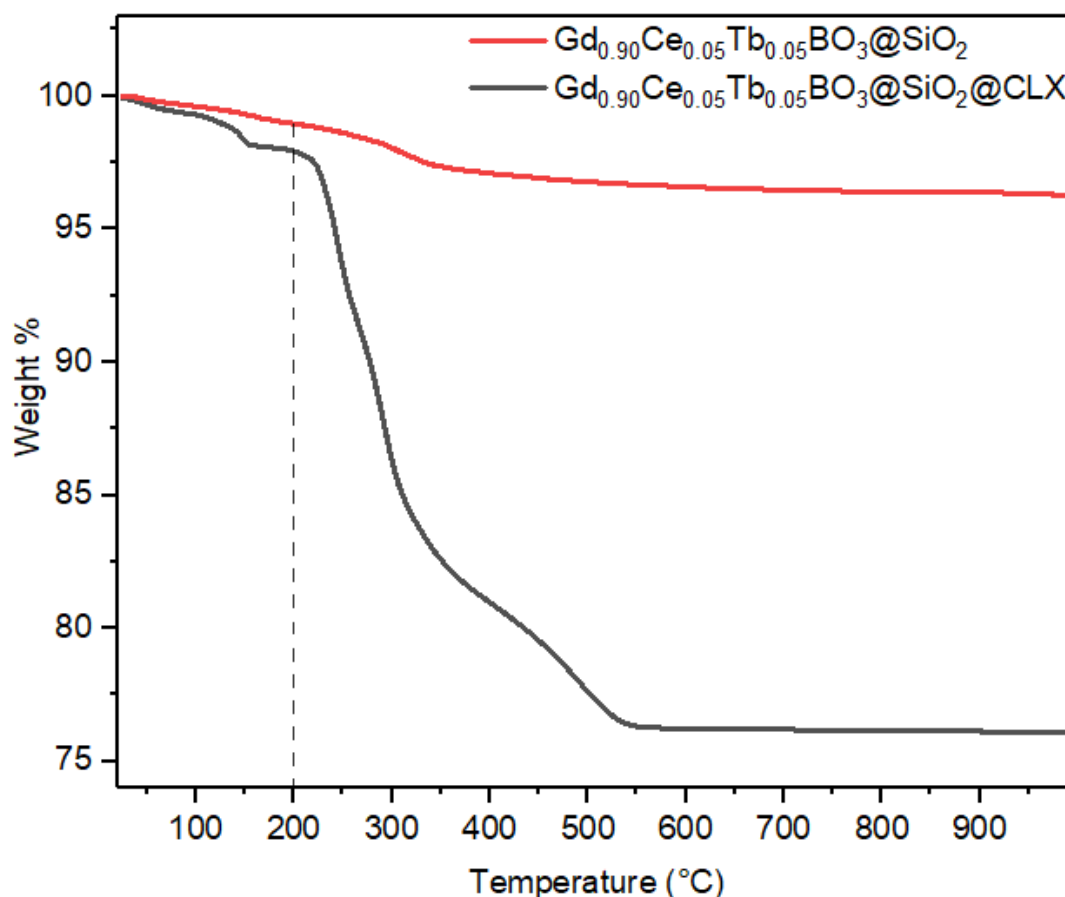


Figure 44. TGA curves of the core/shell particles and Celecoxib loaded core/shell particles.

#### 4.10. Vibrating-sample magnetometer (VSM)

The magnetization curves at room temperature, 20 K and 2 K were recorded for  $Gd_{0.90}Ce_{0.05}Tb_{0.05}BO_3$  core and magnetization of core/shell and drug loaded core/shell materials were recorded at room temperature. In Figure 45, there are the magnetization

curves for core, core/shell and Celecoxib loaded samples. Small areas observed for hysteresis loops and low values of coercivity (Table 5) indicates the soft magnetic properties of  $Gd_{0.90}Ce_{0.05}Tb_{0.05}BO_3$ .

Table 4. Magnetization values of core, core/shell and Celecoxib loaded core/shell materials.

	$Gd_{0.90}Ce_{0.05}Tb_{0.05}BO_3$	$Gd_{0.90}Ce_{0.05}Tb_{0.05}BO_3 @SiO_2$	$Gd_{0.90}Ce_{0.05}Tb_{0.05}BO_3 @SiO_2@CLX$
Magnetic susceptibility	1,10 emu/g	0,41 emu/g	0,37 emu/g

Magnetic susceptibility of  $\beta-NaYF_4:Gd^{3+} / Tb^{3+}$  particles were found 0,76 emu/g (Padhye et al., 2015) and in our study, magnetic susceptibility is much higher, 1.10 emu/g, which means that our drug carrier can be used as an MRI contrast agent in the future.

Table 5. Coercivity values of core, core/shell and Celecoxib loaded core/shell materials.

	H <sub>C</sub> (Tesla) 298 K	H <sub>C</sub> (Tesla) 20 K	H <sub>C</sub> (Tesla) 2 K
$Gd_{0.90}Ce_{0.05}Tb_{0.05}BO_3$	0.00548	0.00388	0.00441
$Gd_{0.90}Ce_{0.05}Tb_{0.05}BO_3 @SiO_2$	0.00979	-	-
$Gd_{0.90}Ce_{0.05}Tb_{0.05}BO_3 @SiO_2 @CLX$	0.00922	-	-

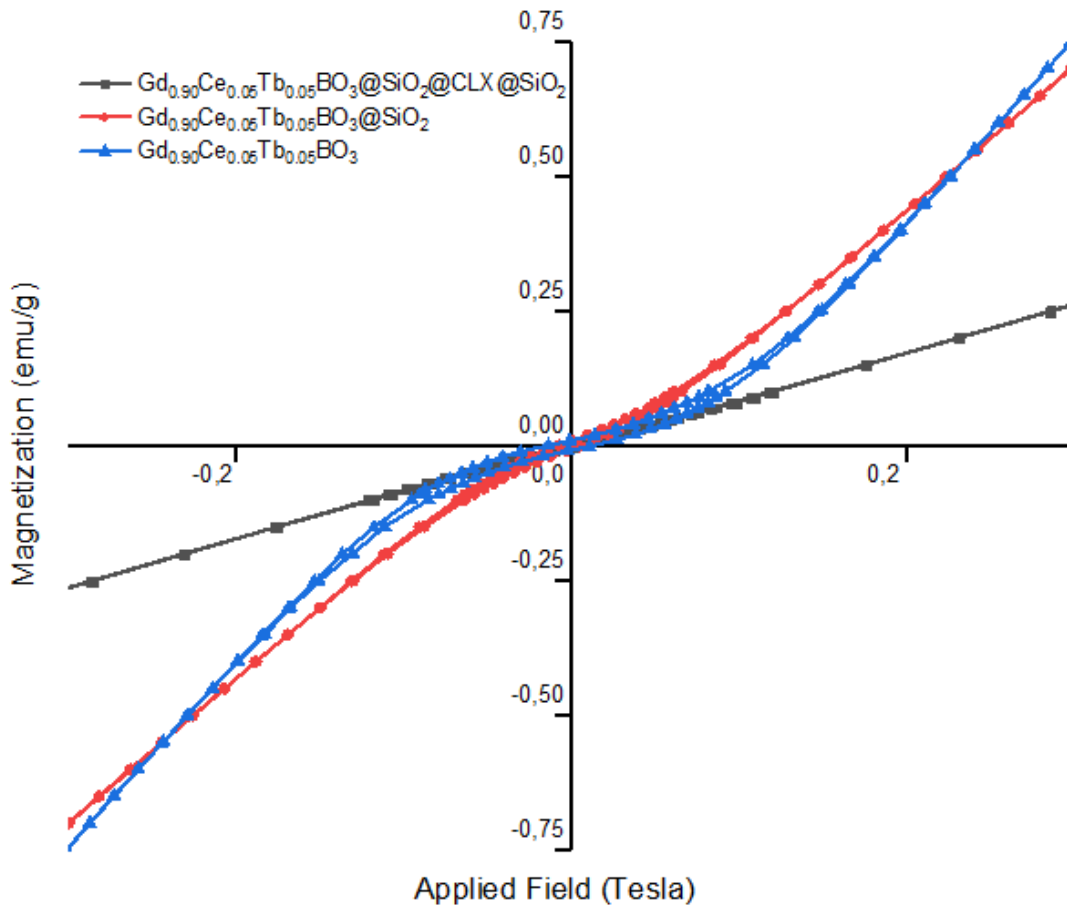


Figure 45. Magnetization curves of the core, core/shell particles and Celecoxib loaded core/shell particles.

In order to be used as an MRI contrast agent, magnetization of the samples are important. For example, in literature there is a similar study including a Gd-based drug carrier and in this study, scientists have used this magnetic nanoparticle as Doxorubicin drug carrier and also MRI contrast agent. When we look at the highest magnetization values, our drug carrier has about 0.75 emu/g where in this study there is about 0.40 emu/g. To compare, our product has a higher magnetization value so it can be used as an MRI contrast agent, too (Li et al., 2013).

Magnetic susceptibility value for  $Gd_{0.90}Ce_{0.05}Tb_{0.05}BO_3$  was determined as 1.10 emu/g. In literature, Gd based drug carrier used as MRI contrast agent has 0.76 emu/g

susceptibility value (Padhye et al., 2015). This comparison supports the MRI contrast agent potential of our drug carrier.

#### 4.11. Zeta-potential

Zeta potential measurements are done to get information about the electrical charge of the silica surface and drug loaded silica surface. For the analysis, 1.0 mg of core/shell particles with and without Celecoxib drug is suspended in 50 ml deionized water.

Table 6. Zeta potential results for core, core/shell and Celecoxib loaded core/shell samples.

Sample	Zeta potential (mV) in deionized water at pH 7.0, 25°C
Double silica coating to $Gd_{0.90}Ce_{0.05}Tb_{0.05}BO_3$	$-12.7 \pm 2.6$
CLX - Double silica coating to $Gd_{0.90}Ce_{0.05}Tb_{0.05}BO_3$	$-14.9 \pm 1.8$

Table 6 shows the zeta potentials of double silica coated  $Gd_{0.90}Ce_{0.05}Tb_{0.05}BO_3$  particles and the drug loaded samples. For double-silica coating, it is expected to observe a negatively charged surface since there are silanol groups on the silica surface. For drug loaded samples there is a smaller value,  $-14.9 \pm 1.8$  than core/shell materials' potential. However, it is expected to see an increase in zeta potential values as Celecoxib is a positively charged drug and when combined with silica surface, there must be a neutralization of the negative charge (Venkatesan et al., 2011). This may be explained by the adsorption of the drug inside silica channels is much more than the adsorption on the surface, so surface charge did not change much after drug loading.

#### 4.12. UV-VIS analysis

In order to quantify the amount of drug loaded on the samples and released in PBS media, UV-VIS spectrometry was used. Celecoxib drug shows absorbance at 254 nm and calculations are done by using Beer Lambert's law.

#### 4.12.1. Celecoxib loading

For the quantification of the drug loading, UV-VIS spectrometry is used. In our study, standard solutions of Celecoxib were prepared with concentrations of  $8.0 \times 10^{-6}$ ,  $1.6 \times 10^{-5}$ ,  $2.5 \times 10^{-5}$ ,  $3.0 \times 10^{-5}$  and  $4.5 \times 10^{-5}$  M in ethanol. The absorbance values and concentrations were used to obtain following calibration curve, Figure 46.

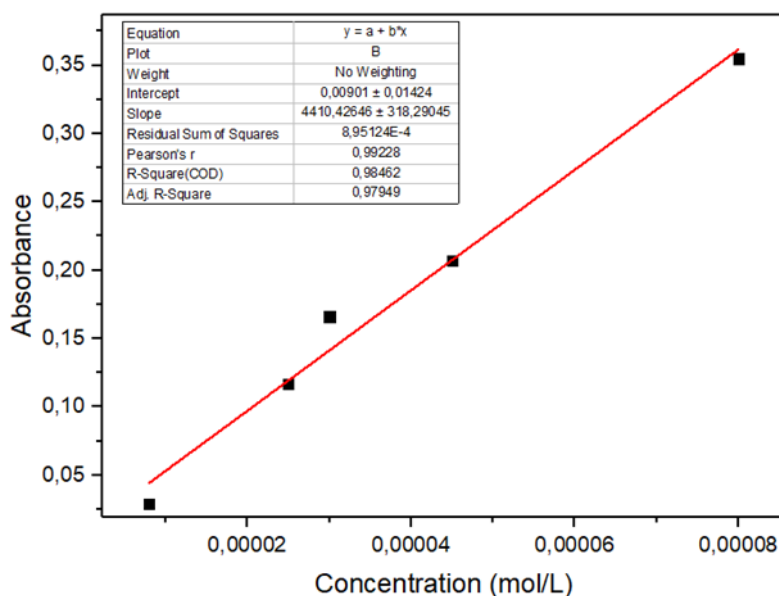


Figure 46. Calibration curve prepared by different Celecoxib concentrations in ethanol.

The slope of the calibration curve gives the molar absorptivity coefficient as  $4410.42 \text{ L cm}^{-1} \text{ mol}^{-1}$ . In order to calculate drug loading percentage, the solution was kept after drug loading and UV analysis was done to calculate remaining drug in the solution. Since the initial concentration of the drug is known, drug loading amount was calculated by subtracting the remaining from the initial. According to Beer Lambert's law, the amount of loaded Celecoxib was calculated as 24 %.

#### 4.12.2. Celecoxib release

Drug release studies were done for Celecoxib loaded particles and Celebrix in powder form, which is the commercially available drug. The amount of Celecoxib released

from the  $Gd_{0.90}Ce_{0.05}Tb_{0.05}BO_3@SiO_2$  carrier and Celebrex was quantified by using UV-VIS spectrophotometry at 254 nm. Phosphate buffer solution (PBS) was prepared by mixing 8.00 g of NaCl, 0.20 g of KCl, 1.44 g of  $Na_2HPO_4$  and 0.24 g of  $KH_2PO_4$  in 800 ml deionized water. The pH of this solution was adjusted to 7.4 and the mixture was completed to 1.0 L. A mixture of 50 mL of PBS with a pH of 7.4 and 100 mg of drug loaded samples were prepared and 37°C temperature was maintained to simulate body temperature. After 30 minutes, 1 h, 2 h, 4 h, 6 h, 8 h, 12 h and 24 h, 5 mL of release mixture was taken and to keep the volume constant, a fresh aliquot of 5 mL of PBS solution was added to the mixture. Absorbance values of these 5 mL-samples were obtained by UV-VIS spectrophotometry and Beer Lambert's law was used to calculate the amount of Celecoxib released.

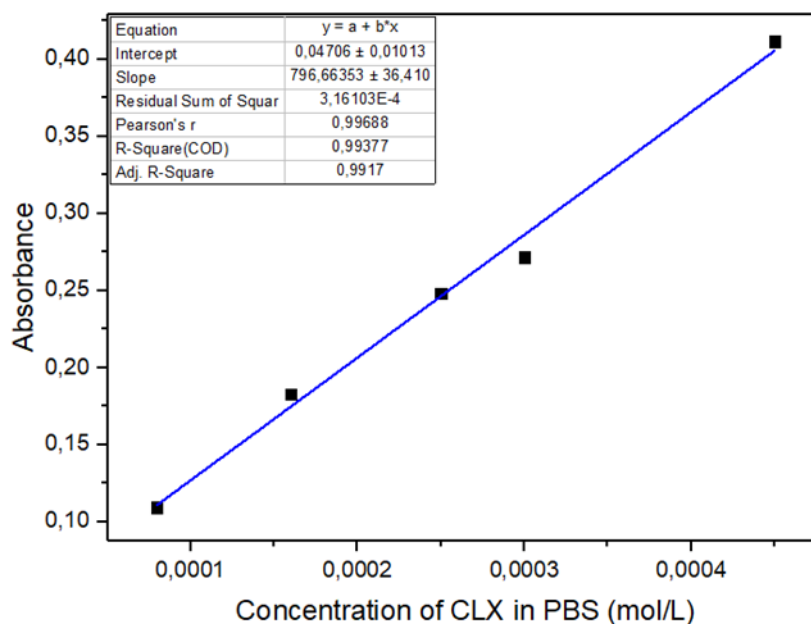


Figure 47. Calibration curve prepared by different Celecoxib concentrations in PBS.

In order to complete the calculations, a calibration curve was drawn by UV-VIS analyses of solutions with different Celecoxib concentrations which are  $8.0 \times 10^{-6}$ ,

$1.6 \times 10^{-5}$ ,  $2.5 \times 10^{-5}$ ,  $3.0 \times 10^{-5}$  and  $4.5 \times 10^{-5}$  M in PBS. The slope of the calibration curve,  $796.66353 \text{ L cm}^{-1} \text{ mol}^{-1}$  was used as  $\epsilon$  in Beer Lambert's  $A = \epsilon bc$  formula as can be seen in the Figure 47.

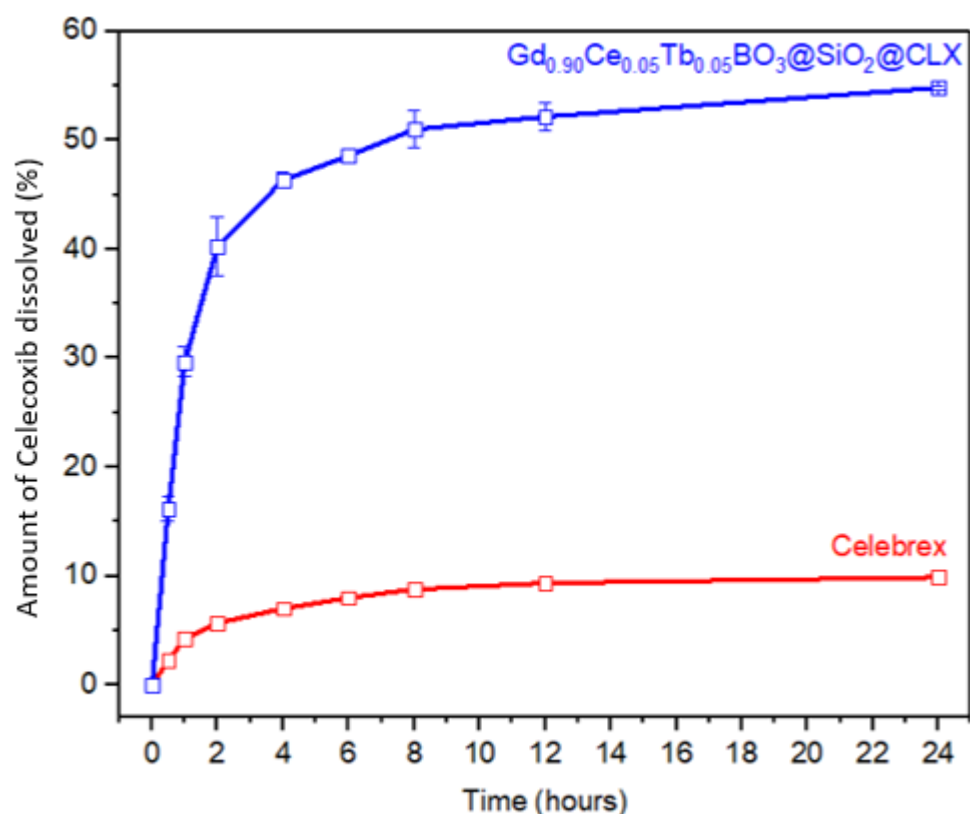


Figure 48. Celecoxib release profile of  $\text{Gd}_{0.90}\text{Ce}_{0.05}\text{Tb}_{0.05}\text{BO}_3@SiO_2$  carrier in PBS with a pH of 7.4.

The comparison of in vitro dissolution behavior of  $\text{Gd}_{0.90}\text{Ce}_{0.05}\text{Tb}_{0.05}\text{BO}_3@SiO_2$  and Celebrex can be seen in Figure 48. In the first 30 minutes, there was a burst release due to the surface adsorbed Celecoxib but in general, there is a slow Celecoxib release for  $\text{Gd}_{0.90}\text{Ce}_{0.05}\text{Tb}_{0.05}\text{BO}_3@SiO_2$  carrier. From the figure, it can be said that the solubility of Celecoxib was enhanced by using  $\text{Gd}_{0.90}\text{Ce}_{0.05}\text{Tb}_{0.05}\text{BO}_3@SiO_2$  carrier.

#### 4.13. Cell proliferation assay

Since CLX has previously been shown to have chemopreventive effects in colorectal cancer (Koehne & Dubois, 2004), HCT-116 colon cancer cells were chosen as models to investigate whether CLX released from silica particles could affect cellular viability. HCT-116 cells were seeded on 96-well plate at a concentration of 10,000 cell/well. After 24 hours, this time cells were treated with 500, 100, 50, 10 and 1  $\mu\text{g}/\text{mL}$  concentration of  $\text{Gd}_{0.90}\text{Ce}_{0.05}\text{Tb}_{0.05}\text{BO}_3$  core,  $\text{Gd}_{0.90}\text{Ce}_{0.05}\text{Tb}_{0.05}\text{BO}_3@ \text{SiO}_2$  drug carrier without drug, drug loaded  $\text{Gd}_{0.90}\text{Ce}_{0.05}\text{Tb}_{0.05}\text{BO}_3@ \text{SiO}_2$  and Celebrex (4 technical replicates were used). The pure drug amount was 1/3 of the total mass. Therefore 500  $\mu\text{g}/\text{ml}$  of drug means 500/3  $\mu\text{g}/\text{ml}$  of actual powder. Untreated cells were also included as a control. After 24 hours of treatment medium containing nanoparticles were changed to MTT reagent containing medium and MTT protocol was followed to get the absorbance values at 570 nm.

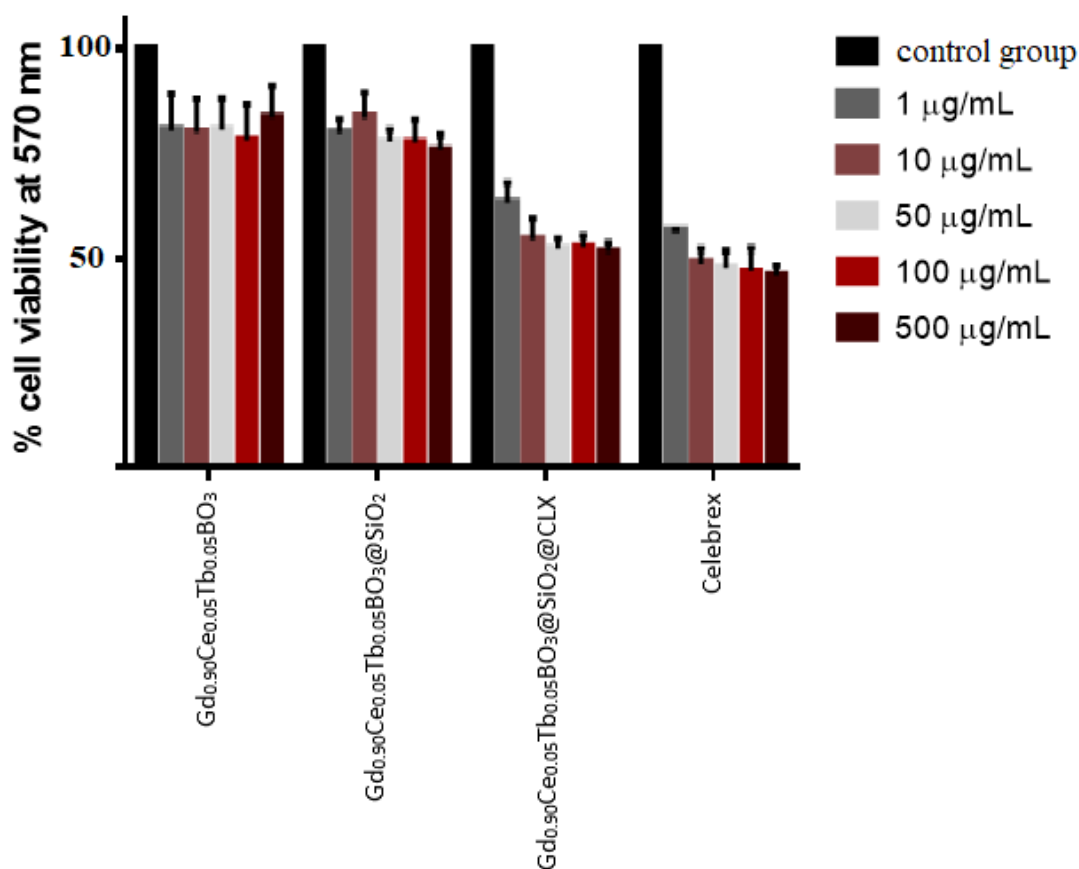


Figure 49. MTT result showing the viability of HCT-116 cells after treated with core, empty/drug loaded drug carrier and drug only at different concentrations.

The results were shown in the Figure 49. High absorbance values mean that the cells are alive, so only cells treated with Celecoxib loaded carrier are consisted in that when the concentration of the drug is increased, the viability of the cells is decreasing. Statistically significant decreases in viability of cells were seen in the CLX loaded samples compared to the unloaded samples. Celebrex shows more concentration dependent decrease than drug loaded particles but it may mean that some of the drug still stays inside the particles or maybe more time needed to release all of the drug.

## CHAPTER 5

### CONCLUSION

In this study, core/shell type luminescent and magnetic  $\text{Gd}_{0.90}\text{Ce}_{0.05}\text{Tb}_{0.05}\text{BO}_3@\text{SiO}_2$  particles were synthesized successfully. For the synthesis of  $\text{Gd}_{0.90}\text{Ce}_{0.05}\text{Tb}_{0.05}\text{BO}_3$  core, sol-gel method was used and it is understood that EDTA is a much better chelating agent compared to citric acid since the XRD pattern of EDTA synthesis is pure. Also, the particle size is much smaller and agglomeration is low for EDTA synthesis. Photoluminescence spectra were collected for the samples with different dopant concentrations and 5 % Ce, 5 % Tb doped  $\text{GdBO}_3$  was determined to have the highest PL intensity. Also, magnetic susceptibility was measured high enough to be used as an MRI contrast agent. The quantum yield efficiency of these particles were measured as 42%. Double silica coating to  $\text{Gd}_{0.90}\text{Ce}_{0.05}\text{Tb}_{0.05}\text{BO}_3$  core was successful in producing core/shell type particles. Crystal structure of  $\text{GdBO}_3$ , PL intensity and magnetic susceptibility values were either conserved or dropped slightly after silica coating and Celecoxib loading. A drug loading efficiency of 24% was reached. Celecoxib release rate and dissolution rate were enhanced by using  $\text{Gd}_{0.90}\text{Ce}_{0.05}\text{Tb}_{0.05}\text{BO}_3@\text{SiO}_2$  drug carrier when compared to commercial drug Celebrex. The cytotoxicity tests show that the drug carrier increases the biocompatibility of the Celecoxib. All of the results here confirm that  $\text{Gd}_{0.90}\text{Ce}_{0.05}\text{Tb}_{0.05}\text{BO}_3@\text{SiO}_2$  nanoparticles are promising drug carriers and also bioimaging agents.



## REFERENCES

- Allen, T. M., & Cullis, P. R. (2004). Drug Delivery Systems: Entering the Mainstream. *Science*, 303(5665), 1818–1822.
- Andersson, J., Rosenholm, J., Areva, S., & Lindén, M. (2004). Influences of material characteristics on ibuprofen drug loading and release profiles from ordered micro- and mesoporous silica matrices. *Chemistry of Materials*, 16(21), 4160–4167.
- Antoni, M. (2015). Inorganic Synthesis Methods for Nanostructured Capacitors.
- Bahadur, A., Yadav, R. S., Yadav, R. V., & Rai, S. B. (2017). Multimodal emissions from Tb<sup>3+</sup>/Yb<sup>3+</sup>-co-doped lithium borate glass: Upconversion, downshifting and quantum cutting. *Journal of Solid State Chemistry*, 246(October 2016), 81–86.
- Bao, G., Mitragotri, S., & Tong, S. (2013). Multifunctional Nanoparticles for Drug Delivery and Molecular Imaging. *Annual Review of Biomedical Engineering*, 15(1), 253–282.
- Caruso, F., Hyeon, T., Rotello, V., & Zink, J. I. (2012). Mesoporous silica nanoparticles in biomedical applications. *Chem Soc Rev*, 41(7), 2590–2605.
- Chadeyron, G., Mahiou, R., Arbus, A., & Cousseins, J. C. (1997). Revised Structure of the Orthoborate YBO<sub>3</sub>. *Journal of Solid State Chemistry*, 266(128), 261–266.
- Chaudhuri, R. G., & Paria, S. (2012). Core / Shell Nanoparticles : Classes , Properties , Synthesis Mechanisms , Characterization , and Applications. 2373–2433.
- Cornejo, C. R. (2016). Luminescence in Rare Earth Ion-Doped Oxide Compounds. In *Luminescence - An Outlook on the Phenomena and their Applications*.
- Cox, J. R., & Keszler, D. A. (2002). InBO<sub>3</sub>. *Acta Crystallographica Section C Crystal Structure Communications*, 50(12), 1857–1859.
- Dieke, G. H., & Satten, R.A. (1970). Spectra and Energy Levels of Rare Earth Ions in Crystals. *American Journal of Physics*, 38(3), 399–400.
- Dorosz, D., Kochanowicz, M., Zmojda, J., Miluski, P., & Marciniak, M. (2015). Rare-Earth Doped Materials for Optical Waveguides. *ICTON2015*, 2–6.
- Duan, Q., Qin, F., Wang, P., Zhang, Z., & Cao, W. (2013). Upconversion emission efficiency of Tb<sup>3+</sup>-Yb<sup>3+</sup>-codoped glass. *J. Opt. Soc. Am. B* 30, 456–459.
- Dwars, T., Paetzold, E., & Oehme, G. (2005). Reactions in Micellar Systems. *Angewandte Chemie*, 7174–7199.
- Edinst.com. (2019). [online] Available at: <https://www.edinst.com/wp->

content/uploads/2016/02/FLS980-Series-Reference-Guide-Integrating-Sphere.pdf [Accessed 24 Jun. 2019].

- Ehlich, P. E. F. R. Ö., Franciscano, C. U., & Andradas, R. (2005). Celecoxib Identification Methods. *Acta Farm. Bonaerense*, 24(3), 421–425.
- Eren, Z. S., Tunçer, S., Gezer, G., Yildirim, L. T., Banerjee, S., & Yılmaz, A. (2016). Improved solubility of celecoxib by inclusion in SBA-15 mesoporous silica: Drug loading in different solvents and release. *Microporous and Mesoporous Materials*, 235, 211-223.
- Eti Maden, “Bor sektör raporu,” 2017.
- Feng, J., Zhang, H., Song, S., Li, Z., Sun, L., Xing, Y., & Guo, X. (2008). Syntheses, crystal structures, visible and near-IR luminescent properties of ternary lanthanide ( $Dy^{3+}$ ,  $Tm^{3+}$ ) complexes containing 4,4,4-trifluoro-1-phenyl-1,3-butanedione and 1,10-phenanthroline. *Journal of Luminescence*, 128, 1957–1964.
- Gai, B. S., Yang, P., Li, C., Wang, W., Dai, Y., Niu, N., & Lin, J. (2010). Synthesis of Magnetic , Up-Conversion Luminescent , and Mesoporous Core – Shell-Structured Nanocomposites as Drug Carriers. *Advanced Functional Materials*, 1166–1172.
- Geraldes, C. F. G. C., & Laurent, S. (2009). Classification and basic properties of contrast agents for magnetic resonance imaging. (December 2008). *Contrast Media Mol. Imaging*, 2009, 4 1–23.
- Giesber, H. G., Ballato, J., Pennington, W. T., & Kolis, J. W. (2003). Synthesis and characterization of optically nonlinear and light emitting lanthanide borates. *Information Sciences*, 149, 61–68.
- Hwang, G., Jeon, H., & Kim, Y. (2002). Physical Properties of Barrier Ribs of Plasma Display Panels : I , Formation of Pores during Sintering of Lead Borosilicate Glass Frits. *Journal of the American Ceramic Society*, 60(187983), 2956–2960.
- Jain, T. K., Richey, J., Strand, M., Leslie-pelecky, D. L., Flask, C. A., & Labhasetwar, V. (2008). Biomaterials Magnetic nanoparticles with dual functional properties : Drug delivery and magnetic resonance imaging. *Biomaterials*, 29, 4012–4021.
- Khalid, A. H., & Kontis, K. (2008). Thermographic Phosphors for High Temperature Measurements: Principles, Current State of the Art and Recent Applications. *Sensors*, 5673–5744.
- Koehne, C. H., & Dubois, R. N. (2004). *Semin Oncol*, 31[2 Suppl 7]:12-21.
- Kruk, M., & Jaroniec, M. (1997). Application of Large Pore MCM-41 Molecular Sieves To Improve Pore Size Analysis Using Nitrogen Adsorption Measurements. *Langmuir*, 7463(12), 6267–6273.

- Kubasiewicz, K., Runowski, M., Lis, S., & Szczeszak, A. (2015). Synthesis, structural and spectroscopic studies on GdBO<sub>3</sub>:Yb<sup>3+</sup>/Tb<sup>3+</sup>@SiO<sub>2</sub> core-shell nanostructures. *Journal of Rare Earths*, 33(11), 1148–1154.
- Kumar, D.S., Kumar, B.J., Mahesh, H. (2018). Synthesis of Inorganic Nanomaterials. *Elsevier*, 2018, 59-88.
- Lakowicz, J.R. Principles of fluorescence spectroscopy, Springer.
- Li, C., Yang, D., Ma, P., Chen, Y., Wu, Y., & Hou, Z. (2013). Nanostructures for Dual Modal Imaging and In Vivo Drug Delivery. *Small*, (24), 4150–4159.
- Li, P., Song, Y., Niu, X., Li, K., & Fan, Y. (2019). Drug Delivery System with Multiple Rare Earth Ions Fluorescent-Labeling Drugs and Magnetic Nanoparticles. *Journal of Nanoscience and Nanotechnology*, 19(6), 3288–3292.
- Li, Y., Zhang, J., Zhang, X., Luo, Y., Lu, S., Ren, X., Yan, C. (2009). Luminescent Properties in Relation to Controllable Phase and Morphology of LuBO<sub>3</sub>: Eu<sup>3+</sup> Nano / Microcrystals Synthesized by Hydrothermal Approach. *Chemistry of Materials*, (3), 468–475.
- Liechty, W.B., Kryscio, D.R., Slaughter, B.V., Peppas, N.A. (2010). Polymers for Drug Delivery Systems. *Annu Rev Chem Biomol Eng*, 1, 149-173.
- Liu, G., Chen, K., & Li, J. (2018). Scripta Materialia Combustion synthesis : An effective tool for preparing inorganic materials. *Scripta Materialia*, 157, 167-173.
- Liu, J., Bu, W., Pan, L., & Shi, J. (2013). NIR-Triggered Anticancer Drug Delivery by Upconverting Nanoparticles with Integrated Azobenzene-Modified Mesoporous Silica. *Angewandte Chemie*, 52(16) 4375-4379.
- Livage, J., & Pierre, U. (2016). Inorganic Materials , Sol – Gel Synthesis of \*. *Materials Science and Materials Engineering*, (April 2015), 1–4.
- Lucas, J., Lucas, P., Le Mercier, T., Rollat, A., Davenport, W. (2015). Introduction to Rare Earth Luminescent Materials. *Elsevier*, 251-280.
- Ma, Y., Chen, Z., Chu, Y., Yang, Y., Liu, Y., Li, H., & Peng, J. (2018). Regulation of gold nanoparticles for the rare earth luminescence enhancement based on nanoporous silica glass. *Journal of Luminescence*, 204(July), 104–109.
- Matea, C. T., Mocan, T., Tabaran, F., Pop, T., Mosteanu, O., Puia, C., ... Mocan, L. (2017). Quantum dots in imaging, drug delivery and sensor applications. *International Journal of Nanomedicine*, 12, 5421–5431.
- Murthy, K. V. R., & Virk, H. S. (2014). Luminescence Phenomena : An Introduction. *Defect and Diffusion Forum*, 347, 1–34.
- Narayanan, S., Sathy, B. N., Mony, U., Koyakutty, M., Nair, S. V, & Menon, D.

- (2012). Biocompatible Magnetite/Gold Nanohybrid Contrast Agents via Green Chemistry for MRI and CT Bioimaging. *ACS Applied Materials and Interfaces*, 4(1), 251-260.
- Nevozhay, D., Kańska, U., Budzyńska, R., & Boratyński, J. (2007). Current status of research on conjugates and related drug delivery systems in the treatment of cancer and other diseases. *Postępy Higieny i Medycyny Doświadczalnej*, 61, 350–360.
- Peijzel, P. S., Meijerink, A., Wegh, R. T., Reid, M. F., & Burdick, G. W. (2005). A complete 4 f n energy level diagram for all trivalent lanthanide ions. *Journal of Solid State Chemistry*, 178, 448–453.
- Qiao, Y., Li, S., Liu, W., Ran, M., Lu, H., & Yang, Y. (2018). Recent Advances of Rare-Earth Ion Doped Luminescent Nanomaterials in Perovskite Solar Cells. *Nanomaterials*, 8(1)
- Qiao, Y., Sergentu, D., Yin, H., Zabula, A. V, Cheisson, T., Mcskimming, A., Schelter, E. J. (2018). Understanding and Controlling the Emission Brightness and Color of Molecular Cerium Luminophores. *Journal of the American Chemical Society*, 140(13), 4588-4595.
- Qin, C., Qin, L., Chen, G., & Lin, T. (2013). One-dimensional Eu<sup>3+</sup> and Tb<sup>3+</sup> doped LaBO<sub>3</sub> nano fibers: Fabrication and improved luminescence performances. *Materials Letters*, 106, 436–438.
- Ren, M., Lin, J. H., Dong, Y., Yang, L. Q., & Su, M. Z. (1999). Structure and Phase Transition of GdBO<sub>3</sub>. *Chemistry of Materials*, 11(6), 1576–1580.
- Ronda, C. R. (2007). Luminescence: From Theory to Applications. Weinheim, Germany: Wiley-VCH Verlag GmbH & Co. KGaA.
- Ruvalcaba, C. (2016). Luminescence in Rare Earth Ion-Doped Oxide Compounds.
- Sao, R., Vaish, R., & Sinha, N. (2015). Multifunctional Drug Delivery Systems Using Inorganic Nanomaterials : A Review. *Luminescence*.
- Savjani, K. T., Gajjar, A. K., & Savjani, J. K. (2012). Drug Solubility : Importance and Enhancement Techniques. *ISRN Pharmaceutics*, 2012(100), 1-10.
- Selvin, P. R., & Hearst, J. E. (2006). Luminescence energy transfer using a terbium chelate: improvements on fluorescence energy transfer. *Proceedings of the National Academy of Sciences*, 91(21), 10024–10028.
- Severoğlu, M. (2016). Microwave assisted solid state synthesis of rare earth ions doped LaBO<sub>3</sub>, YBO<sub>3</sub> and GdBO<sub>3</sub>, their characterizations and investigations of luminescence properties. METU, 2016.
- Shin, J., Anisur, R., Ko, M. K., Im, G. H., Lee, J. H., & Lee, I. S. (2009). Hollow Manganese Oxide Nanoparticles as Multifunctional Agents for Magnetic

- Resonance Imaging and Drug Delivery. *Angew. Chem. Int. Ed.*, 48(2), 321–324.
- Singh, D., Singh, K., Bhagwan, S., Saini, R. K., Srivastava, R., & Singh, I. (2016). Preparation and photoluminescence enhancement in terbium ( III ) ternary complexes with  $\beta$  -diketone and monodentate auxiliary ligands. *Cogent Chemistry*, 2(1), 1–11.
- Song, S., Hidajat, K., & Kawi, S. (2005). Functionalized SBA-15 Materials as Carriers for Controlled Drug Delivery : Influence of Surface Properties on Matrix - Drug Interactions. *Langmuir*, 21(21), 9568–9575.
- Sounderya, N., Zhang, Y., & Shell, C. (2010). Use of Core / Shell Structured Nanoparticles for Biomedical Applications. *Recent Patents on Biomedical Engineering*, 2010, 34–42.
- Sun, C., Lee, J. S. H., & Zhang, M. (2008). Magnetic nanoparticles in MR imaging and drug delivery. *Advanced drug delivery reviews*, 60(11), 1252–1265.
- Szczeszak, A., Ekner-Grzyb, A., Runowski, M., Szutkowski, K., Mrówczyńska, L., Kaźmierczak, Z., Lis, S. (2016). Spectroscopic, structural and in vitro cytotoxicity evaluation of luminescent, lanthanide doped core@shell nanomaterials  $GdVO_4:Eu^{3+}5\% @SiO_2@NH_2$ . *Journal of Colloid And Interface Science*, 481, 245-255.
- Teo, R. D., Termini, J., & Gray, H. B. (2016). Lanthanides: Applications in Cancer Diagnosis and Therapy. *Journal of Medicinal Chemistry*, 59(13), 6012–6024.
- The C.I.E. Color Space. (2003). Retrieved from <http://hyperphysics.phy-astr.gsu.edu/hbase/vision/cie.html>
- Tiwari, G., Tiwari, R., Sriwastawa, B., Bhati, L., Pandey, S., Pandey, P., & Bannerjee, S. K. (2012). Drug delivery systems : An updated review. *International journal of pharmaceutical investigation*, 2(1), 2-11.
- Toennies, P. (1970). Springer Series in Chemical Physics.
- Tunc, S., Severcan, F., & Banerjee, S. (2012). Celecoxib reduces fluidity and decreases metastatic potential of colon cancer cell lines irrespective of COX-2 expression. *Biosci. Rep.*, 32, 35–44.
- Vallet-Regí, M., Balas, F., & Arcos, D. (2007). Minireviews Mesoporous Materials for Drug Delivery. *Angew. Chem. Int. Ed.*, 46, 7548 – 7558.
- Venkatesan, P., Puvvada, N., Dash, R., Kumar, B. N. P., Sarkar, D., Azab, B., Mandal, M. (2011). Biomaterials The potential of celecoxib-loaded hydroxyapatite-chitosan nanocomposite for the treatment of colon cancer. *Biomaterials*, 32(15), 3794–3806.
- Wang, H., Gu, W., Xiao, N., Ye, L., & Xu, Q. (2014). Chlorotoxin-conjugated graphene oxide for targeted delivery of an anticancer drug. *International Journal*

of *Nanomedicine*, 1433–1442.

- Wang, L., Shi, L., Liao, N., Jia, H., Du, P., Xi, Z., Jin, D. (2010). Photoluminescence properties of  $\text{Y}_2\text{O}_3:\text{Tb}^{3+}$  and  $\text{YBO}_3:\text{Tb}^{3+}$  green phosphors synthesized by hydrothermal method. *Materials Chemistry and Physics*, 119(3), 490–494.
- Wang, S. (2009). Ordered mesoporous materials for drug delivery. *Microporous and Mesoporous Materials*, 117, 1–9.
- Wilczewska, A. Z., Niemirowicz, K., Markiewicz, K. H., & Car, H. (2012). Nanoparticles as drug delivery systems. *Pharmacological Reports*, 64(5), 1020–1037.
- Wiwattanapongpan, J., & Mekasuwandumrong, O. (2007). Effect of dopants on the properties of metal-doped zirconia prepared by the glycothermal method. *Ceramics International*, 33(8), 1469–1473.
- Xia, L. Y., Li, X., Zhu, F., Hu, S., & Huang, L. (2017). Luminescent and Magnetic alpha-FeO@YO:Eu Bifunctional Hollow Microspheres for Drug Delivery Luminescent and Magnetic alpha-Fe<sub>2</sub>O<sub>3</sub>@Y<sub>2</sub>O<sub>3</sub>:Eu<sup>3+</sup> Bifunctional Hollow Microspheres for Drug Delivery. *Journal of Physical Chemistry C*, 121(37), 20279-20286.
- Yang, C. H., Pan, Y. X., & Zhang, Q. Y. (2007). Enhanced white light emission from Dy<sup>3+</sup>/Ce<sup>3+</sup> co-doped GdAl<sub>3</sub>(BO<sub>3</sub>)<sub>4</sub> phosphors by combustion synthesis. *Materials Science and Engineering B: Solid-State Materials for Advanced Technology*, 137(3), 195–199.
- Yang, P., Quan, Z., Hou, Z., Li, C., Kang, X., Cheng, Z., & Lin, J. (2009). Biomaterials A magnetic , luminescent and mesoporous core – shell structured composite material as drug carrier. *Biomaterials*, 30(27), 4786–4795.
- Yang, X., Zhang, X., Liu, Z., Ma, Y., Huang, Y., & Chen, Y. (2008). High-Efficiency Loading and Controlled Release of Doxorubicin Hydrochloride on Graphene Oxide. *J. Phys. Chem. C*, 112, 17554–17558.
- Zhang, X., Zhou, L., Pang, Q., & Gong, M. (2014). A broadband-excited and narrow-line GdBO<sub>3</sub>:Ce<sup>3+</sup>,Tb<sup>3+</sup>,Eu<sup>3+</sup> red phosphor with efficient Ce<sup>3+</sup> (Tb<sup>3+</sup>)<sub>n</sub> Eu<sup>3+</sup> energy transfer for NUV LEDs. *Optical Materials*, 36(7), 1112–1118.
- Zhang, Z. J., Jin, T. T., Xu, M. M., Huang, Q. Z., Li, M. R., & Zhao, J. T. (2015). Low-temperature vaterite-type LuBO<sub>3</sub>, a vacancy-stabilized phase synthesized at high temperature. *Inorganic Chemistry*, 54(3), 969–975.





